공학박사학위논문

곡선 유로에서의 비등 열전달을 이용한 전기자동차용 모터 열관리에 대한 연구

Study on the Thermal Management of Motor in Electric Vehicle using Flow Boiling Heat Transfer in Curved Channel

2019 년 8 월

서울대학교 대학원

기계항공공학부

김 선 진

곡선 유로에서의 비등 열전달을 이용한 전기자동차용 모터 열관리에 대한 연구

Study on the Thermal Management of Motor in Electric Vehicle using Flow Boiling Heat Transfer in Curved Channel

지도교수 김 민 수

이 논문을 공학박사 학위논문으로 제출함

2019 년 4 월

서울대학교 대학원

기계항공공학부

김 선 진

김선진의 공학박사 학위논문을 인준함

2019 년 6 월

위 원 장 : 민 경 덕

부위원장 : 김 민 수

위 원 : 송 한 호

위 원 : 도 형 록

위 원 : 김 민 성

Abstract

Study on the Thermal Management of Motor in Electric Vehicle using Flow Boiling Heat Transfer in Curved Channel

Sunjin Kim

Department of Mechanical and Aerospace Engineering

The Graduate School

Seoul National University

In this study, in order to improve motor cooling performance, flow boiling cooling was proposed, and experiments and simulations were conducted. Motor thermal management is important for performance improvement and failure prevention. Motor thermal management is becoming more and more important as the demand and power output of permanent magnet motor increases for eco-friendly vehicles. Due to the improved power output and reduced size, the heat loss of the motor increases and a new method is needed to replace the conventional water cooling method. For this reason, flow boiling cooling using existing cooling channel with refrigerant is proposed in this research.

In order to apply flow boiling cooling with the motor cooling, study on the flow boiling characteristics in a curved channel is required. Therefore, the experiments of heat transfer with R245fa and R134a was conducted by copying the motor cooling channel and motor heat loss. Thereby, the heat transfer coefficient according to the location in the channel was obtained. The sudden drop of the heat transfer coefficient is observed based on the location, and bubble dynamics are used to predict bubble motion to account for the heat transfer coefficient variation. Moreover, actual bubble movement is investigated using high speed camera. As a result, it was confirmed that the heat transfer coefficient decreases when the bubble adheres to the heating surface and moves in the direction opposite to the main flow. In order to prevent the reduction of the heat transfer coefficient, it is necessary to control the mass flow rate appropriately.

A lumped parameter thermal model for motor was developed to verify the performance of flow boiling cooling. Transient thermal analysis was performed by calculating the temperature and heat loss according to the position in the motor using the model. The performance of the flow boiling cooling was confirmed comparing the motor winding temperature and heat loss with the conventional water cooling method. Flow boiling cooling with the same pump power consumption condition could keep the motor winding temperature 6.3^{o}C

lower than water cooling. Furthermore, the motor power output can be improved by 6.0% without increasing pump power consumption.

In order to apply the proposed method to actual vehicle, an integrated system is proposed that uses refrigerant from existing heat pump system. The performance of the cabin thermal management and motor cooling is calculated and compared for both the PCVC (Parallel Cooling Vapor Compression) system and LPVC (Liquid Pump and Vapor Compressor) system. By pumping the refrigerant from the outlet of the condenser, the LPVC system presented high performance regardless of the season.

The method proposed in this research can be integrated to the existing vehicle system. It greatly improves the motor cooling performance compared to the conventional method. Therefore, this method will improve the performance and the safety significantly of the eco-friendly vehicle.

Keyword: Motor cooling, Flow boiling, Curved channel, Lumped parameter thermal model, Integrated heat pump system

***Identification Number*: 2014-21567**

Contents

List of Figure

List of Tables

Nomenclature

A	area (m^2)
a_w	coeffcient for electric resistance (1/K)
B	magnetic flux density (T)
Bo	boiling number
C	clearance volume ratio, constants
COP	coefficient of performance
C_d	drag coefficient
C_f	friction coefficient
C_l	shear lift coefficient
c_p	specific heat (kJ/kg-K)
D_{ch}	test section diameter (m)
D_h	hydraulic diameter (m)
Dn	Dean number
d_c	fin collar outside diameter (m)
$d_{h,ch}$	hydraulic diameter of channel (m)
dR_{tc}	distance between two holes for thermocouple (mm)
d_w	wetted diameter (m)
E	energy (kJ) or constant for boiling heat transfer
F	force (N)
F_p	fin pitch (m)
F_l	fin length (m)

f	friction factor
G	mass flux (kg/m^{2}s)
g	gravitational acceleration (= 9.81 m/s^2)
H_{ch}	height of channel (mm)
h	heat transfer coefficient (kW/m^2-K)
h_{lv}	latent heat (kJ/kg)
i	enthalpy (kJ/kg-K)
j	Couburn j factor
k	thermal conductivity (kW/m-K)
k_e	eddy current coefficient
k_h	hysteresis coefficient
L	length (m)
L_l	louver length (m)
L_p	length (m)
LPVC	liquid pump and vapor compressor
$\dot{m}$	mass flow rate (kg/s)
m_{sys}	system charge amount (kg)
N_{CB}	convective boiling coefficient
Nu	Nusselt number
n	polytropic coefficient
PCVC	parallel cooling vapor compression
Pr	Prandtl number
Q	heat generation (kJ)
$\dot{q}, \dot{Q}$	heat (kW)

q''	heat flux (kW/m^2)
R	thermal resistance (K/W)
$R_{c,i}$	inner radius of curved channel (mm)
$R_{c,o}$	outer radius of curved channel (mm)
$R_{tc,1}$	distance from center of test section to 1st thermocouple hole (mm)
R_w	eletric resistance of winding (Ω)
Re	Reynolds number
r	r-direction
r1	inner radius of dicretized cell
r2	outer radius of dicretized cell
T	temperature (^{o}C)
Ta	Taylor number
T_d	tube depth (mm)
T_p	tube pitch (mm)
UA	overall heat transfer coefficient (kW/K)
u	velocity
u_∞	liquid mean velocity in channel (m/s)
V	volume (m^3)
v	velocity (m/s)
$\dot{W}$	work (kW)
W_{ch}	width of channle (mm)
W_s	width of side wall (mm)
W_t	total width heated (mm)

X_{tt}	lockhart–martinelli parameter
x	vapor quality
z_0	depth of dicretized cell

Greek

α	upstream contact angle
β	downstream contact angle or constant for iron loss
δ_f	fin thickness (mm)
ε	void fraction
θ	angle
θ_l	louver angle [deg]
θ_0	angle of dicretized cell
μ	dynamic viscosity (m^2/s)
ρ	density (kg/m^3)
σ	surface tension (m/s^2)
η_f	fin efficiency
τ	shear stress (Pa)
ω	rotational speed (rad/s)

Subscript

air	air side
b	bubble or buoyancy

c	cell, cooling
ch	channel
comp	compressor
cond	condenser
d	drag
disp	displacement
EEV	electronic expansion valve
e	element
evap	evaporator
exp	experiment
f	fluid
fric	frictional
frt	frontal
gap	air gap
h	heating
ht	heated
k	k^{th} location
l	liquid, lower
lo	liquid only
m	mean
max	maximum
mom	momentum
mot	motor
n	normal

r	r-direction
ref	refrigerant
rms	root mean square
rot	rotor
sim	simulation
sl	shear lift
sn	surface tension in normal direction
st	surface tension in tangential direction
sta	stator
str	stored
sys	system
t	tangential
tc	thermocouple
tp	two-phase
u	upper
v	vapor
w	wall or winding
wt	water
z	z-direction
θ	theta direction

Chapter 1. Introduction

1.1 Background of the study

Emission regulation on the conventional vehicles and growth of technology for renewable energy are changing the trend of global vehicle market [1]. Research and development of eco-friendly vehicles such as electric cars, hybrid cars and fuel cell cars are being carried out more actively than ever as an alternative of existing internal combustion engine vehicles. According to Fig. 1.1, the share of electric vehicles in the global vehicle market in 2025 is expected to be about 8% and this percentage is four times higher market share than that of the present state. Furthermore, by 2040, 54% of all vehicles are expected to be replaced as an electric cars [2]. In fact, legislation has been passed that bans the sale of internal combustion engine vehicles by 2025 or later in many countries in the world. With this trend, the importance of eco-friendly vehicles is expected to grow.

Eco-friendly vehicles share in common that they use electricity as an energy source to create driving force. Thus, an electric motor is required to convert electrical energy into driving force. The electric motor uses the input electricity to induce a magnetic field to interact with the induced magnetic field

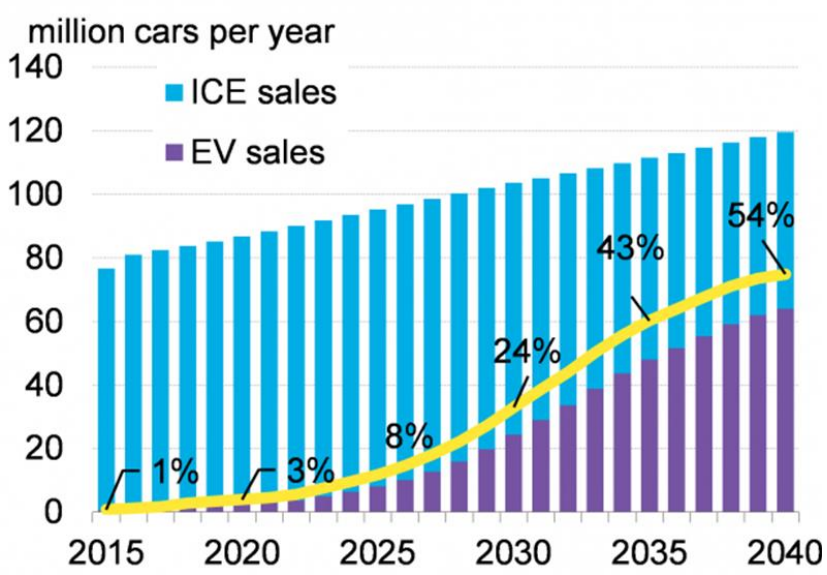

Fig. 1.1 Annual global light-duty vehicle sales [2]

or the magnetic field of the attached magnet in the motor, thereby converting the electromagnetic force into a rotational force. Because high torque and high power output are required to be applied to vehicles, most of the eco-friendly vehicles use permanent magnet synchronous motors (PMSM) [3]. The driving force of the electric motor is generated by the electromagnetic field of the winding and the permanent magnet. To be applied to vehicles, the power output of the motor is continually increased. As a result, the amount of heat loss due to the generation of electromagnetic force increases. It is the cause of continuous temperature rising of the winding and permanent magnet in the motor during motor operation. However, as shown in Fig. 1.2, the life time of the electric motor is directly affected by the motor temperature [4]. When the temperature of the motor winding rises, the insulation of the winding is damaged, which causes performance degradation or even a fatal failure of the motor. The permanent magnet has a similar thermal management issue as permanent demagnetization phenomenon. When the temperature of the magnet exceeds the critical temperature, the performance is greatly reduced [5]. Besides, the heat loss due to the current through the winding varies greatly with the winding temperature shown in Fig. 1.3, because the electric resistance of the copper varies with its temperature. Therefore, proper thermal management is crucial for safe operation and efficiency improvement of the PMSM.

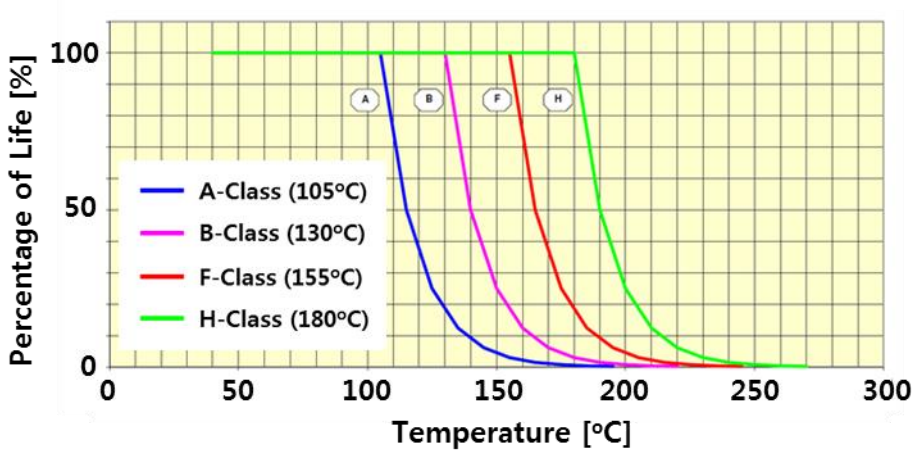

Fig. 1.2 The relationship between winding temperature and motor life time with respect to winding insulation class [4]

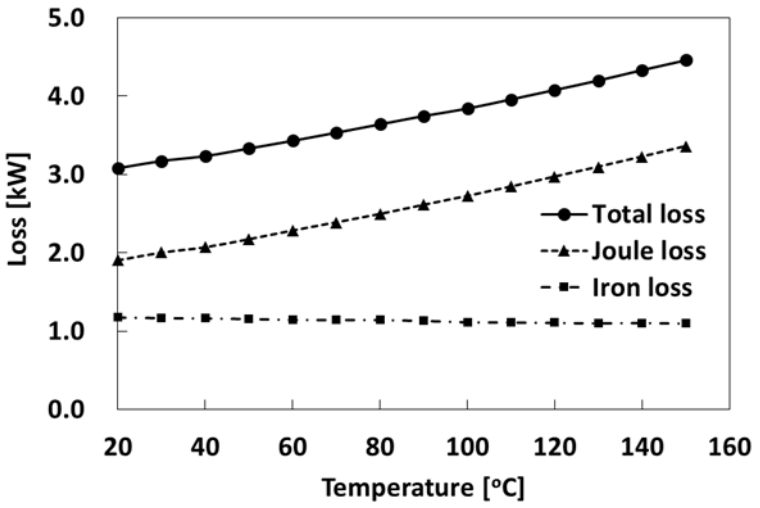

Fig. 1.3 Energy loss of a motor with respect to its temperature

(Driving condition: 240 Nm, 6000 rpm)

Thermal management has not been considered especially for small motors. Due to the small heat loss, natural convection was enough for motor cooling. However, the power output of the motor is increased, an air cooling using forced convection was gradually applied. Furthermore, in the case of a high performance electric motor for eco-friendly vehicles, a channel or a jacket is designed around the motor to cool them through coolant flow as shown in Fig. 1.4 [6]. Nevertheless, as the required performance of eco-friendly vehicles continues to increase, performance of water cooling has been reached its limitation. Therefore, new methods for thermal management of high performance electric motor should be suggested.

One of the most important issues for eco-friendly vehicles is about mileage. Because eco-friendly cars use electric energy for driving, electric energy used for HVAC (heating, ventilation and air-conditioning) has a serious influence on the reduction of mileage. Air-conditioner during summer season and cabin heating system such as PTC heater or heat pump during winter season are the main factors of energy consumption [7]. The energy used by the motor thermal management system also affects the reduction of driving mileage. Therefore, the method of motor thermal management needs to be designed considering not only the thermal management of the motor itself but also the performance and feasibility with the entire vehicle.

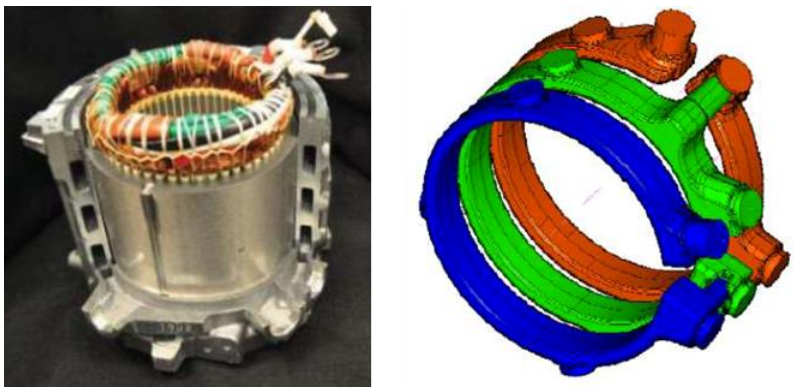

Fig. 1.4 Water cooling jacket of Nissan Leaf motor [6]

1.2 Literature survey

1.2.1 Boiling heat transfer in curved channel

In order to cool the motor properly, it is necessary to find a cooling method that can increase the heat transfer coefficient for a given channel geometry. In this case, flow boiling is a solution. Flow boiling is known to have a high heat transfer coefficient as compared to single phase flow. The characteristics of single phase heat transfer and two-phase flow heat transfer coefficients in a straight tube are already widely known [8 - 10]. However, considering the shape of the electric motor, the straight tube is difficult to be applied for the cooling jacket. In order to maximize the heat transfer area, a flow path which has maximum contact area with the side of the motor as cylindrical shape is necessary. In this case, the channel is continuously connected curved rectangular channel as shown in Fig. 1.4 [6].

A study of two phase flow pattern in a curve channel is found in the researches of the U-bend shape channel. Wang et al. [11] studied an influence of vapor quality, mass flux and tube diameter using air and water mixture in a horizontal return bend. The authors proposed flow pattern map based on the visualization results and verified that flow pattern is affected by surface tension

and reduction of developing length. Chu et al. [12] conducted experimental and numerical study on the pressure drop in curved rectangular microchannels. Padilla el al. [13] investigated pressure drop and two-phase flow pattern with visualization experiments. In this paper, pressure drop is analyzed by flow regimes such as slug and annular flow. However, these studies didn't take account of flow boiling in the channel. Since all of these researches are conducted for U-bend in a heat exchanger, they has a limitation for explaining the flow boiling for a cooling channel which encloses a cylindrical motor.

There is another references of the helical coiled channel having a similar geometry to the cooling channel of a motor. It has been widely used in steam generator for a nuclear reactors and heat exchangers for many applications to increase heat exchange area. Since water and steam are used in nuclear reactors, enormous studies have been conducted [14-19]. Furthermore, researches on R134a used in heat pump for vehicles have been actively investigated. Chen et al. [20] studied wall temperature distribution and average heat transfer coefficient of flow boiling in helically coiled tubes by their experimental setup. Heat transfer characteristics at low mass flux and low pressure is analyzed. Elsayed et al. [21] investigated flow boiling heat transfer inside small diameter helically coiled tubes. Based on the results of heat transfer coefficient from this paper, they propose new correlation. Cui et al. [22] and Aria et al. [23]

conducted experimental researches on heat transfer characteristics about vertical helically coiled tubes. Wongwises et al. [24] studied evaporation heat transfer and pressure drop of R134a in a helically coiled heat exchanger. The authors suggest new correlations for heat transfer coefficient and pressure drop to account for obtained results. Moreover, condensation heat transfer of R134a is investigated by existing papers [25-27]. Nevertheless, the study of flow boiling in a curved rectangular channel is still insufficient if considering motor cooling jacket. It is necessary to study flow boiling heat transfer in which heat flux and mass flow rate are properly selected in consideration of the heat loss amount of motor for electric vehicles.

1.2.2 Thermal management for electric motor

Electric motors always need suitable thermal management because of the risk of performance degradation and failure due to temperature rise. When the ratio of power output divided by volume is small, sufficient cooling is possible by air using a fan. For air cooling motor, many researches focus on the cooling performance with the control of the fan or the geometry of the air flow path [28-32]. However, the power density of the motor has increased, an improved cooling method has been required. Water cooling has been adopted as a solution.

Chiu et al. [33] presented advanced cooling performance of water jacket compared with air cooling method. Pechánek et al. [34] investigated effect of cooling jacket geometry on the cooling performance. Tüysüz et al. [35] proposed additional axial duct inside of the winding for the coolant. As a result, maximum winding temperature decreased and motor efficiency is improved. Furthermore, Chen et al. [36] researched the design and optimization of dual-cycled cooling structure in which water jacket cooling and forced air cooling were combined.

Nonetheless, the power density of electric motors is increasing and more effective cooling methods are being investigated. Various studies have been conducted, such as heat pipe attached on the motor case [37], improvement of thermal conductivity by silicon on the end winding [38] and phase change material inside of a motor [39-41]. The most actively researched method among them is oil cooling. Oil cooling method has better cooling performance than water cooling. Lim et al. [42] studied in-wheel motor thermal management using oil spray cooling system. The authors developed thermal model of an oil cooled motor and conducted experimental research to optimize and validate the cooling performance of oil spray system. Davin et al. [43] investigated diverse oil cooling method such as dripping injection or jet nozzle injection. In this paper, effect of oil flow rate and rotational speed of the rotor on the cooling

performance is evaluated by experimental research. Lee et al. [44] researched rotor cooling method using a hollow shaft design by the authors. Proposed oil cooling system showed higher cooling performance compared with general oil cooling [45] and oil spray cooling [46].

Even though various studies have demonstrated the performance of oil cooling, applying oil cooling method to actual vehicles has a problem. Oil cooling systems require an additional system to cool the oil used to cool the motor. The cost of the vehicle can be significantly increased due to the complexity of the vehicle system. Therefore, new methods are needed that can be properly integrated to a vehicle system while providing cooling performance similar to oil cooling performance. Flow boiling is a solution to satisfy these requirements. In order to improve the cooling performance, studies on the flow boiling applied in inverter cooling [47-48] or fuel cell thermal management [49-50] are actively conducted. Not only it is possible to improve the cooling performance using flow boiling of two phase refrigerant, but also the refrigerant of a conventional heat pump system in a vehicle can be adopted. Therefore, sophisticated research on the flow boiling for motor cooling is necessary.

1.2.3 Thermal management system for electric vehicle

Electric vehicles should minimize electricity consumption except for driving. For this reason, many studies have been conducted to optimize HVAC and component thermal management systems and to minimize its power consumption. Leigton [51] designed a water-based electric vehicle integrated cooling system and demonstrated its performance through bench test. This system achieved mileage improvement by reducing electric energy consumption for cabin heating at the winter season. In order to maximize the mileage of electric vehicles, especially, reduction of energy used for cabin heating in the winter has been actively researched. Kwon et al. [52] investigated heating performance of vapor injection heat pump system for electric vehicle at low ambient temperature. Compared with convectional heat pump, both coefficient of performance (COP) and heating capacity are improved. Choi et al. [53] studied the performance optimization of the vapor injection heat pump system depending on the location of injection position on the scroll compressor and intermediate pressure ratio. Ahn et al. [54] researched about dual source heat pump system using both air and waste heat in electric vehicle as heat sources. The authors presented the performance of various heating modes by their experimental setup. They also studied effective dehumidifying by electric vehicle heat pump system using an additional waste heat with low occupancy

[55]. As a result, heating capacity and COP improved by 15.8% and 5.2% respectively. In addition to these researches, various studies have been conducted to improve the performance of the whole electric vehicle thermal management system [56-59]. Therefore, the flow boiling method for motor cooling needs to be integrated into the conventional vehicle system so that the energy consumption of the system can be reduced.

A solution that can provide phase change cooling by flow boiling while minimizing power consumption is using a liquid pump. In fact, various studies have been conducted to carry out phase change cooling using a liquid pump or only gravity. Lee et al. [60] investigated hybrid cooler combining vapor compression and natural circulation cycles by gravity using R134a as a refrigerant. In this research, performance optimization of the hybrid cooler is conducted on the refrigerant charge, heat exchanger geometry and the vertical distance between the condenser and the evaporator. Zhang et al. [61] studied integrated air conditioner with thermosyphon for heat recovery from internet data centers. As a result, 60% of the energy consumption is saved compared with the traditional coal-fired boiler for heating of buildings. Dong et al. [62] researched integrated system driven by both liquid pump and vapor compressor using R22 as a refrigerant to reduce the energy consumption of the cooling system for data centers. In this paper, influence of pump rotational speed and

outdoor temperature on the performance of the system is evaluated by experimental results. Zhang et al. [63] investigated CO_2 loop thermosiphon in an integrated air conditioning system. Numerical study was conducted on the performance of the designed system as filling ratio of the refrigerant in the system, riser length and height difference of the evaporator side are the main parameters. The above studies considered the vapor compression cycle at high ambient temperature or liquid refrigerant cooling system at low ambient temperature selectively to cool the target. However, in the case of motor cooling of an electric vehicle, heat pump system must be operated basically and at the same time flow boiling for motor cooling should be driven. Therefore, research on a system that simultaneously drives both the flow boiling method and heat pump system is required.

1.3 Objectives and scopes

Due to the necessary of the new motor cooling method with improved cooling performance and applicability to the vehicle system, this paper investigates flow boiling cooling for the motor using an outer jacket. Flow boiling cooling can exhibit improved cooling performance as compared to conventional water cooling method. Moreover, unlike other methods which are

being researched recently, using refrigerant from the existing heat pump system in the vehicle can minimize the complexity of the system. The integrated system allows the use of waste heat from the motor in winter season for indoor heating to minimize vehicle energy consumption. Therefore, in this paper, researches are conducted to apply flow boiling cooling to the motor in an electric vehicle.

In the chapter 2, before dealing with the cooling system of the motor, the flow boiling heat transfer in the curved rectangular channel similar with the motor cooling jacket is investigated. The heat transfer characteristics of R245fa and R134a in the curved rectangular channel are studied through experimental analysis. Moreover, the movement of a bubble during flow boiling in the curved rectangular channel is observed and analyzed through visualization experiments to predict and confirm the change of the local heat transfer coefficient.

In the chapter 3, comparison of cooling performance between flow boiling cooling method and conventional water cooling for a motor is conducted by transient analysis. For the performance comparison, fully lumped parameter thermal model which can calculate temperature variation with time and temperature distribution inside the motor is developed. In addition, based on the electromagnetic analysis, the change of the heat loss of the motor according to the motor temperature is evaluated.

In the chapter 4, integrated system which combines the existing heat pump system for cabin thermal management and flow boiling cooling system for a motor is proposed and analyzed by steady state simulation. The performance of the system using a liquid pump and the system using parallel low pressure line for the motor cooling is compared according to the seasonal operating condition. The performance of the systems are evaluated based on the motor cooling performance and vehicle energy consumption.

Chapter 2. Experimental study on the flow boiling of R245fa and R134a in curved rectangular channel

2.1 Introduction

In this chapter, heat transfer characteristics in the curved rectangular channel are described through experiments. Heat transfer in straight channels and U-bends has been studied by many researchers. However, studies of flow boiling heat transfer in a curved rectangular channel that wraps around a cylindrical object such as a motor are still insufficient. Therefore, in this research, the boiling heat transfer coefficient is measured by the simulated cooling channel of the motor with simulating the heat generation of the motor. Furthermore, the flow boiling and movement of bubbles in the curved rectangular channel is observed through the visualization experiment.

The content of the first section is experimental researches for the heat transfer coefficient using R245fa and R134a. The temperature and the pressure of the channel are measured according to the mass flow rate, degree of subcool (DSC) of the channel inlet and channel heating value. As a result, the local heat

transfer coefficient in the curved rectangular channel is calculated. During flow boiling occurs in the channel, the temperature of the channel wall and local heat transfer coefficient are varied dramatically depending on the position of the channel.

The variation of the local heat transfer coefficient with location in the channel is analyzed in the second section. When flow boiling occurs in the curved rectangular channel, the generated bubbles are affected by various forces based on the position where they are initially generated. Due to the forces on the bubbles, moving direction and speed of the bubbles are changed. It can improve or impede the heat transfer performance on the specific position in the channel. Therefore, the change of the heat transfer coefficient according to the position is explained by comparing the movement of the bubble predicted through bubble dynamics and the result obtained through the visualization experiments.

2.2 Experimental setup

2.2.1 Experimental apparatus

A schematic diagram of experiment for flow boiling in curved rectangular

channel is presented in Fig. 2.1. Solid line presents refrigerant line and dashed line means water line. Liquid refrigerant from the reservoir passes magnetic gear pump. It is heated by preheater if inlet temperature needs to be changed. Afterward, refrigerant goes through the test section which is curved rectangular channel and flow boiling occurs inside the channel. Finally, it passes plated heat exchanger which cools the refrigerant using cold water from the chiller. Temperature, pressure, mass flow rate and heating power are measured by installed sensors. Measured data is gathered by a data acquisition module. The detailed information about installed sensors and the data acquisition module is presented in Table 2.1. Pictures of the experimental setup are shown in the Fig. 2.2. Fig. 2.2(a) is the picture of total system when heat transfer coefficient is calculated by measured data. Fig. 2.2(b) shows visualization experiment with high speed camera for observing movement of the bubbles.

2.2.2 Design of test section

Test section is designed as shown in Fig. 2.3. 24 cartridge heaters and 24 thermocouples are inserted perpendicular to the channel. Channel geometry is chosen based on the existing motor cooling jacket. Fig. 2.3(b) shows cross section of A-A presented in Fig. 2.3(a). W_{ch} and H_{ch} are the width and height of

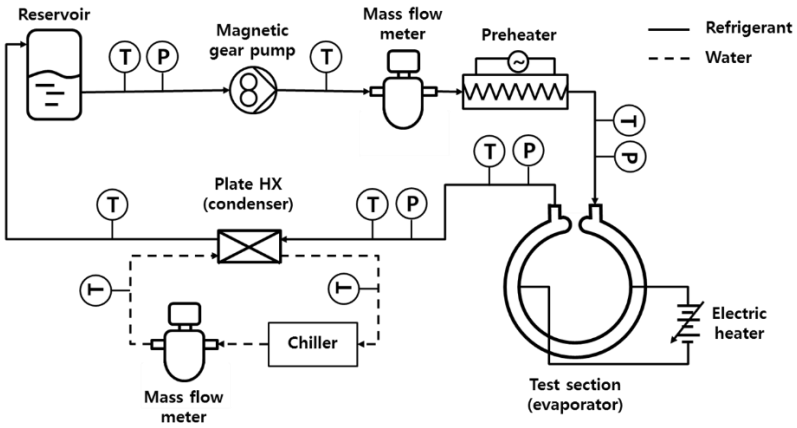

Fig. 2.1 Schematic of experimental setup

Table 2.1 Information of sensors and devices

Sensors	**Model**	**Manufacturer**	**Measurement accuracy**
Thermocouple	T-type	OMEGA	±0.5°C
Mass flow meter	ULTRAmass MKII	Oval	±0.2% of reading
Pressure transmitter	UNIK 5000	GE	±0.4% of full scale
Power meter	WT130	Yokogawa	±0.3% of reading

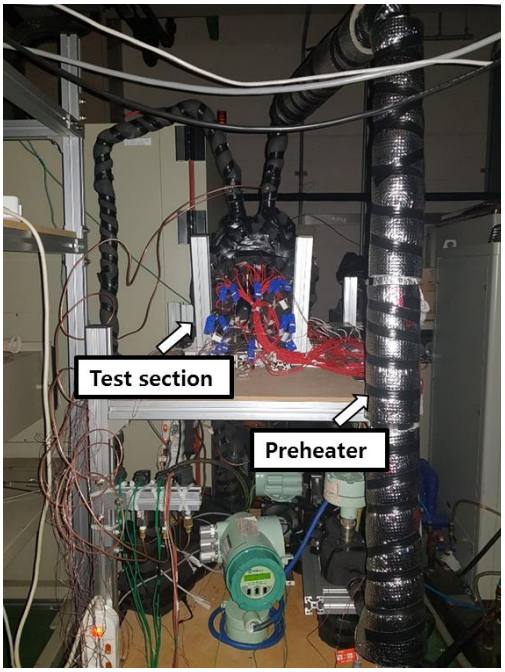

(a)

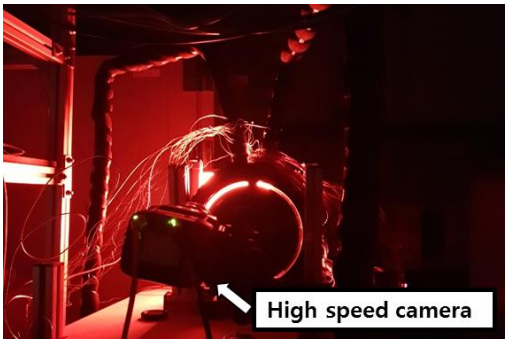

(b)

Fig. 2.2 Pictures of experimental setup (a) total system and (b) test section with high speed camera

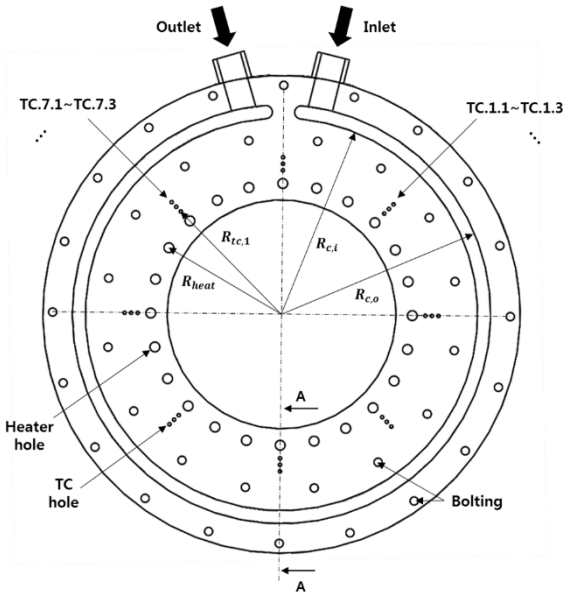

(a)

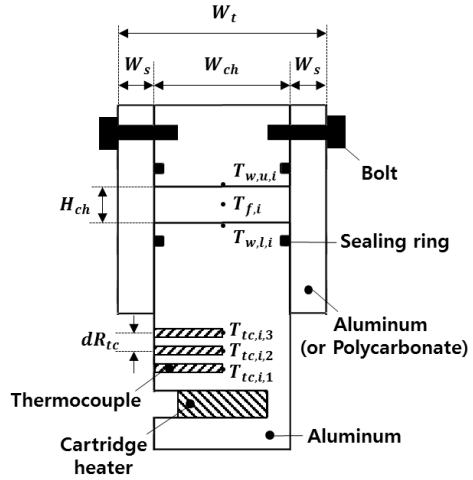

(b)

Fig. 2.3 Design of test section (a) curved channel, (b) cross section A-A of the channel presented in Fig. 2.3(a)

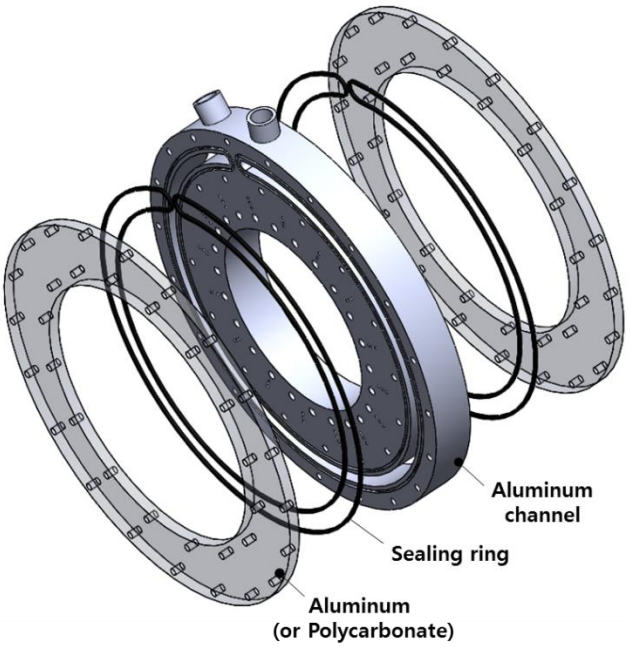

Fig. 2.3 Design of test section (c) assembly of the test section

the channel. Three parallel thermocouples measure the temperature gradient of the channel to calculate the heat flux from the heater to the refrigerant. Side wall of the channel is used as aluminum plate for heat transfer experiment and polycarbonate plate for visualization experiment. The temperature of the channel is measured at the 7 location for obtaining local heat transfer coefficient. Measurement points are 45^{o} apart from each other. Location 1 is the closest point to the inlet and location 7 is the closest point to the outlet. The detailed values of the test section geometry are described in Table 2.2. Assembly of the test section is described in Fig. 2.3(c).

2.2.3 Test condition

The experimental conditions for the measurement of the heat transfer coefficient are chosen taking into account the actual motor cooling channel and the heat generation from the motor. If considering the efficiency of a motor of 100 kW power output or more, the heat generation is usually less than 4 kW. Since the existing cooling channel of the motor is composed of four parallel channels, the heat generated by the motor per channel is 1 kW level. Thus the heat transferred to the channel is designed as 1.02 kW. In the case of the saturation temperature of the refrigerants, the temperature was determined

based on the refrigerant temperature in the condenser which can be the highest temperature in the heat pump system of a vehicle.

The refrigerants are selected as R245fa and R134a. R134a is a refrigerant that is popularly used in heat pump system for vehicles. Therefore, when flow boiling cooling is applied to the actual motor, it is the most likely candidate. However, the heat pump utilizing R134a has a high pressure as high as 1300 kPa level during operation. Thus, visualization experiments for observation of bubble movement were performed using R245fa. R245fa has a pressure of up to 400 kPa at the temperature of the experimental conditions. It is suitable for experiments using a visualization plate. The detailed conditions are described in Table 2.3.

2.3 Data reduction and validation

2.3.1 Calculating local pressure

In the experiment, the inlet and outlet pressure are measured. In order to obtain the local heat transfer coefficient, it is necessary to calculate the local pressure and temperature in the channel. The local pressure is calculated based on the local pressure drop. Fig. 2.4(a) shows simple diagram of the channel and

Table 2.2 Geometric parameters of the test section

Parameter	Value [mm]
$R_{c,i}$	120
$R_{c,o}$	128
$R_{tc,1}$	88
dR_{tc}	4
R_{heat}	80
W_{ch}	30
W_s	8
W_t	46
H_{ch}	8

Table 2.3 Experimental condition

Experimental Conditions	**R245fa**	**R134a**
Channel heating power [W]	0 ~ 1020	
Preheating power [W]	0 ~ 700	
Mass flux [kg/m^2 s]	43.8 ~ 233.3	20.8 ~ 158.8
DSC of channel inlet [^{o}C]	0.6 ~ 23.5	0.6 ~ 32.2
Saturated temperature [^{o}C]	21.4 ~ 55.1	24.0 ~ 65.9
Water temperature [^{o}C]	9.3 ~ 27.5	17.8 ~ 37.2

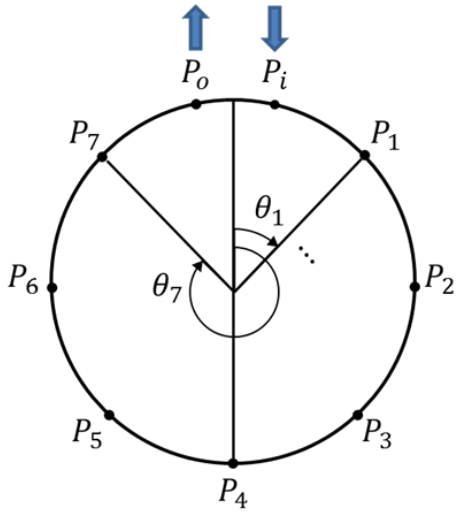

(a)

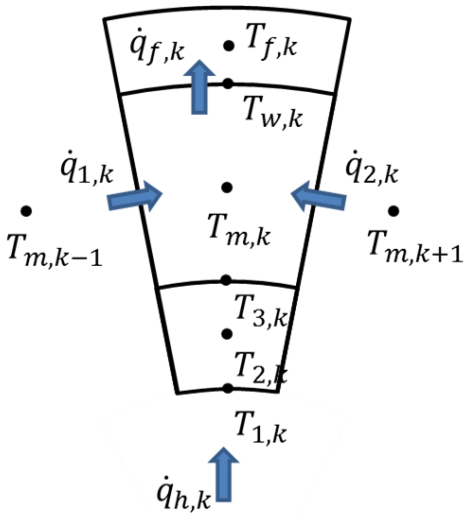

(b)

Fig. 2.4 Simple diagram for data reduction (a) pressure distribution in the channel and (b) temperature and heat transfer in the channel and fluid

local pressure. P_i and P_o are measured separately. From these values, total pressure drop in the channel is calculated from Eq. (2.1).

$$\Delta P_{ch} = P_i - P_o \tag{2.1}$$

Total pressure drop in the channel is the sum of three terms as presented in Eq. (2.2).

$$\Delta P_{ch} = \Delta P_{static,ch} + \Delta P_{fric,ch} + \Delta P_{mom,ch} \tag{2.2}$$

$\Delta P_{static,ch}$ is static pressure drop in the channel, $\Delta P_{fric,ch}$ is frictional pressure in the channel and $\Delta P_{mom,ch}$ is momentum pressure drop in the channel. Because the inlet and outlet pressure of the channel are measured at the same height from the bottom, $\Delta P_{static,ch}$ is equal to zero. In order to calculate local pressure, local pressure drop and pressure of each location are obtained from Eq. (2.3) ~ (2.4).

$$\Delta P_k = P_{k-1} - P_k \quad (k = 1, 2, \dots, 7) \tag{2.3}$$

$$\Delta P_k = \Delta P_{static,k} + \Delta P_{fric,k} + \Delta P_{mom,k} \tag{2.4}$$

As shown in Eq. (2.5) ~ (2.7), $\Delta P_{static,k}$ is calculated from the height difference of each location.

$$\Delta P_{static,k} = \tilde{\rho} g R_{c,i}\{(1-\sin\theta_{k-1}) - (1-\sin\theta_k)\} \tag{2.5}$$

$$\tilde{\rho} = \rho_l(1-\epsilon) + \rho_v \epsilon \tag{2.6}$$

$$\epsilon = \frac{x}{\rho_v}\left[\left(1+0.12(1-x)\right)\left(\frac{x}{\rho_v}+\frac{1-x}{\rho_l}\right) + \frac{1.18(1-x)[g\sigma(\rho_l-\rho_v)]^{0.25}}{G\rho_l^{0.5}}\right]^{-1} \tag{2.7}$$

$\tilde{\rho}$ is average density of the local point in the channel. ϵ is the void fraction calculated by basic correlation from Rouhani and Axelsson [64]. The parameter required for the correlation is adopted from Padilla et al. [65].

Local frictional pressure drop and local momentum pressure drop are assumed linearly as shown in Eq. (2.8).

$$\Delta P_{fric,k} + \Delta P_{mom,k} = \frac{1}{8}\Delta P_{ch} \tag{2.8}$$

From Eq. (2.4) ~ (2.8), local pressure drop is derived as Eq. (2.9).

$$\Delta P_k = \tilde{\rho} g R_{c,i}\{(1-\sin\theta_{k-1}) - (1-\sin\theta_k)\} + \frac{1}{8}\Delta P_{ch} \quad (2.9)$$

2.3.2 Calculating local heat transfer coefficient

Local heat transfer coefficient is obtained from energy balance between channel and refrigerant as presented in Fig. 2.4(b). $T_{tc,i,1}$ ~ $T_{tc,i,3}$ are measured. Considering discretized cell as sector of channel, temperature distribution is calculated by heat dissipation equation in the radial direction of the cylindrical coordinate as shown in Eq. (2.10).

$$\frac{d}{dr}\left(kr\frac{dT}{dr}\right) + \dot{q} = 0 \quad (2.10)$$

Heat is coming from inside of the cell, $\dot{q}$ is equal to zero. As a result, temperature distribution is calculated as Eq. (2.11).

$$T(r) = C_1 \ln(r) + C_2 \quad (2.11)$$

C_1 and C_2 are obtained from measured temperature of $T_{tc,i,1}$ ~ $T_{tc,i,3}$. $T_{w,l,i}$ and $T_{m,i}$ are calculated using Eq. (2.10). In the same manner, $T_{m,i-1}$ and $T_{w,m,i+1}$ are obtained.

Heat transfer and energy conservation is considered for the cell as Eq. (2.12)

~ (2.15).

$$\dot{q}_{f,i} = \dot{q}_{1,i} + \dot{q}_{2,i} + \dot{q}_{ht,i} \tag{2.12}$$

$$\dot{q}_{1,i} = (UA)_{1,i}\left(T_{m,i-1} - T_{m,i}\right) \tag{2.13}$$

$$\dot{q}_{2,i} = (UA)_{2,i}\left(T_{m,i+1} - T_{m,i}\right) \tag{2.14}$$

$$\dot{q}_{ht,i} = (UA)_{ht,i}\left(T_{tc,i,3} - T_{m,i}\right) \tag{2.15}$$

$\dot{q}_{f,i}$ is heat transfer from channel wall to fluid. $\dot{q}_{1,i}$ is heat transfer from the left cell of the channel to i^{th} cell. $\dot{q}_{2,i}$ is heat transfer from the right cell of the channel to i^{th} cell. $\dot{q}_{ht,i}$ is heat transfer from the inside cell of the channel to i^{th} cell. The UA value of each cell is calculated as Eq. (2.16) ~ (2.18).

$$(UA)_{1,i} = \frac{\theta_0(r_1 + r_2)}{4kz_0(r_2 - r_1)} \tag{2.16}$$

$$(UA)_{2,i} = \frac{\theta_0(r_1 + r_2)}{4kz_0(r_2 - r_1)} \tag{2.17}$$

$$(UA)_{ht,i} = \frac{1}{2\theta_0 kz_0}\left(\frac{2r_2^2 \ln(r_2/r_1)}{r_2^2 - r_1^2} - 1\right) \tag{2.18}$$

Refrigerant temperature at the location *i* is calculated from its enthalpy and the enthalpy is obtained from Eq. (2.19).

$$h_i = h_{i-1} + \frac{\dot{q}_{f,i}}{\dot{m}_f} \tag{2.19}$$

h_i is the enthalpy of i^{th} cell. $\dot{m}_f$ is the mass flow rate of the fluid.

Furthermore, from the fluid's point of view, the heat from the four sides of the channel is transferred, it is necessary to take into account the effect of non-heated upper and side wall. For this reason, the side wall is considered as a fin. The side wall have a lower temperature as they move away from the heated lower surface. Therefore, considering the temperature distribution in the fin, the temperature of the upper wall can be determined as shown in Eq. (2.20) ~ (2.21).

$$T_{w,u,i} - T_{f,i} = \frac{1}{\cosh(mL)}\left(T_{w,l,i} - T_{f,i}\right) \tag{2.20}$$

$$m = \sqrt{\frac{h_{tp,i}}{kH_{ch}}} \tag{2.21}$$

As a result, local heat transfer coefficient for refrigerant is calculated from Eq. (2.22) with iterative procedure.

$$\dot{q}_{f,i} = h_{tp,i}\left(T_{w,l,i} - T_{f,i}\right)\frac{W_{ch}}{W_t}\left(\frac{2\eta_f H_{ch}}{W_{ch}} + 1 + \frac{1}{\cosh(mL)}\right) \tag{2.22}$$

Where,

$$\eta_f = \frac{\tanh(mL)}{mL} \tag{2.23}$$

The enthalpy and other physical properties needed for data reduction and further analysis in this paper are obtained using the measured temperature and pressure based on the REFPROP 10.0 [66].

2.3.3 Experimental setup validation

Prior to conducting the flow boiling experiment, the validation of the experimental setup was confirmed. Fig. 2.5 shows the results of the energy balance based on the measured results of the experiments for the single-phase flow. Fig. 2.5(a) compares the channel heat measured by the power meter and the heat calculated by measured temperature and pressure at the channel inlet and outlet. Fig. 2.5(b) shows both the heat from the refrigerant obtained by its temperature and pressure and the heat to the water calculated by its temperature in the plate heat exchanger as a condenser. Measurement and energy balance are confirmed by these results.

Calculated local heat transfer coefficients are verified by existing

correlation. Kandlikar [10] proposed a correlation for two-phase heat transfer coefficient in a straight tube. Considering the effect of bubble movement in the curved channel, location 7 is rarely affected by bubble movement. Therefore, obtained local heat transfer coefficients at the location 7 are compared with predicted heat transfer coefficient using Kandlikar's correlation as presented in Fig. 2.6. The results identify the reliability of calculated local heat transfer coefficient from the experimental setup in this research.

2.4 Results and discussion

2.4.1 Flow boiling heat transfer coefficient of R245fa and R134a

The local heat transfer coefficient in the curved rectangular channel is greatly influenced depending on the position. It can be seen that the result of the local heat transfer coefficient varies significantly based on the position in the channel as shown in Fig. 2.7(a). Fig. 2.7 shows the results of the local heat transfer coefficient, vapor quality, and the wall temperature according to the inlet temperature and location on the channel when the mass flux is 87.5 kg/m^2s and the saturated temperature is 40.9^oC for R245fa. As shown in Fig. 2.7(a) and (b), when the vapor quality is near zero, the local heat transfer coefficient is

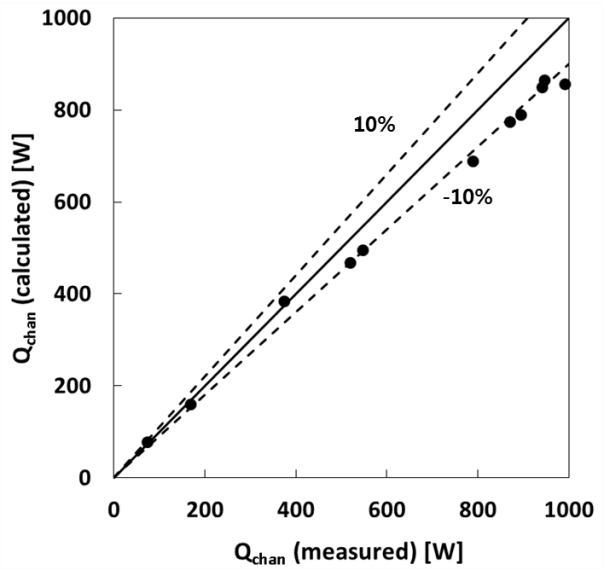

(a)

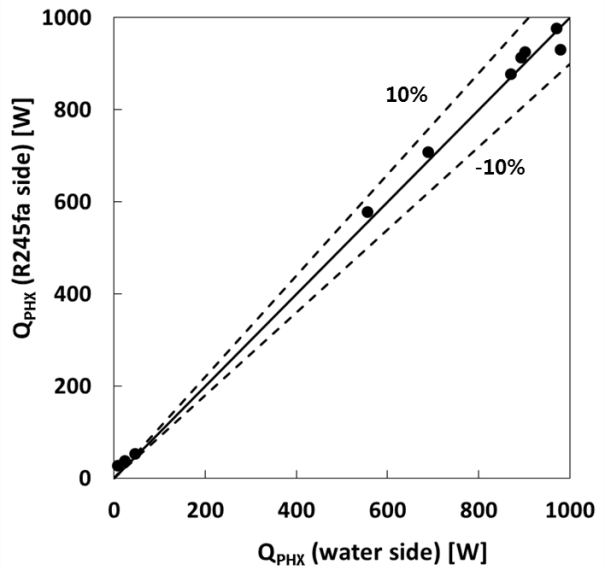

(b)

Fig. 2.5 Experimental setup validation (a) measured heat and calculated heat on the channel and (b) energy balance in the condenser

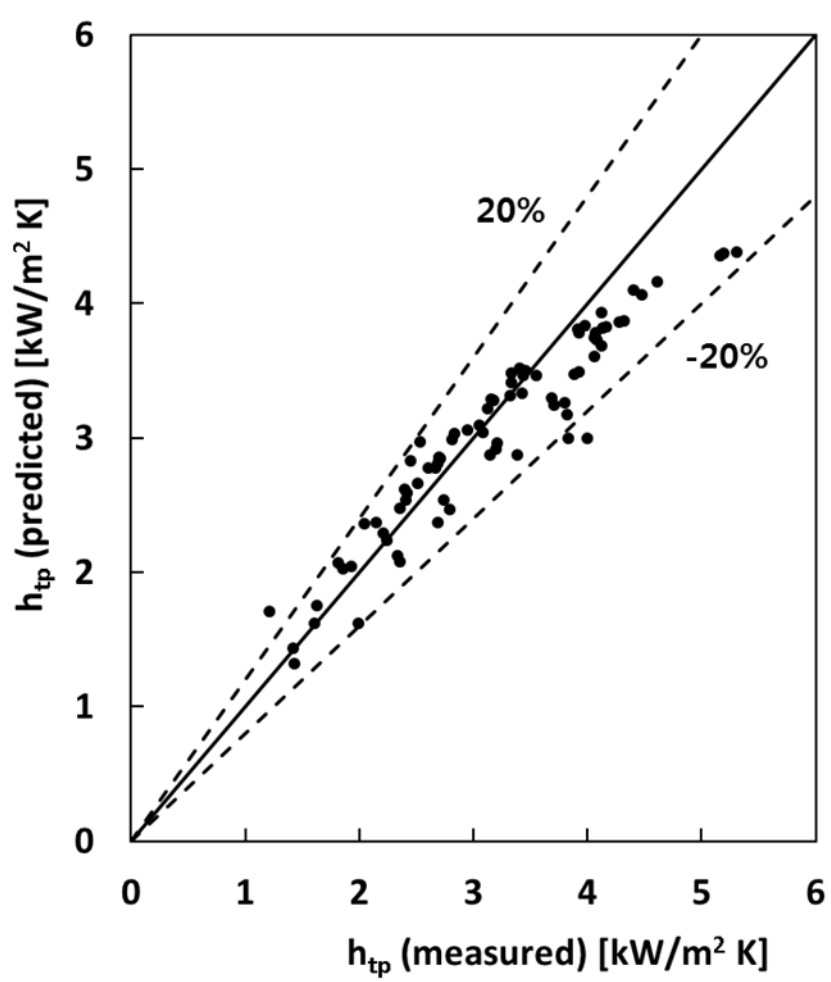

Fig. 2.6 Comparison between calculated heat transfer coefficient from measured data at location 7 (R245fa) and predicted heat transfer coefficient from Kandlikar [10]

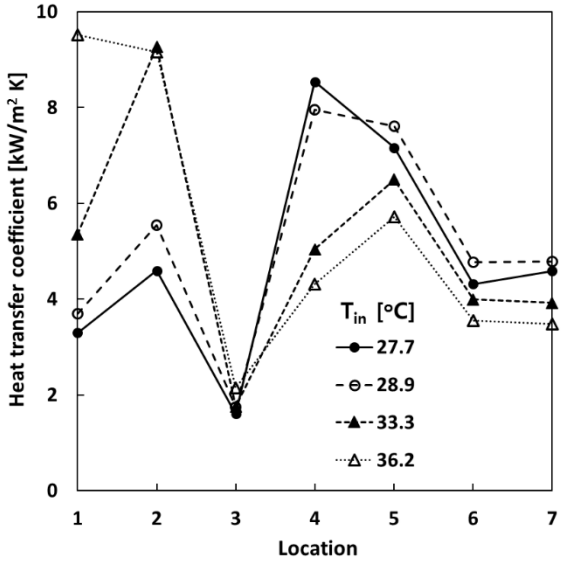

(a)

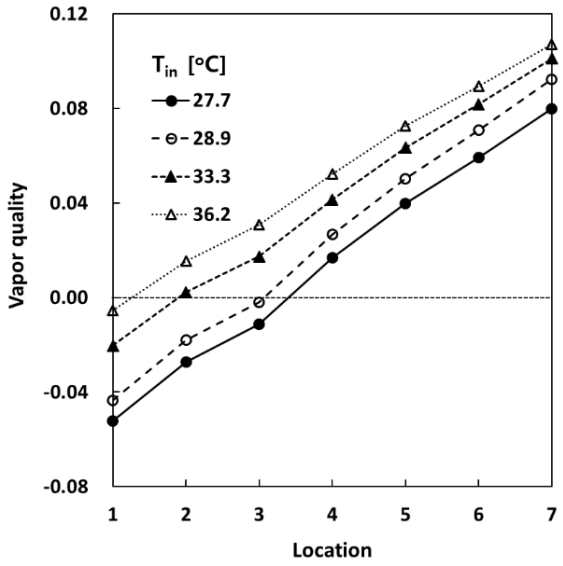

(b)

Fig. 2.7 Variation of (a) heat transfer coefficient and (b) vapor quality with respect to inlet temperature and location

(R245fa, G = 87.5 kg/m^2 s, T_{sat} = 40.9^{o}C)

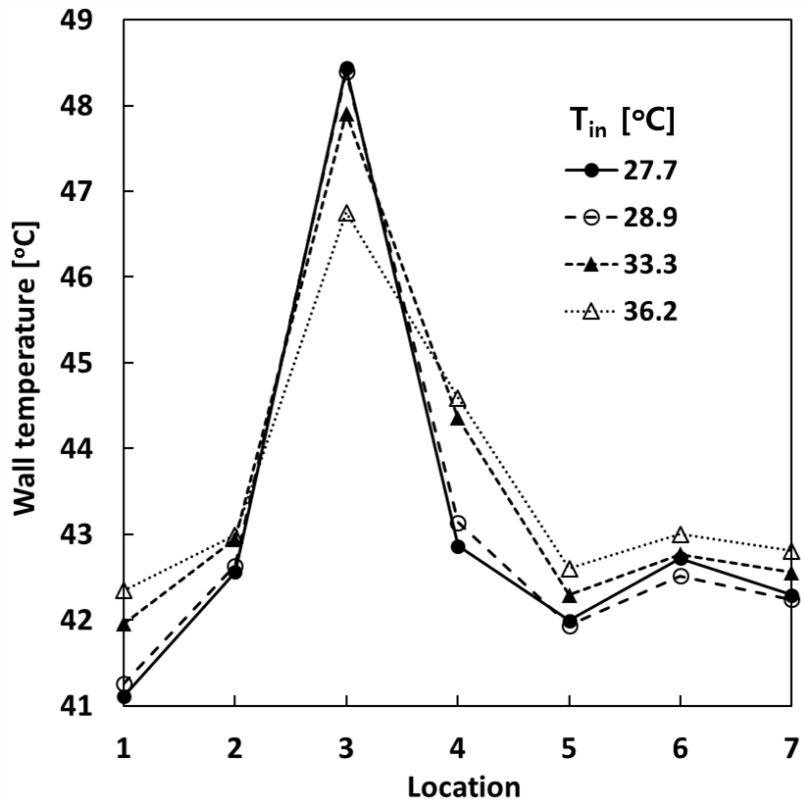

Fig. 2.7 Variation of (c) wall temperature with respect to inlet temperature and location (R245fa, G = 87.5 kg/m^2 s, T_{sat} = 40.9°C)

high. If the case of T_i = 36.2°C, vapor quality of position 1 is -0.0054. Although the quality is less than 0, a part of liquid on the surface can be boiled, which is called subcooled boiling [67]. In this case, the local heat transfer coefficient is calculated high. In the other case, the quality is close to 0 at location 2 or 3, and the heat transfer coefficient at this point is high. However, regardless of the inlet temperature, the local heat transfer coefficient of location 3 is smaller than that of the other locations. In particular, if the inlet temperature is 28.9°C, the local heat transfer coefficient is calculated as 1.739 kW/m^{2}K, which is lower than elsewhere, even though the vapor quality at location 3 is -0.0021 close to 0. On the other hand, such a sudden drop of the local heat transfer coefficient is recovered again at location 4 and 5. The local heat transfer coefficient of location 4 and 5 increases significantly again compared to that of location 3. Variation of local heat transfer coefficient is identified by the wall temperature variation of the channel. As shown in Fig. 2.7(c), the wall temperature at location 3 is much higher than elsewhere. For example, if the inlet temperature is 27.7°C, the wall temperature at location 3 is 5.6°C higher than the wall temperature at location 4. Such tendency is reduced as the inlet temperature increases. If the inlet temperature changes, the location where Onset of Nucleate Boiling (ONB) occurs in the channel changes. Since the mass flux, the channel heating and the pressure of the refrigerant in the Fig. 2.7 are the

same, it can be seen that the sudden drop of the local heat transfer coefficient at location 3 is affected based on the location of ONB in the channel. The closer the ONB is to location 3, the stronger this tendency is.

At Fig. 2.8, the cause of the sudden drop of the local heat transfer coefficient can be more clearly identified. The figure shows the local heat transfer coefficient with respect to the heat flux and vapor quality. As shown in the figure, it can be confirmed that the heat transfer coefficient increases as the DSC decreases before the vapor quality is lower than 0. After the vapor quality is 0, heat transfer coefficient decreases as the vapor quality increases. This tendency is happened when nucleate boiling is dominant [68]. Besides, heat flux has relatively small effect on the heat transfer coefficient. Moreover, the sudden drop of the local heat transfer coefficient described above section is observed again in the Fig. 2.8(a). In the area marked in red circle, even though the vapor quality of these points is close to 0, the heat transfer coefficient is significantly small compared to the other results. All of the location of sudden heat transfer drop are location 3. However, such a phenomenon isn't observed as the mass flux increases. As shown in the Fig. 2.8(b), the variation of the heat transfer coefficient due to the vapor quality and the heat flux shows a trend without exception. Thus, it can be ascertained that the sudden drop of the local heat transfer coefficient is affected by the mass flux.

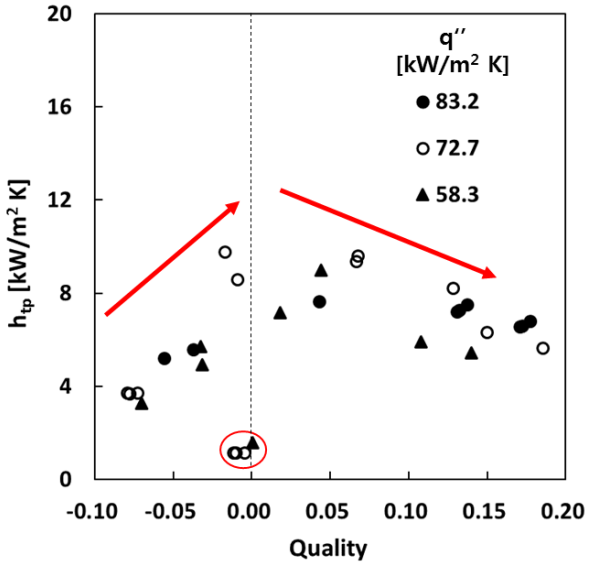

(a)

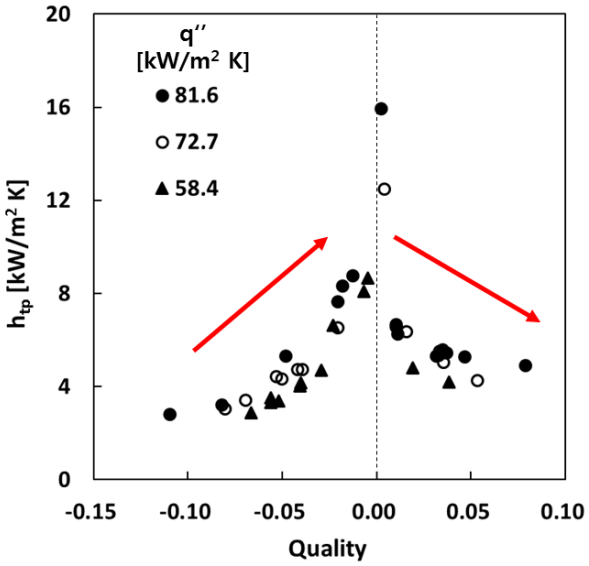

(b)

Fig. 2.8 Variation of heat transfer coefficient with heat flux and vapor quality (R245fa) (a) G = 87.5 kg/m^{2}s, (b) G = 170.9 kg/m^{2}s

In order to investigate the effect of mass flux, two cases are compared as shown in the Fig. 2.9. The figure shows the heat transfer coefficients as a function of channel heating at mass flux of 87.5 kg/m^{2}s and 170.9 kg/m^{2}s, respectively. In the low mass flux case of Fig. 2.9, as the channel heating increases, the maximum value of the local heat transfer coefficient is observed at location 5, whereas the heat transfer coefficient at location 3 decreases sharply. On the other hand, when the mass flux is 170.9 kg/m^{2}s as shown in Fig. 2.9, no sudden drop of the local heat transfer coefficient at location 3 is observed. The minimum heat transfer coefficient is obtained from location 1 and 7 close to the inlet and outlet, and the maximum heat transfer coefficient is observed from location 5. As mentioned above, variation of the local heat transfer coefficient is influenced by the location of the ONB. The location of the ONB is affected by mass flux. With the same channel heating power, the ONB moves backward with increasing mass flux. As shown in Fig. 2.10(a), when the mass flux is 87.5 kg/m^{2}s, the ONB location is close to location 3, which causes sudden drop of the local heat transfer coefficient. However, as shown in Fig. 2.10(b), when the mass flux is 170.9 kg/m^{2}s, the ONB location is around location 4 or after that. As a result, the sudden drop of heat transfer coefficient at location 3 is not observed.

The wall temperature of the channel is obtained as shown in Fig. 2.11.

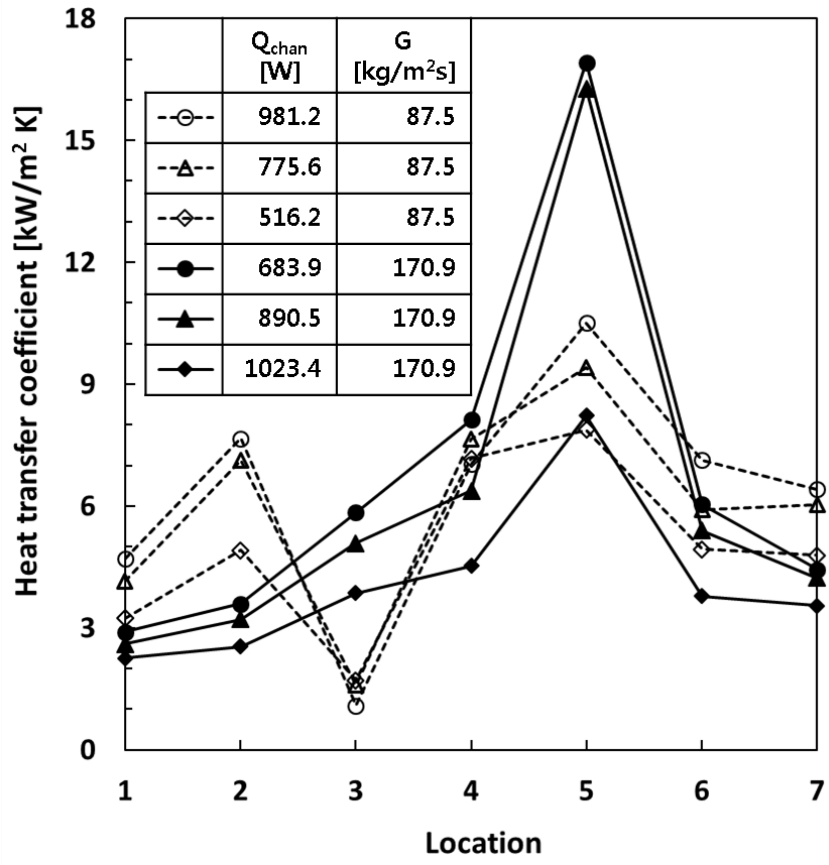

Fig. 2.9 Variation of heat transfer coefficient with channel heating power and location (R245fa)

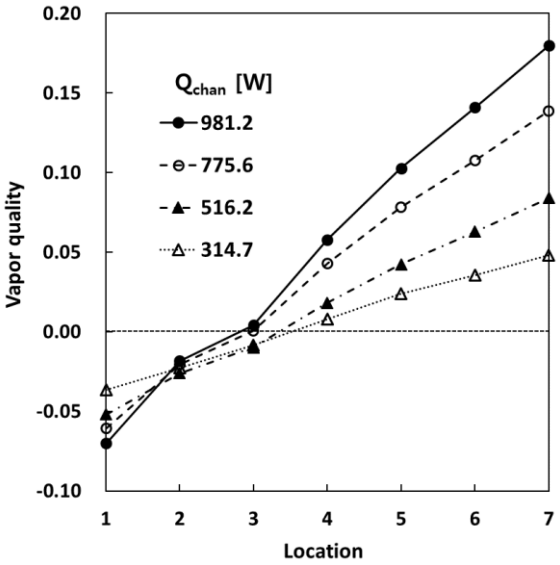

(a)

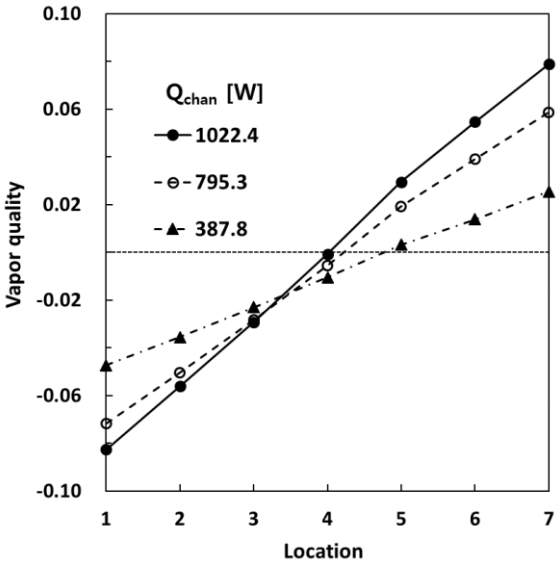

(b)

Fig. 2.10 Variation of vapor quality with channel heating power and location (R245fa) (a) G = 87.5 kg/m^{2}s, (b) G = 170.9 kg/m^{2}s

Fig. 2.11 shows the wall temperature when the mass flux is 87.5 kg/m^{2}s and 170.9 kg/m^{2}s. As can be seen in the low mass flux case of the figure, the wall temperature at location 3 rises sharply as the channel heating power increases. Since heat transfer by flow boiling does not occur well at location 3, the wall temperature at location 3 and its surroundings are high. However, when the mass flux is 170.9 kg/m^{2}s as shown in Fig. 2.11, the wall temperature is almost uniform. In fact, if the mass flux is 87.5 kg/m^{2}s and the channel heating power is 981.2 W, the maximum difference of the wall temperature reaches 18.2^{o}C. On the other hand, when the mass flux is 170.9 kg/m^{2}s and the channel heating power is 1023.4 W, the maximum deviation of the wall temperature is only 3.7^{o}C.

Similar results are confirmed in the case of R134a. Fig. 2.12 shows the results according to the mass flux when the channel heating power is 984.7 W and the refrigerant saturation temperature is 40.8^{o}C. As shown in Fig. 2.12(a), the maximum heat transfer coefficient is calculated at location 5 regardless of the mass flux. However, when the mass flux is small, the local heat transfer coefficient at location 3 decreases rapidly. Particularly when the mass flux is 20.8 kg/m^{2}s, the local heat transfer coefficient is calculated to be significantly low not only at location 3 but also at location 2 and 4. The decrease of the local heat transfer coefficient near the location 3 gradually disappear with increasing

mass flux. When the mass flux is 158.3 kg/m^{2}s, the sudden drop of the local heat transfer coefficient is hardly observed. In Fig. 2.12(b), where the mass flux is 158.3 kg/m^{2}s, the heat transfer coefficient at location 3 doesn't decrease sharply, although the location of the ONB is between the location 3 and location 4. This indicates that the sudden drop of the heat transfer coefficient can be prevented when the mass flux is large. In addition, when the mass flux is 20.8 kg/m^{2}s, the heat transfer coefficient at location 2 and 4 are calculated as low as that of location 3. In this condition, the vapor quality near the location 3 is from 0.3 to 0.5 as shown in Fig. 2.12(b). Therefore, if the vapor quality is high around location 3, the heat transfer coefficient drop would be severe. As shown in Fig. 2.12(c), the sudden drop of the heat transfer coefficient affects the wall temperature distribution. If the mass flux is 20.8 kg/m^{2}s, the wall temperature at location 3 reaches 70.3^{o}C and the temperature difference between location 2 and location 5 is 27.2^{o}C. On the other hand, when the mass flux is 158.3 kg/m^{2}s, the wall temperature at location 3 is 46.2^{o}C, which is only 3.9^{o}C different from location 5.

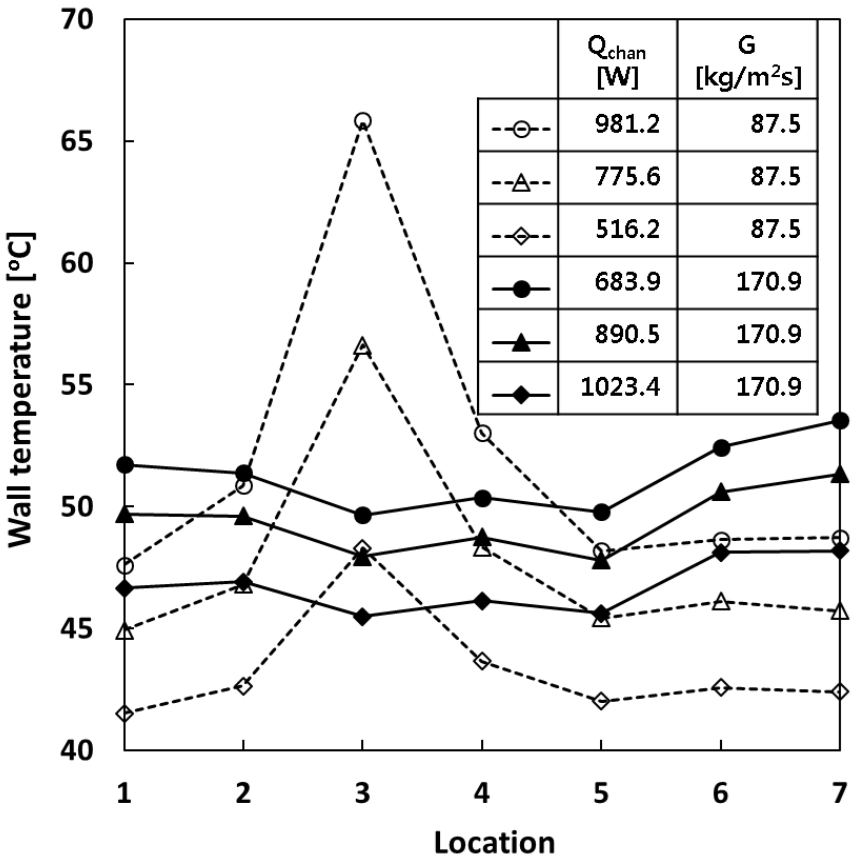

Fig. 2.11 Variation of wall temperature with channel heating power and location (R245fa)

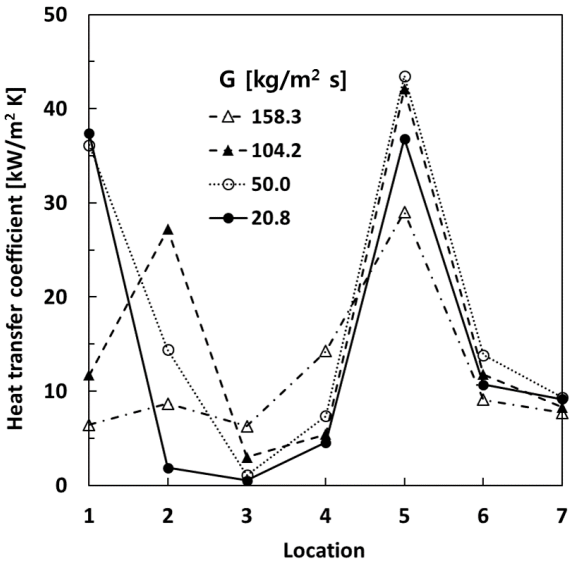

(a)

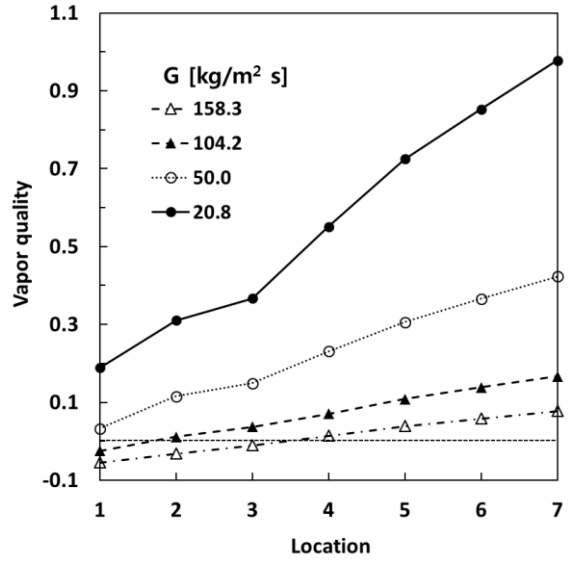

(b)

Fig. 2.12 Variation of (a) heat transfer coefficient and (b) vapor quality with mass flux and location (R134a, Q_{chan} = 984.7 W, T_{sat} = 40.8°C)

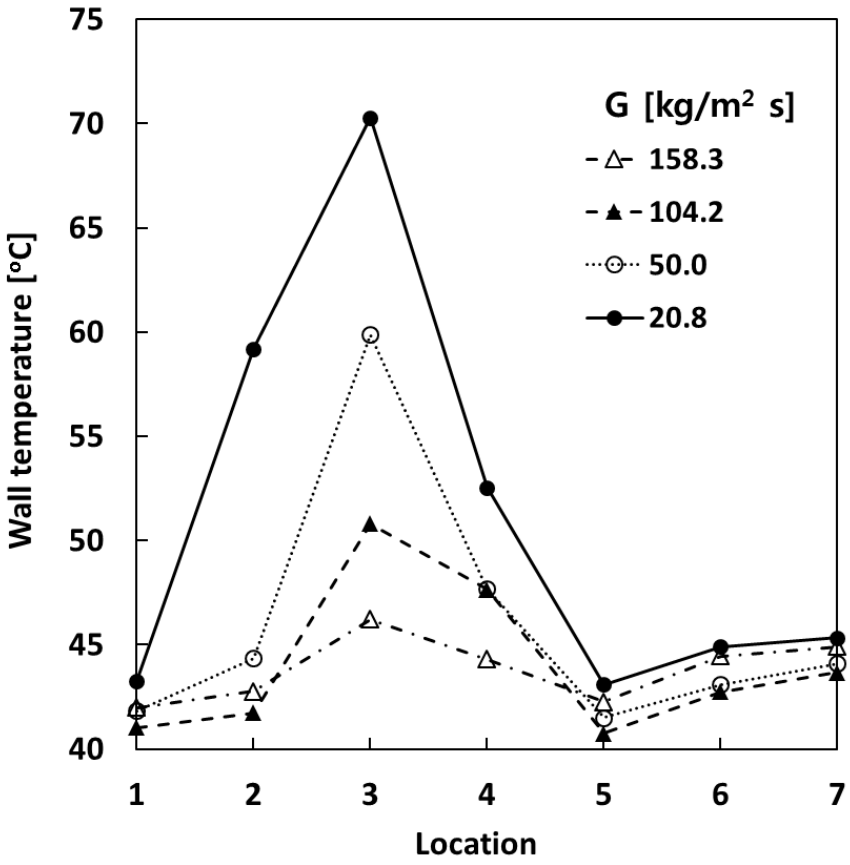

(c)

Fig. 2.12 Variation of (c) wall temperature with mass flux and location

(R134a, Q_{chan} = 984.7 W, T_{sat} = 40.8°C)

2.4.2 Bubble movement and heat transfer characteristics in curved rectangular channel

In the section 2.4.1, it is confirmed that the heat transfer coefficient changes significantly based on the location in the curved channel. The mass flux and the location of the ONB affect sudden drop of the local heat transfer coefficient dominantly. In this section, the effect of mass flux and the location of the ONB on the heat transfer is described by the results of visualization experiments. The main concern in the previous section is the heat transfer coefficient at location 3 and 5. At location 3, the sudden drop of the heat transfer coefficient based on the mass flux appeared. On the other hand, at location 5, the maximum heat transfer coefficient was obtained from all mass flux conditions. In order to confirm this, the flow boiling at two locations and the surroundings are photographed with a high-speed camera.

First, the image results of the flow boiling at location 4 which is between location 3 and 5 are shown in Fig. 2.13. The mass flux is 79.2 kg/m^{2}s, channel heating power is 445.1 W and saturated temperature of refrigerant is 29.7^{o}C. As shown in the figure, many bubbles are generated on the heated surface. If focusing on the 4 bubbles marked as red circle in the figure, bubble (a) and (b) move in the same direction as the main flow. Bubble (a) which is larger than bubble (b) moves a little faster than bubble (b). For the bubble (c), its velocity

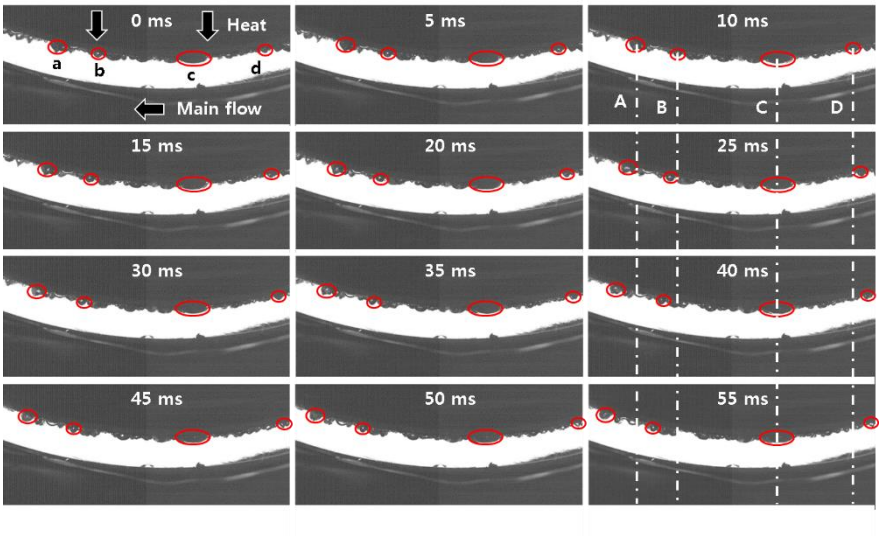

Fig. 2.13 High speed camera results of location 4

(R245fa, Q_{chan} = 445.1 W, G = 79.2 kg/m^{2}s)

is almost zero. On the other hand, bubble (d) moves in the opposite direction to the main flow. The movement of the bubble shown in the figure can be easily identified based on the 4 lines starting from the picture at 10 ms. The direction and distance of the movement of the bubbles (a), (b), (c) and (d) during 10 ms to 55 ms can be confirmed.

Fig. 2.14 shows the results of imaging the flow boiling at location 5. As shown in the right side of the figures, the bubbles generated at location 4 comes to the location 5. Moreover, all the bubbles move in the same direction as the main flow. In particular, as the size of the bubble is larger, the moving speed of the bubble is faster. If considering the three bubbles marked in the first figure, each bubble rises rapidly attaching on the heating surface. At this time, the largest bubble (a) moves the fastest. Besides, the bubble (a) eats a small bubble which is slower than bubble (a). The same tendency is observed from the bubble (b) and (c). Because the bubble (b) is faster, the distance between bubble (b) and (c) gets closer and closer. The relative velocity of marked bubbles can be compared via the dashed line (A), (B) and (C).

While, the results at location 3 are slightly different. Fig. 2.15 shows the results of imaging at location 3. As shown in the figure, almost all of the bubbles taken at this shooting angle move along the wall in an upward direction, which is opposite to the main flow. The bigger the bubble is, the faster it goes upward.

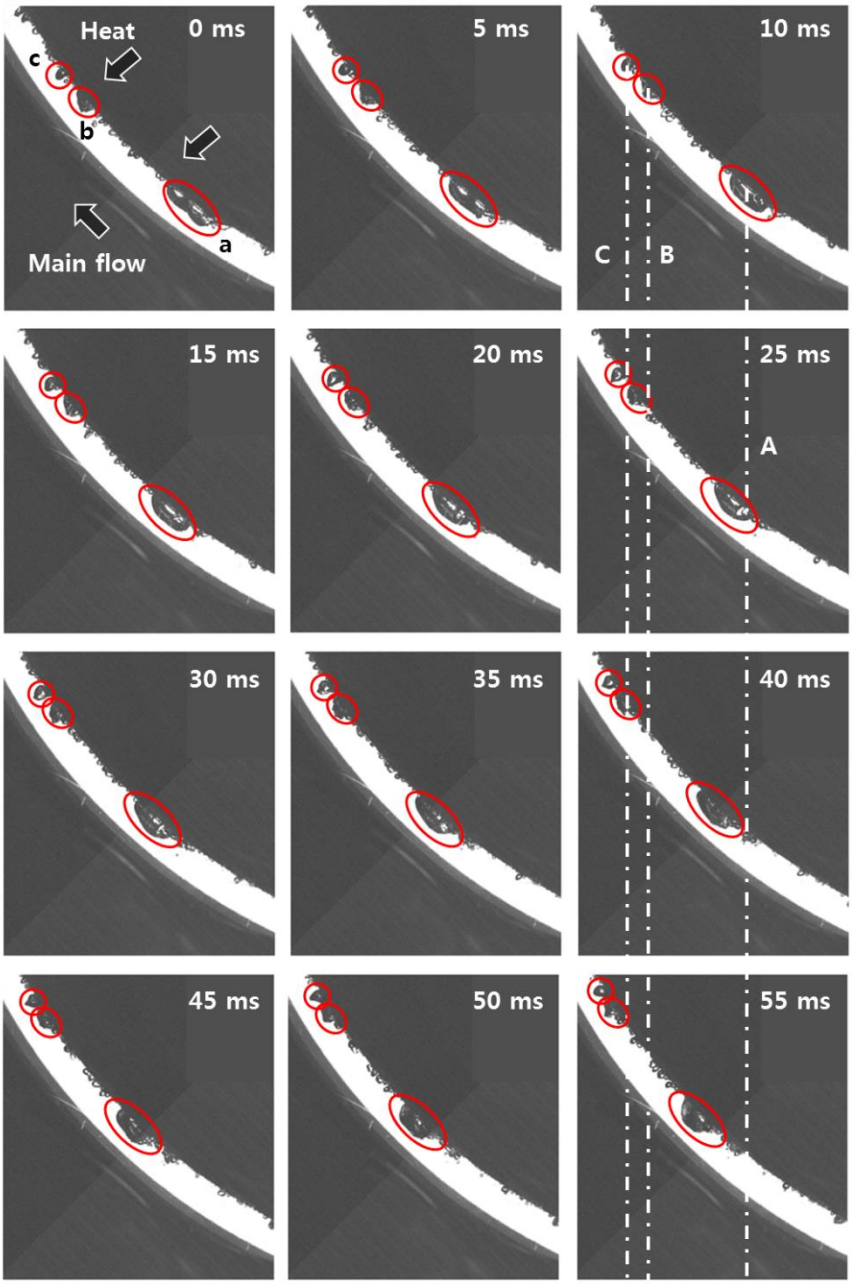

Fig. 2.14 High speed camera results of location 5

(R245fa, Q_{chan} = 445.1 W, G = 79.2 kg/m^{2}s)

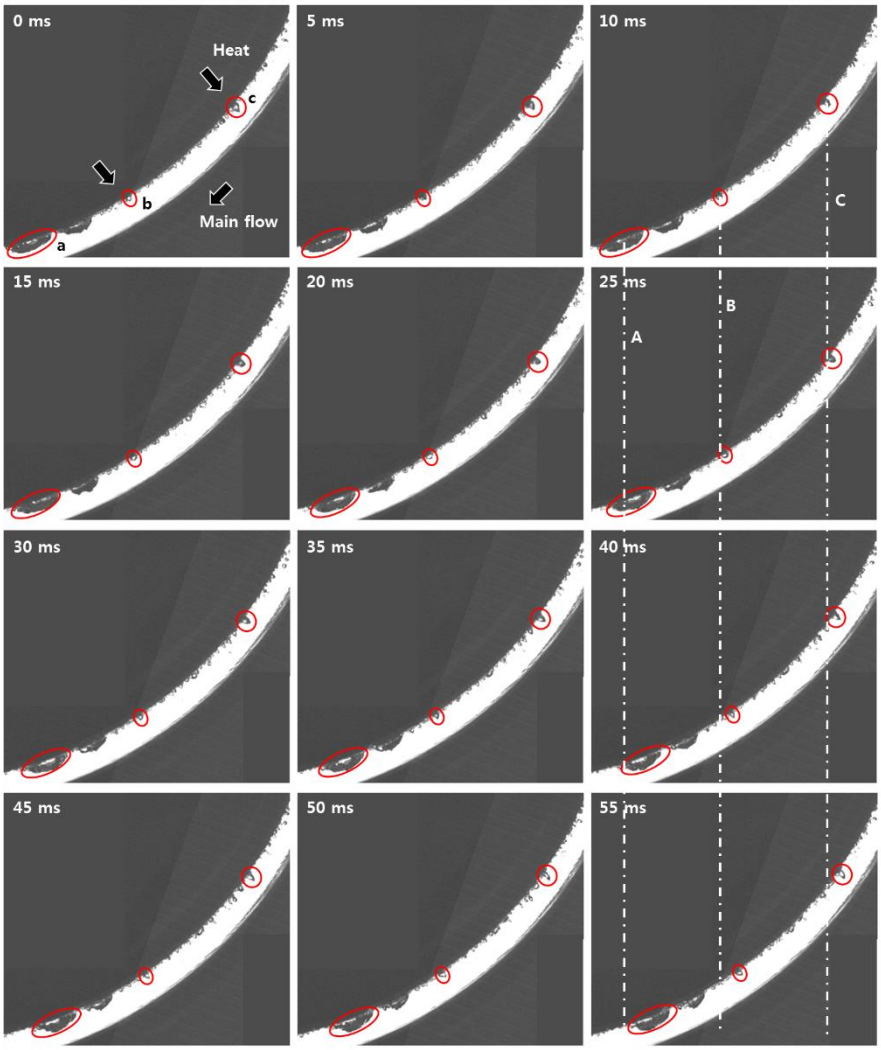

Fig. 2.15 High speed camera results of location 3

(R245fa, Q_{chan} = 445.1 W, G = 79.2 kg/m^{2}s)

In the case of the largest bubble (a), it moves faster than the other bubbles. Also, as can be seen from the bubble (c), the resistance of the main flow makes the shape of the bubble slightly flat since the bubble moves in the opposite direction to the main flow.

As described in the section 2.4.1, the sudden drop of the heat transfer coefficient appears according to the mass flux at location 3 of the curved channel. The reason of the phenomenon is found by the bubble movement observed in the visualization results. As shown in Fig. 2.15, the bubbles generated from location 3 or 4 move to the location 3. They cover the heating surface and move in the opposite direction to the main flow. For this reason, the flow boiling of the liquid on the heating surface is disturbed. Bubbles that have already vaporized prevent the heating surface, and the liquid doesn't receive heat from the heating surface. On the other hand, as shown in Fig. 2.14 of location 5, the bubbles move in the same direction as the main flow. In fact, the velocity of the bubble is faster than the velocity of the liquid. Therefore, bubbles move while pushing the liquid, and the heat transfer coefficient is improved at the heating surface. This tendency is more pronounced as the heating value of the channel increases. Therefore, the influence of the bubble movement on the variation of local heat transfer coefficient is further increased.

In order to identify the relationship between bubble velocity and heat

transfer characteristics, it is necessary to accurately predict the bubble velocity. Therefore, bubble speed is calculated using bubble dynamics. In order to calculate the velocity of the bubble, calculating the force acting on the bubble generated in the channel is essential. As shown in Fig. 2.16, there are four kinds of forces. 1) Buoyancy force, 2) drag force, 3) lift force and 4) surface tension force are them.

Firstly, the buoyancy force is calculated as Eq. (2.24).

$$F_b = (\rho_l - \rho_v)V_b g \tag{2.24}$$

Buoyancy force always acts in the opposite direction of the gravity.

The second force is drag force due to the main flow. The direction of the drag force is determined by the relative velocity between the main flow and the bubble. The drag force is calculated by Eq. (2.25) [69].

$$F_d = \frac{1}{2} C_d \rho_l \pi r_b^2 (u_\infty - v_t)|u_\infty - v_t| \tag{2.25}$$

C_d is drag coefficient, u_∞ is local liquid velocity and v_t is tangential velocity of the bubble. C_d is obtained considering flow regime of the main liquid flow as presented in Eq. (2.26) and (2.27).

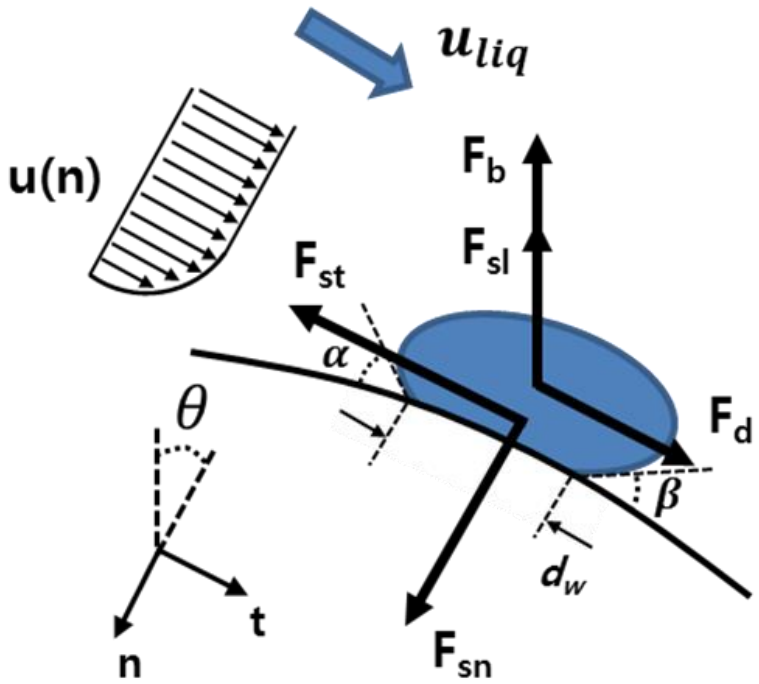

Fig. 2.16 A diagram of bubble and forces acting on the bubble

$$C_d = \begin{cases} 240 & Re_b \leq 0.1 \\ \frac{24}{Re_b}(1 + 0.15Re_b^{0.687}) & 0.1 < Re_b \leq 1000 \\ 0.44 & 1000 < Re_b \end{cases} \quad (2.26)$$

$$Re_b = \frac{2r_b|u_\infty - v_t|}{\gamma} \quad (2.27)$$

The local liquid velocity of the bubble center is evaluated by universal single phase flow profile. The dimensionless velocity of liquid flow is presented as Eq. (2.28) ~ (2.30).

$$u^+ = \begin{cases} y^+ & y^+ \leq 5 \\ 5\ln y^+ - 3.05 & 5 < y^+ \leq 30 \\ 2.5\ln y^+ + 5.5 & 30 < y^+ \end{cases} \quad (2.28)$$

$$u^+ = \frac{u}{\sqrt{\tau_w/\rho_l}} \quad (2.29)$$

$$y^+ = \frac{y\sqrt{\tau_w/\rho_l}}{\gamma} \quad (2.30)$$

τ_w is the wall shear stress and it is calculated as Eq. (2.31).

$$\tau_w = \frac{1}{2}C_f\rho_l u_\infty^2 \quad (2.31)$$

C_f is the friction coefficient. It is defined as following equations.

$$C_f = \frac{\lambda}{4} \tag{2.32}$$

$$\lambda = \begin{cases} \dfrac{64}{Re_D} & Re_D < 2000 \\ \dfrac{0.3163}{Re_D^{0.25}} & 2000 \le Re_D < 10^5 \end{cases} \tag{2.33}$$

$$Re_D = \frac{u_\infty D_h}{\mu} \tag{2.34}$$

Where, λ is the friction factor, Re_D is the Reynolds number of main flow and D_h is the hydraulic diameter of the channel.

The third force is shear lift force obtained by following equations [70-71].

$$F_{sl} = \frac{1}{2} C_l \rho_l \pi r_b^2 \left(u_{liq} - v_t\right)\left|u_{liq} - v_t\right| \tag{2.35}$$

$$C_l = 3.877 G_s^{0.5} (Re_b^{-2} + (0.344 G_s^{0.5})^4)^{0.25} \tag{2.36}$$

$$G_s = \left|\frac{du}{dn}\right| \frac{r_b}{u_{liq} - v_t} \tag{2.37}$$

Where, C_l is the shear lift force coefficient, Re_b is the Reynolds number of the bubble. The shear lift force is acting on the bubble as normal direction against the heated surface.

The last force which is considered in this paper is surface tension force. It is defined as following equations for each direction [72].

$$F_{st} = -d_w \sigma \frac{\pi(\alpha - \beta)}{\pi^2 - (\alpha - \beta)^2} (sin\,\alpha + sin\,\beta) \tag{2.38}$$

$$F_{sn} = d_w \sigma \frac{\pi}{\alpha - \beta} (cos\,\beta - cos\,\alpha) \tag{2.39}$$

α and β is the contact angle between the bubble and the surface as shown in the Fig. 2.16. d_w is contact diameter between bubble and surface. σ is the surface tension between vapor and liquid. The normal component of the surface tension force is towards the heated surface. The component in the tangential direction is determined according to the magnitude of both contact angles.

As shown in Fig. 2.16, normal direction of the coordinate is chosen as heading to the heated surface, tangential direction is selected as parallel with the direction of the main liquid flow. Based on the coordinate, bubble velocity is calculated by force balance of each direction as following equations.

$$\sum F_n = -F_b\,cos\,\theta - F_{sl} + F_{sn} = m_b \frac{dv_{b.n}}{dt} \tag{2.40}$$

$$\sum F_t = -F_b\,sin\,\theta + F_d - F_{st} = m_b \frac{dv_{b.t}}{dt} \tag{2.41}$$

θ is the angle defined as shown in the Fig. 2.16 as determined by the location of the bubble.

As shown in Fig. 2.17, at locations 3 and 5 the direction of the force to which the bubble is subjected is roughly represented. The forces that mainly affect the movement of the bubble are buoyancy force and drag force. The buoyancy force is determined according to the volume of the bubble, and the drag is determined according to the frontal area of the bubble and the mass flux of the main flow. Therefore, when the mass flux is small, the influence of the buoyancy force is dominant. In this case, the direction of the bubble movement is opposite to the main flow. As a result, as shown in Fig. 2.15, the bubble moves reversely with contacting on the heated surface.

In order to predict bubble velocity, the prediction accuracy of bubble dynamics is verified based on the results of visualization experiments. First, as shown in the Fig. 2.18, the velocity of the bubble was calculated at locations 3 and 5, respectively, based on the visualization experiment which is conducted when channel heating power is 445.1 W, mass flux of the main flow is 79.2 kg/m^2s and saturated temperature is 29.7^oC. In the figure, only the magnitude of the velocity is presented. For location 3, the direction of the bubble velocity is the reverse direction. In this condition, velocity of the main flow calculated from mass flux is 0.06 m/s. The velocity of the bubble at location 5 moves faster

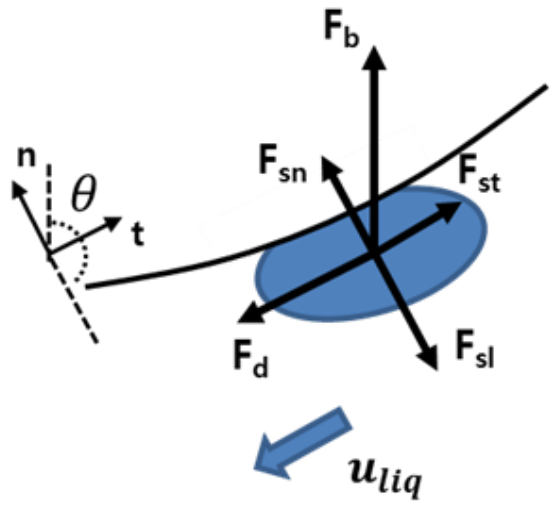

(a)

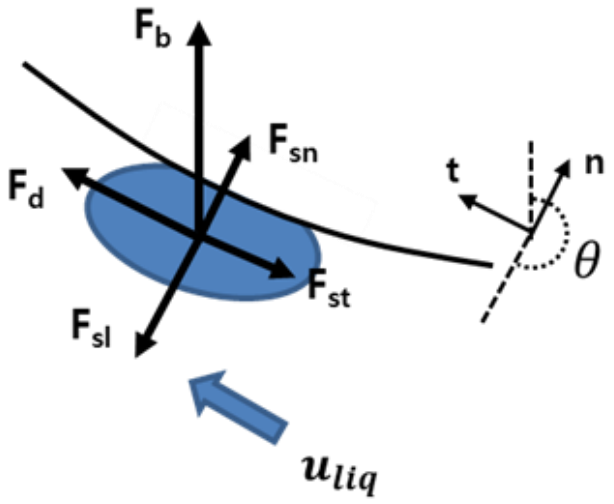

(b)

Fig. 2.17 Diagrams of bubble and forces at (a) location 3 and (b) location 5 in the channel

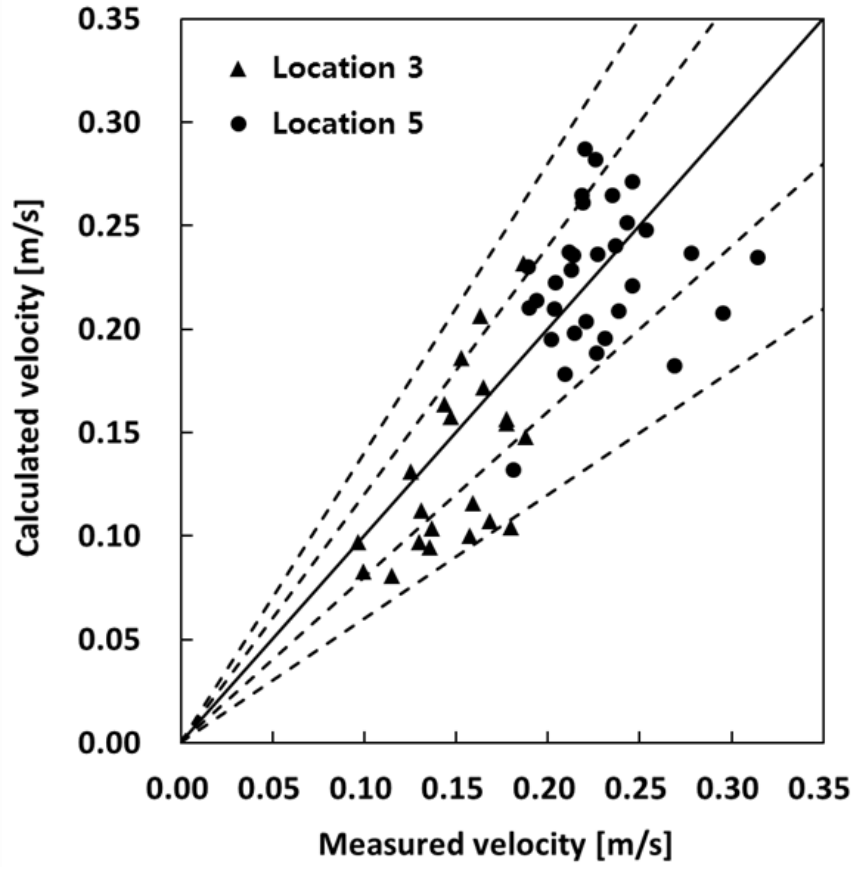

Fig. 2.18 Bubble velocity validation comparing measured velocity and calculated velocity

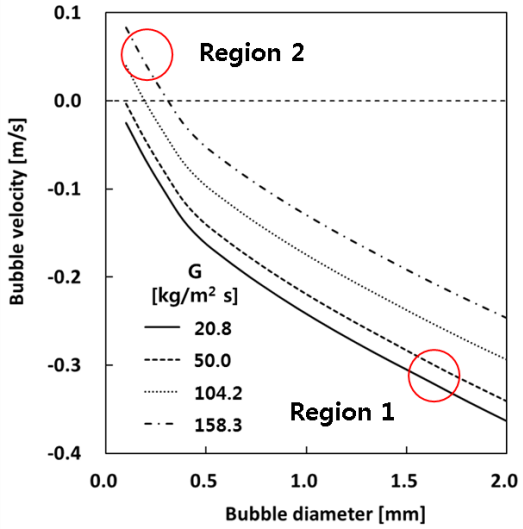

(a)

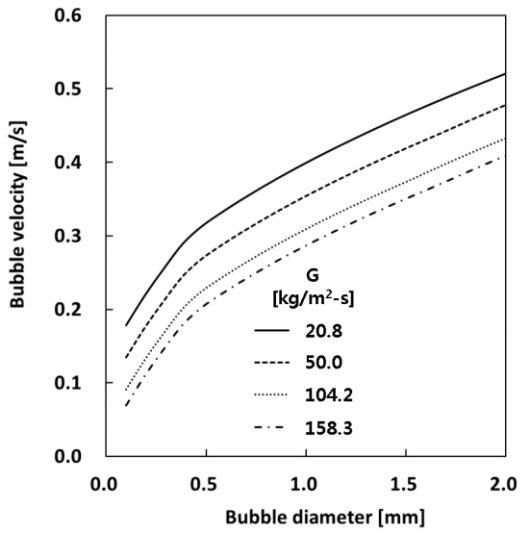

(b)

Fig. 2.19 Bubble velocity variation with bubble diameter and mass flux at (a) location 3 and (b) location 5

than the main flow. The calculated results by bubble dynamics and the results calculated through visualization experiments are compared in Fig. 2.18. As shown in the figure, all 51 results are predicted within an error range of 40.0%, and the average error is 19.8%.

The velocity of the bubble can be calculated using these method to explain the variation of the local heat transfer coefficient with location on the channel. Fig. 2.19(a) shows the calculated bubble velocity at location 3 according to the bubble size in the experiment conducted using R134a under the conditions of Fig. 2.12. The bubble is assumed to be elliptical in shape. As shown in the figure, as the bubble size increases or the mass flux decreases, the magnitude of the reverse velocity increases. In particular, when focusing on the region 1 and region 2 as shown in the figure, region 1 is a condition with a low mass flux. If the mass flux is small, the vapor quality becomes higher under the same channel heating condition as presented in Fig. 2.12(b), which means that the number of large bubbles increases. In this case, many of the bubbles are moving reversely with fast velocity. Because they disturb liquid boiling on the heated surface, heat transfer coefficient at location 3 is suddenly dropped. On the other hand, at region 2, as the mass flux increases, small bubbles are expected to move parallel to the main flow. When the mass flux is high, as shown in Fig. 2.12(b), most of the bubbles are small because the vapor quality at location 3 is small.

Therefore, most bubbles can be predicted by moving in the same direction as the main flow. In fact, the sudden drop of the local heat transfer coefficient with a large mass flux is mitigated, and the reason can be found in the movement of the bubbles parallel to the main flow. In the case of location 5, the velocity increases as the bubble size increases as shown in Fig. 2.19(b). The bubble boosts the liquid on the heated surface because the bubble velocity is faster than the velocity of the main flow. Therefore, the heat transfer performance is improved at location 5.

2.5 Summary

In order to investigate the flow boiling heat transfer characteristics in the curved rectangular channel, experiments for heat transfer coefficient measurement using R245fa and R134a and visualization experiments using R245fa are conducted.

Based on the location in the channel, the variation of the local heat transfer coefficient is observed, which is dominated by the mass flux and the vapor quality with location. The sudden drop of the local heat transfer coefficient in the vicinity of location 3 at low mass flux is identified. On the other hand, near the location 5, the local heat transfer coefficient is significantly increased. It is confirmed by the high wall temperature near the location 3. Moreover, as the

channel heating power increases and the inlet temperature of the channel increases, the sudden drop of the local heat transfer coefficient occurs violently. This is because boiling started rapidly in the channel, and the vapor quality increases significantly.

Variation of the local heat transfer coefficient within the channel is investigated considering bubble movement in the channel. If the mass flux is low, bubbles generated on the heating surface is affected by the buoyancy force dominantly. For location 3 in the channel, the buoyancy force forces the bubble in the opposite direction to the main flow. This prevents bubbles from detaching to the heating surface and boiling the liquid on the heated surface. On the other hand, at location 5, the bubble pushes the liquid on the heated surface moving faster than the main flow due to the buoyancy force. It improves the local heat transfer performance on the location 5. When the mass flux is increased, the drag force acting on the bubbles is increased. As a result, the number of the bubble moving parallel to the main flow increases at the location 3. Especially when the mass flux increases, the vapor quality is lower with the same channel heating power, which means that the number of small bubbles is increased. For the small bubbles, they have been more affected by drag force than by the buoyancy force, and moves parallel to the main flow. Therefore, the sudden drop of the local heat transfer coefficient at location is mitigated.

Chapter 3. Numerical study on the motor cooling performance of flow boiling using lumped parameter thermal model

3.1 Introduction

In this chapter, flow boiling cooling system has been proposed which can replace the existing water cooling system for an electric motor. While using the existing cooling channel in the same manner, it is intended to achieve an improvement in cooling performance by improving the heat transfer performance through flow boiling heat transfer. Therefore, the comparison of the cooling performance is conducted when the water cooling system and the flow boiling cooling system are applied to the motor. In order to evaluate the cooling performance of the motor, as described in Chapter 1, the temperature of the winding is observed mainly. Lowering the temperature of the winding can reduce the risk of the motor failure and extend the motor life time. In addition, the joule loss which is the main part of the motor heat loss can be reduced. Therefore, the cooling performance of both water cooling and flow boiling cooling is compared based on the temperature variation of the motor winding under the same driving conditions.

First, fully lumped parameter thermal model for motor is developed to accurately calculate the temperature variation of the motor winding and other positions. In consideration of the shape of the motor, a three-dimensional model is developed based on the cylindrical coordinate. Heat transfer on the cylindrical coordinate, temperature change of the solid and fluid during driving, and heat generation at each position according to the motor operating conditions are all taken into consideration for the model. The developed model is verified in comparison with the experimental results. By the developed motor model, temperature inside the motor which is difficult to measure by using sensor can be calculated.

The developed model is used to compare water cooling and flow boiling cooling. Variation of the motor winding temperature and heat loss of motor are calculated while changing the flow rate and inlet temperature under the same driving conditions. Improved cooling performance using flow boiling is confirmed as superior to that of water cooling system under the same pump power consumption. However, in the case of flow boiling cooling, the cooling performance is degraded when the mass flow rate is small due to the vaporization of the refrigerant. Therefore, when the inlet temperature and mass flow rate were properly selected, the winding temperature of the motor could be lowered compared to the existing water cooling method. Furthermore, lower

winding temperature makes joule loss smaller. As a result, motor efficiency could be improved. Because cooling performance of the flow boiling is enough to cool the existing motor, the motor power output can be improved using the same pump power.

3.2 Theoretical model

3.2.1 Thermal circuit in the cylindrical coordinate

Considering the shape of the motor, it is appropriate to represent the motor in a cylindrical coordinate rather than in the Cartesian coordinate. In the case of existing water cooling method, a temperature difference occurs not only in the r-direction but in both the theta-direction and the z-direction. Therefore, fully lumped parameter thermal model which considers heat transfer in a three-dimensional cylindrical coordinate is required. Discretized cells must be divided into levels that can guarantee both computational speed and accuracy.

The basic cell in the cylindrical coordinate system is displayed as shown in Fig. 3.1. When the mean temperature of the cell is $T_{m,c}$, the boundary temperature is presented as shown in the figure. Considering the relationship between the total energy stored in the cell and the mean temperature, Eq. (3.1)

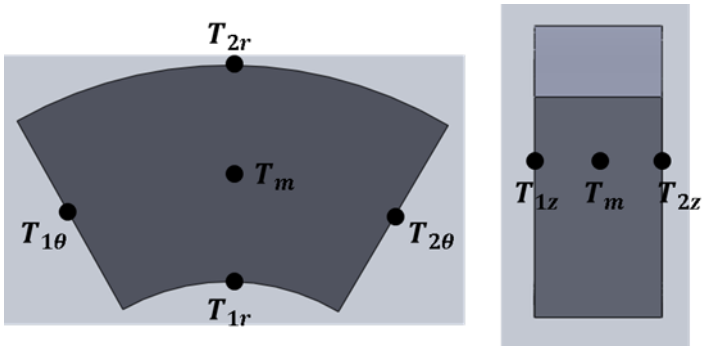

Fig. 3.1 Discretized cell and temperature notation in the cylindrical coordinate

is derived.

$$E_{str,c} = \rho_c V_c c_{p,c} T_{m,c} \tag{3.1}$$

$E_{str,c}$ is the total energy stored in the discretized cell. A small element which is assumed as uniform temperature has energy inside of the element as Eq. (3.2).

$$dE_{str,e} = \rho_e c_{p,e} T_e dV \tag{3.2}$$

Because an element is inside of the cell, $\rho_e = \rho_c$ and $c_{p,e} = c_{p,c}$. In the cylindrical coordinate, volume element is presented as Eq. (3.3).

$$dV = r d\theta dz dr \tag{3.3}$$

Because energy balance should be satisfied for the discretized cell, total energy stored in the cell is presented as Eq. (3.4).

$$E_{str} = \int dE_{str} \tag{3.4}$$

As a result, mean temperature of the cell is described as Eq. (3.5).

$$T_m = \frac{1}{V}\int T r d\theta dz dr \tag{3.5}$$

Heat transfer of each direction is assumed as independent. Then, mean temperature of each direction is calculated as Eq. (3.6) ~ (3.8).

$$T_{m,r} = \frac{2}{r_2^2 - r_1^2}\int_{r_1}^{r_2} T(r) r dr \tag{3.6}$$

$$T_{m,\theta} = \frac{1}{\theta_0}\int_{\theta_1}^{\theta_2} T(\theta) d\theta \tag{3.7}$$

$$T_{m,z} = \frac{1}{z_0}\int_{z_1}^{z_2} T(z) dz \tag{3.8}$$

Based on the derived mean temperature of the discretized cell in the cylindrical coordinate, heat resistance is obtained as follows [73]. To derive heat resistance of each direction, heat dissipation equation and Fourier's law of conduction is considered as Eq. (3.9) ~ (3.10).

$$\frac{1}{r}\frac{\partial}{\partial r}\left(k_r r \frac{\partial T}{\partial r}\right) + \frac{1}{r^2}\frac{\partial}{\partial \theta}\left(k_\theta \frac{\partial T}{\partial \theta}\right) + \frac{\partial}{\partial z}\left(k_z \frac{\partial T}{\partial z}\right) + \dot{q} = \rho c_p \frac{\partial T}{\partial t} \tag{3.9}$$

$$q'' = -k\left(\vec{\imath}\frac{\partial T}{\partial r} + \vec{\jmath}\frac{1}{r}\frac{\partial T}{\partial \theta} + \vec{k}\frac{\partial T}{\partial z}\right) \tag{3.10}$$

From the assumption of independent heat transfer in each direction,

temperature distribution is obtained as Eq. (3.11) in r-direction.

$$T(r) = -\frac{\dot{q}}{4k}r^2 + C_1 \ln r + C_2 \tag{3.11}$$

Where, $\mathrm{T}(r_1) = T_{1,r}$ and $\mathrm{T}(r_2) = T_{2,r}$ as boundary condition. From Eq. (3.6), mean temperature for r-direction is calculated using Eq. (3.12).

$$T_{m,r} = T_{2,r}\left[\frac{r_2^2}{r_2^2 - r_1^2} - \frac{1}{2\ln(r_2/r_1)}\right] + T_{1,r}\left[\frac{1}{2\ln(r_2/r_1)} - \frac{r_1^2}{r_2^2 - r_1^2}\right] + \frac{\dot{q}(r_1^2 + r_2^2)}{8k} - \frac{\dot{q}(r_2^2 - r_1^2)}{8k\ln(r_2/r_1)} \tag{3.12}$$

If $\dot{q} = 0$, the mean temperature can be described as Eq. (3.13) considering thermal circuit in r-direction.

$$T_{m,r} = T_{1,r}\frac{R_{2,r}}{R_{1,r} + R_{2,r}} + T_{2,r}\frac{R_{1,r}}{R_{1,r} + R_{2,r}} \tag{3.13}$$

$R_{1,r}$ means heat resistance between boundary temperature of $T_{1,r}$ and mean temperature of $T_{m,r}$. $R_{2,r}$ is heat resistance between boundary temperature of $T_{2,r}$ and mean temperature of $T_{m,r}$. From Eq. (3.12) and (3.13), heat resistances are obtained as Eq. (3.14) and (3.15).

$$R_{1,r} = \frac{1}{2\theta_0 k_r z_0}\left[\frac{2r_2^2 \ln(r_2/r_1)}{r_2^2 - r_1^2} - 1\right] \tag{3.14}$$

$$R_{2,r} = \frac{1}{2\theta_0 k_r z_0}\left[1 - \frac{2r_1^2 \ln(r_2/r_1)}{r_2^2 - r_1^2}\right] \tag{3.15}$$

When $\dot{q} \neq 0$, additional heat resistance $R_{m,r}$ is adopted [74]. $R_{m,r}$ is virtual heat resistance between mean temperature and central temperature of the cell. In the case of no heat generation, temperature of the cell center is equal to mean temperature. However, heat generation is non zero, temperature of the cell center can be different with mean temperature. Thermal circuit with non-zero heat generation is presented as Fig. 3.2. For the convenient, $T_{1,r}$ and $T_{2,r}$ are equal to zero. Then, the mean temperature of the cell is presented as Eq. (3.16).

$$T_{m,r} = \dot{q} V_c \left[R_{m,r} + \frac{R_{1,r} R_{2,r}}{R_{1,r} + R_{2,r}}\right] \tag{3.16}$$

Using Eq. (3.12) and (3.16), $R_{m,r}$ is obtained as Eq. (3.17).

$$R_{m,r} = \frac{-1}{4\theta_0 k_r z_0 (r_2^2 - r_1^2)}\left[r_1^2 + r_2^2 - \frac{4r_1^2 r_2^2 \ln(r_2/r_1)}{r_2^2 - r_1^2}\right] \tag{3.17}$$

In the same manner, heat resistance of each direction is derived as Eq. (3.18) ~ (3.23).

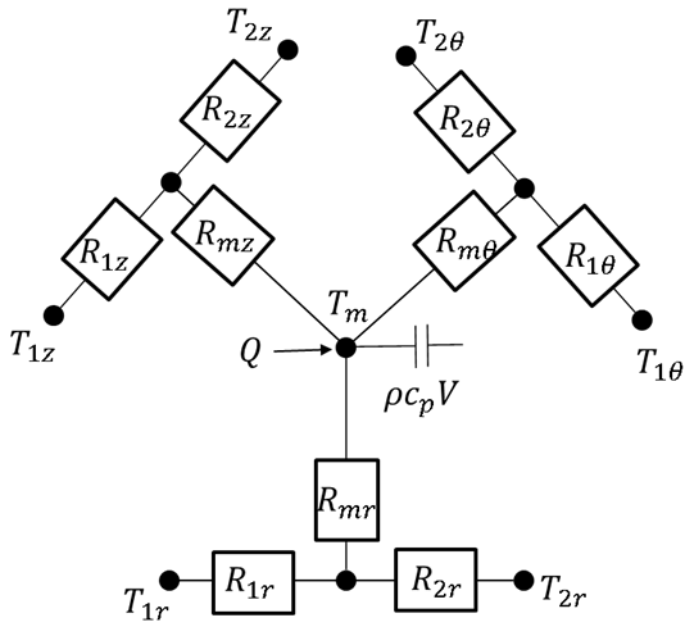

Fig. 3.2 Thermal circuit of the discretized cell in the cylindrical coordinate

$$R_{1,\theta} = \frac{\theta_0(r_1 + r_2)}{4k_\theta z_0(r_2 - r_1)} \tag{3.18}$$

$$R_{2,\theta} = R_{1,\theta} \tag{3.19}$$

$$R_{m,\theta} = -\frac{\theta_0(r_1 + r_2)}{12k_\theta z_0(r_2 - r_1)} \tag{3.20}$$

$$R_{1,z} = \frac{z_0}{k_z \theta_0(r_2^2 - r_1^2)} \tag{3.21}$$

$$R_{2,z} = R_{1,z} \tag{3.22}$$

$$R_{m,z} = -\frac{Z_0}{3k_z \theta_0(r_2^2 - r_1^2)} \tag{3.23}$$

Based on the heat resistances derived before, thermal circuit of discretized cell for fully lumped parameter thermal model is presented as Fig. 3.2. For the derived thermal circuit, the mean temperature of each direction is assumed as the same. All of the discretized cell inside motor is represented as thermal circuit as shown in the Fig. 3.2.

3.2.2 Loss calculation model

One of the most important thing for the motor thermal model is heat loss calculation. An accurate prediction of heat loss is necessary to precisely calculate the variation of the temperature inside the motor. The main heat losses generated in the motor are three kinds.

The first one is the Joule loss. This is heat generation due to the current of the motor winding. The Joule loss is calculated as Eq. (3.24).

$$Q_{Joule} = 3I_{rms}^2 R_w \tag{3.24}$$

The '3' represents three phase because general electric motor for electric vehicle has three phase. I_{rms} means root mean square current based on the AC current. R_w is electric resistance of the winding.

R_w is obtained as Eq. (3.25).

$$R_w = \rho_0(1 + a_w T_w)\frac{L_w}{A_w} \tag{3.25}$$

ρ_0 is resistivity at the reference temperature. a_w is a constant for relationship between resistivity and temperature of the winding. T_w is the temperature of the winding. L_w and A_w are length and cross section area of the winding.

The second heat loss is iron loss. Iron loss occurs when iron moves in a magnetic field. The stator and the rotor are made of iron lamination. As the permanent magnet inserted into the rotor rotates and the magnitude of the current flowing through the winding changes, the magnetic field acting on the

stator and the rotor continuously changes. This causes iron loss in the stator and the rotor. Iron loss is typically composed of eddy current loss and hysteresis loss. The iron loss is calculated by the following equation [75].

$$Q_{ie} = \frac{k_e(f)D}{2\pi^2}\int_{iron}\frac{1}{N}\sum_{k=1}^{N}\left\{\left(\frac{B_r^{k+1}-B_r^k}{\Delta t}\right)^2+\left(\frac{B_\theta^{k+1}-B_\theta^k}{\Delta t}\right)^2\right\}dv \quad (3.26)$$

$$Q_{ih} = \frac{k_h(f)D}{T}\sum_{i=1}^{NE}\frac{\Delta V_i}{2}\left(\sum_{j=1}^{N_{pr}^i}\left(B_{mr}^{ij}\right)^2+\sum_{j=1}^{N_{p\theta}^i}\left(B_{m\theta}^{ij}\right)^2\right) \quad (3.27)$$

Q_{ie} is eddy current loss and Q_{ih} is hysteresis loss. B means magnetic flux density. f is the frequency of the magnetic field. By integrating the magnetic flux density depending on the position with respect to the time, it is possible to calculate the iron loss of the total motor. Eq. (3.26) and (3.27) can be simplified as follows to easily calculate the iron loss of the motor.

$$Q_{iron} = k_h B_{max}^{\beta}\omega + k_e B_{max}^2\omega^2 \quad (3.28)$$

k_h is the hysteresis coefficient and k_e is eddy current coefficient. ω_s is angular velocity of the motor. Bmax is maximum magnetic flux density of the rotor or the stator.

The third heat loss is mechanical loss. It is generated due to the friction of the bearing. Although the mechanical loss accounts for about 3% of the heat loss of the entire motor [76], it is difficult to directly affect the temperature of winding and the rotor in the motor. Because it is difficult to transmit to the motor inside. The mechanical loss is transferred to the motor shaft or bearings directly. Therefore, in this study, the mechanical loss is not included when calculating the heat loss of the motor.

In order to accurately calculate the heat loss with respect to the motor operating conditions, the heat losses of the motor are calculated based on the equations (3.24) to (3.28). The calculation is conducted using the Altair FluxMotor 2018 [77]. The heat loss according to the motor operating conditions is calculated as shown in Fig. 3.3. As shown in the figure, the heat loss corresponding to the motor torque and its rotational speed is calculated. Total heat loss is divided into Joule loss and iron loss, and is imposed based on the position in the motor. In particular, the Joule loss is greatly affected by the winding temperature. The Fig. 3.3(a) is a total loss map when the motor temperature is 30^{o}C, and the Fig. 3.3(b) is a total loss map when the motor temperature is 150^{o}C. As shown in the figure, depending on the temperature, a difference of the total loss is varied up to 1.5 kW. In the developed motor thermal model, the loss change due to the winding temperature is considered.

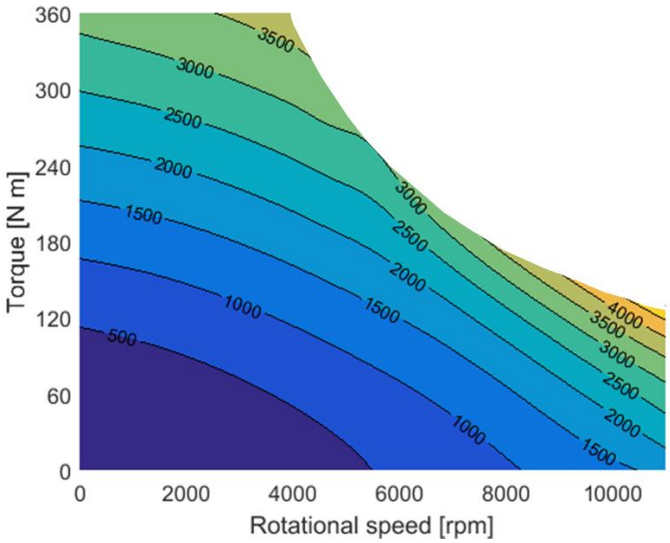

(a)

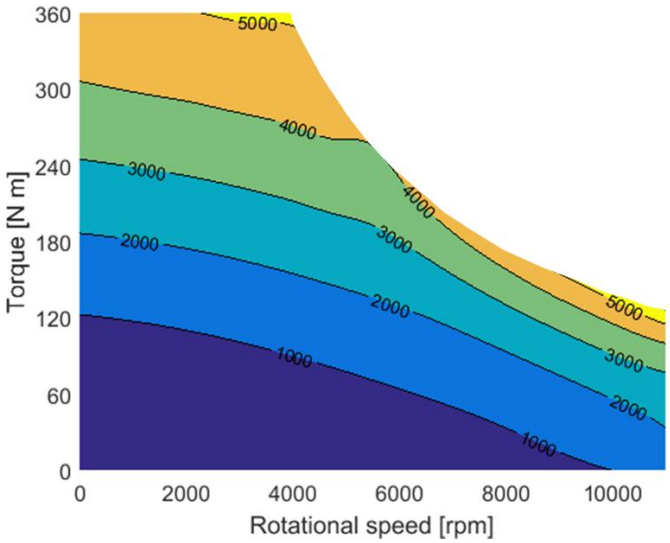

(b)

Fig. 3.3 Total motor heat loss when the motor temperature is

(a) 30ºC and (b) 150ºC

3.2.3 Heat transfer model for fluid

In order to compare motor cooling performance of water and refrigerant, proper heat transfer coefficient correlation is needed. First, in the case of water, the correlation proposed by Rogers et al. [78] is used.

$$Nu = 0.023Re^{0.8}Pr^{0.4}\left(\frac{d_{h,ch}}{D_{ch}}\right)^{0.1} \tag{3.29}$$

$d_{h,ch}$ is the hydraulic diameter of the channel path. D_{ch} is the diameter of the curved channel.

In the case of flow boiling cooling using a refrigerant, the following two correlations are used depending on the range of the vapor quality. When $0 \leq x \leq 0.4$, heat transfer coefficient is obtained by Chen et al. [20] as presented in Eq. (3.30)~(3.31).

$$\frac{Nu_{tp}}{Nu_{lo}} = 2.84\left(\frac{1}{X_{tt}}\right)^{0.27} + (46162Bo^{1.15} - 0.88) \tag{3.30}$$

$$X_{tt} = \left(\frac{1-x}{x}\right)^{0.9}\left(\frac{\rho_g}{\rho_l}\right)^{0.5}\left(\frac{\mu_l}{\mu_g}\right)^{0.1} \tag{3.31}$$

Where, Nu_{tp} is the Nusselt number of two-phase refrigerant and Nu_{lo} is the Nusselt number of liquid-only refrigerant. Nu_{lo} is obtained from Eq. (3.29). ρ

is the density. μ is the kinematic viscosity. Bo is the boiling number and it is calculated as $\mathrm{Bo} = q''/Gh_{lv}$. When $0.4 < \mathrm{x} < 1$, the correlation proposed by Cui et al. [22] is used as presented in Eq. (3.32) and (3.33).

$$Nu_{tp} = 8.76Re_m^{0.6}Pr_l^{1/6}\left(\rho_g/\rho_l\right)^{0.2}\left(k_g/k_l\right)^{0.09}Dn_m^{0.1}N_{CB}^{-0.414} \tag{3.32}$$

$$N_{CB} = \left(\frac{h_{lg}G}{q''}\right)\left[1 + x\left(\frac{\rho_l}{\rho_g} - 1\right)\right]\left(\frac{\rho_g}{\rho_l}\right)^{\frac{1}{3}} \tag{3.33}$$

Where, N_{CB} is the convective boiling coefficient. Two-phase mixture Reynolds number, Re_m, is defined as Eq. (3.34).

$$Re_m = \frac{Gd_{h,ch}}{\mu_l}\left[1 + x\left(\frac{\rho_l}{\rho_v} - 1\right)\right] \tag{3.34}$$

The mixture Dean number, Dn_m, is defined as Eq. (3.35).

$$Dn_m = Re_m\left(\frac{d_{h,ch}}{D_{ch}}\right)^{\frac{1}{2}} \tag{3.35}$$

If refrigerant is single phase as liquid or vapor state, Eq. (3.29) is used for flow boiling heat transfer coefficient.

One of the most important heat transfer coefficients in motor thermal

analysis is the convective heat transfer coefficient at the air gap. There is very small gap between the high speed rotating rotor and the stator. The convective heat transfer coefficient of air in the air gap is different from the general convective heat transfer coefficient of air because of the rotor rotation. When the boundary rotates rapidly near a small gap, the flow of air inside can be described by the Taylor number [79]. The Taylor number is defined as follows.

$$Ta_m = \frac{\omega_{rot} r_m^{0.5} r_{sta} - r_{rot}^{1.5}}{\nu_{air}} \tag{3.36}$$

Ω_{rot} is rotational speed of the rotor. r_{sta} is inner radius of the stator and r_{rot} is the radius of the rotor. r_m is the mean radius of r_{sta} and r_{rot}. ν is the kinematic viscosity of the air. Geometrical factor F_g is defined as Eq. (3.37) for considering air gap flow regime [80].

$$F_g = \frac{\pi^2}{Ta_{m,cr}\sqrt{S}}\left(1 - \frac{r_{sta} - r_{rot}}{2r_m}\right)^{-1} \tag{3.37}$$

Where, S and S_r are defined as following equation.

$$S = 0.0571 S_r + 0.00056 {S_r}^{-1} \tag{3.38}$$

$$S_r = 1 - 0.652\frac{(r_{sta} - r_{rot})/r_m}{1 - (r_{sta} - r_{rot})/(2r_m)} \tag{3.39}$$

At low Taylor number, $Ta_m^2/F_g^2 < 1700$, the flow inside the air gap is a laminar shear flow. In this condition, convective heat transfer coefficient of air in the air gap is calculated using the correlation proposed by Bjorklund et al. [81].

$$Nu_{gap} = \frac{2[(r_{sta} - r_{rot})/r_{rot}]}{\ln[1 + (r_{sta} - r_{rot})/r_{rot}]} \tag{3.40}$$

When $1700 \leq Ta_m^2/F_g^2 < 10^4$, air flow is laminar with vortices. The heat transfer coefficient is obtained by Becker et al. [82-83].

$$Nu_{gap} = 0.128\left(Ta_m^2/F_g^2\right)^{0.367} \tag{3.41}$$

If Taylor number is increased with increasing rotational speed ($10^4 \leq Ta_m^2/F_g^2 < 10^7$), the flow is turbulent. Heat transfer coefficient is calculated by Becker et al. [82-83].

$$Nu_{gap} = 0.409\left(Ta_m^2/F_g^2\right)^{0.241} \tag{3.42}$$

From the above mentioned Nusselt number, air gap heat transfer coefficient is calculated as Eq. (3.43).

$$h_{gap} = Nu_{gap} \frac{k_{air}}{D_{h,gap}} \tag{3.43}$$

$$D_{h,gap} = 2(r_{sta} - r_{rot}) \tag{3.44}$$

3.2.4 Fully lumped parameter thermal model for motor

Based on the above mentioned equations, fully lumped parameter thermal model for electric motor with external cooling jacket is developed. Fig. 3.4 shows discretized motor. The cell is divided as the same number of winding in the θ-direction. In this direction, stator is divided into 5 cells as presented in the Fig. 3.4. The rotor and the permanent magnet isn't discretized in the theta direction. Because, rotor of the motor rotates fast during the driving, temperature distribution of the rotor on the θ-direction can be ignored. Therefore, the rotor and the permanent magnet is divided only for z-direction as shown in the Fig. 3.4. The number of the cell on the z-direction is determined by the number of the parallel coolant path. For the target motor, coolant channel has 4 paths. When the coolant comes to the channel, it is divided into 2 channels. They turn around the motor twice and merge with each other at the exit. Thus,

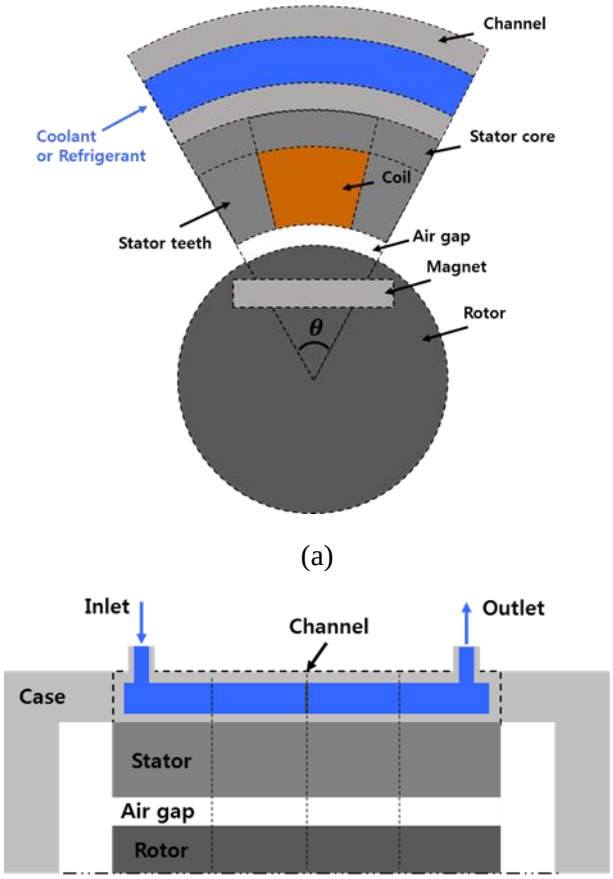

Fig. 3.4 Schematics of the motor considered in the model for (a) r and θ direction and (b) z direction

a temperature distribution in the z-direction occurs alongside the water cooling channel. The motor case is also considered in the motor model. Because the case has a large heat capacity, it is important in calculating the temperature variation of the motor with respect to time.

The geometric parameters and specification of the analyzed motor for the analysis are shown in Table 3.1. In addition, the thermodynamic properties used for numerical analysis are shown in Table 3.2.

Fully lumped parameter thermal model is developed based on the theoretical equations, physical properties and geometric parameters described above. The integrated thermal circuit used in the model is presented as Fig. 3.5. As shown in Fig. 3.5(a), in the case of the r-direction, thermal circuit is linked from the rotor inside of the motor to the cooling channel. The channel is connected with the ambient air. As shown in Fig. 3.5(b), the θ-direction heat transfer circuit is connected as a circle. The first cell in the analysis is the cell in contact with the cooling channel inlet. Cell number in the θ-direction increases along the flowing direction of the cooling water. In the case of the z-direction, thermal circuit is connected as shown in Fig. 3.5(c). The rotor, the winding and the stator are connected to the motor case with a heat transfer circuit. The motor case is linked with the ambient air in the thermal circuit. After applying the thermal circuit as shown in Fig. 3.2 to all the cells inside the

Table 3.1 Geometric parameters and specification of analyzed motor

Parameter	Value
Number of pole	8
Number of slot	48
Permanent magnet	Nd-Fe-B
Maximum power [kW]	150
Outer diameter of stator [mm]	119
Length of stator [mm]	173
Air gap length [mm]	0.8

Table 3.2 Thermodynamic properties used for numerical analysis

Parameter	Value	Reference
Thermal conductivity of lamination in x and y direction [W/m-K]	16.3	[84]
Thermal conductivity of lamination in z direction [W/m-K]	0.2	[84]
Thermal conductivity of winding [W/m-K]	400	-
Thermal conductivity of magnet [W/m-K]	8	[85]
Thermal conductivity of case [W/m-K]	237	[84]
Insulation paper thermal conductivity [W/m-K]	0.25 (winding & stator)	[84]
Winding coating thermal conductivity [W/m-K]	0.31 (winding & air)	[84]
Bond thermal conductivity [W/m-K]	0.2 (magnet & rotor)	[84]
Contact thermal resistance of stator-case [$W^{-1}m^{-2}K$]	0.0011	[84]
Density of lamination [kg/m^3]	7860	-
Density of winding [kg/m^3]	8960	-
Density of magnet [kg/m^3]	7600	[85]
Density of case [kg/m^3]	2700	-

Table 3.2 Thermodynamic properties used for numerical analysis (continued)

Parameter	Value	Reference
Specific heat of lamination [J/kg-K]	449.4	-
Specific heat of winding [J/kg-K]	388.1	-
Specific heat of magnet [J/kg-K]	440	[85]
Specific heat of case [J/kg-K]	903	-

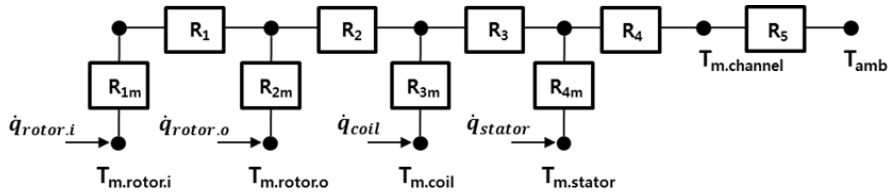

(a)

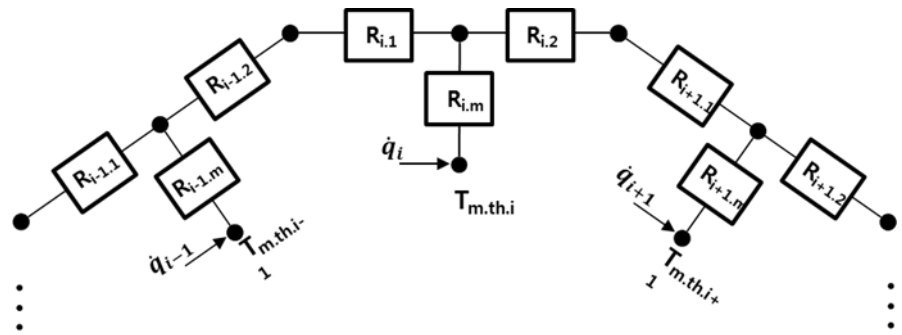

(b)

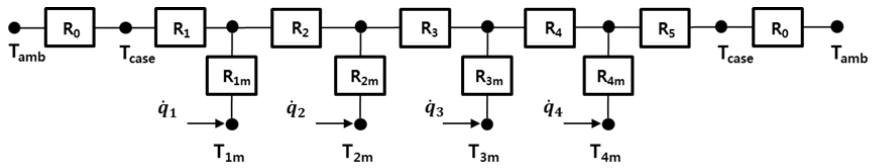

(c)

Fig. 3.5 Total thermal circuit of the motor model for (a) r-direction,

(b) θ-direction and (c) z-direction

motor, fully lumped parameter thermal model for the motor is developed to calculate the motor temperature variation as a function of the time.

3.3 Results and discussion

3.3.1 Model validation

The developed model is verified in comparison with the actual vehicle test. The surface temperature of the motor winding and the temperature of the cooling water outlet were measured in an actual vehicle experiment. Based on the experimental results, the results of the numerical analysis using fully lumped parameter thermal model were verified. Fig. 3.6 compares the results calculated using the motor model with the results measured from the actual vehicle experiment. The error and the relative time shown in the graphs are calculated as Eq. (3.45) and (3.46).

$$t_{re} = \frac{t}{t_{tot}} \tag{3.45}$$

$$err = \frac{T_{sim} - T_{exp}}{T_{exp}} \times 100(\%) \tag{3.46}$$

t_{tot} is the total driving time and t_{re} is relative time presented in the figure.

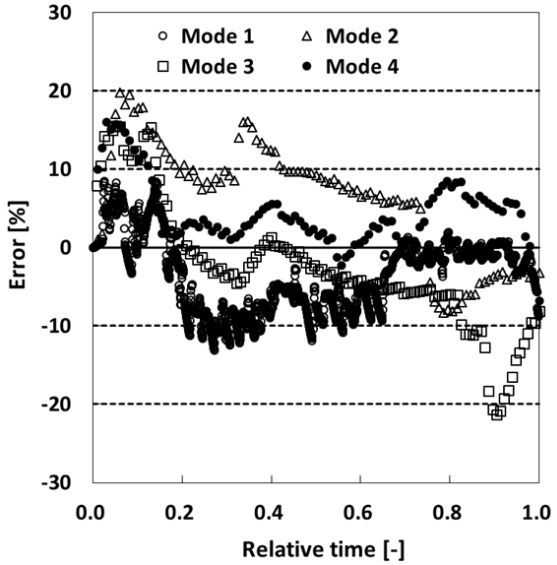

(a)

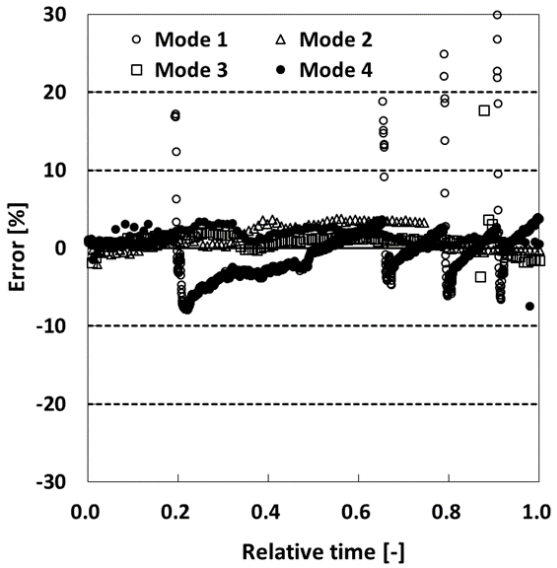

(b)

Fig. 3.6 Model validation results with experimental data (a) coil temperature and (b) coolant outlet temperature

T_{sim} is the temperature calculated by numerical simulation and T_{exp} is the measured temperature from the experiment. As shown in the figure, it is confirmed that the winding temperature and the coolant outlet temperature variation is similar to that of the experimental results for the four driving modes. As shown in Fig. 3.6(a), the largest error in winding temperature is -13.15% and the average error is 4.98% for the four driving modes. In the case of the coolant outlet temperature, as shown in Fig. 3.6(b), it is predicted in the most driving time. However, in the case of the driving mode 1, there is a time in which the error of the coolant outlet temperature becomes large. At the time which the mass flow rate of the water changes suddenly, the error of the coolant outlet temperature is increased. At this time, the model predicts the temperature to be high, because the thermal properties of the pipe after the outlet of the motor are not reflected. The model calculates only for the motor. However, in the actual experiment, the water coming out from the outlet of the motor channel moves toward the radiator through the pipe. The thermal capacity of the pipe after the motor channel is needed to predict the temperature change due to the instantaneous change of the coolant mass flow rate. Therefore, considering the motor alone, the prediction accuracy of the model is high. Moreover, larger error of the coolant outlet temperature occurs only in a time less than 10 seconds in which the mass flow rate suddenly changes. Thus,

overall, the motor coolant outlet temperature can be properly predicted. Average error of the water outlet temperature is 2.12%.

3.3.2 Temperature distribution inside the motor

The motor model is used to compare existing water cooling method and refrigerant cooling method. In the analysis, R134a is adopted as a cooling refrigerant. The criterion for comparing two methods is the power consumption of the pump. Efficient cooling means high cooling performance with low power consumption. Therefore, it is desirable to compare both methods using the power consumed by the pump for the motor cooling. Because pump efficiency is different based on the pump design, this study calculated the ideal power consumption calculated by the flow rate and the pressure difference of the channel. Fig. 3.7 shows the ideal power consumption of the pump as a function of flow rate. The filled marks are the results obtained through the experiments. Based on the experimental results, the relationship between flow rate and ideal pump power consumption is presented as a dotted line. Using R134a of 1.0 L/min, the ideal power consumption of the pump is 0.2 W. The water cooling needs the same power consumption of the pump when the flow rate is 4.1 L/min.

The cooling performance of R134a with 1.0 L/min and water with 4.1

L/min are presented in Fig. 3.8(a). The driving condition of the motor is a torque of 150 Nm and a rotational speed of 4000 rpm. The inlet temperatures of the refrigerant and the water are the same as 60°C. R134a enters to the motor cooling channel inlet as saturated liquid of 60°C. The ambient temperature is 35°C and the initial temperature of the motor is 60°C. As shown in the figure, when the same pump power is consumed, R134a can reduce the maximum temperature of the motor winding to 4.6°C. When 30 minutes passed, R134a cooling showed the maximum temperature of the motor winding as 85.8°C, and water cooling showed 90.4°C, respectively. As the heat loss of the motor increases, the maximum temperature difference of the motor will further increase. In order to show the same cooling performance as R134a with 1 L/min by water cooling, 12.2 L/min is required as shown in Fig. 3.8(a) and the pump power consumption of 2.3 W is consumed as shown in Fig. 3.7. Therefore, R134a cooling can reduce the power consumption of the pump by 92.0%.

However, maintaining proper flow rate of the refrigerant is important. As shown in Fig. 3.8(b), when the flow rate of the R134a is low, the temperature of the winding rises rapidly. The dashed line in Fig. 3.8(b) is the temperature change of the winding when 0.5 L/min of R134a flows. Not only is the maximum temperature of the winding rapidly rising, but also the temperature

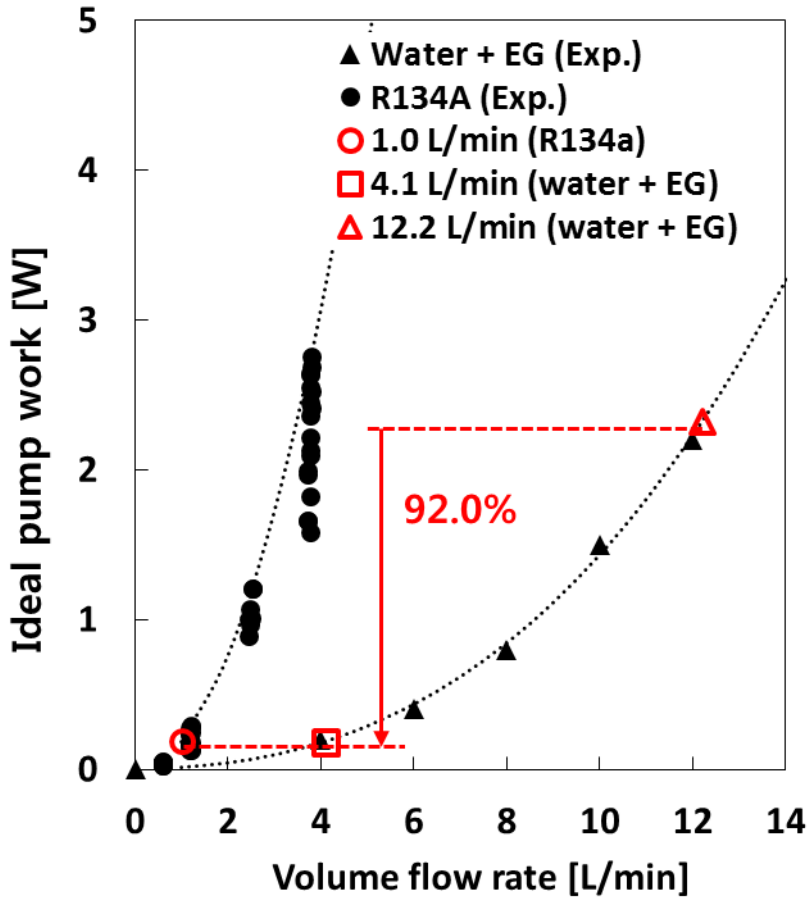

Fig. 3.7 Ideal pump power consumption with respect to volume flow rate

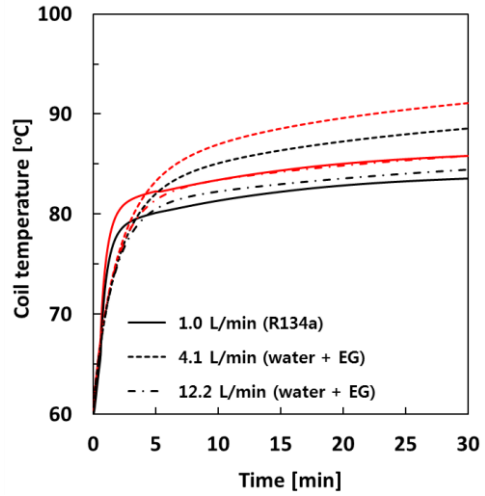

(a)

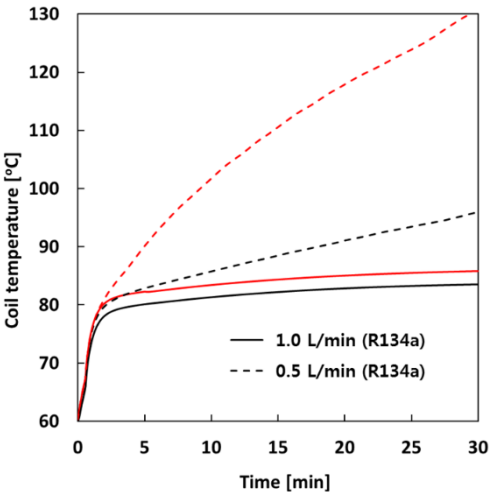

(b)

Fig. 3.8 Coil temperature variation with time (a) comparison with water and R134a and (b) effect of flow rate for R134a

difference between the windings is high. The reason is that all the refrigerant in the channel is vaporized due to the small flow rate if considering motor heat loss. Therefore, near the inlet, R134a is in a two-phase state, but it is vaporized completely while going to the outlet. Therefore, the heat transfer performance is degraded rapidly and the motor cooling failed. When the flow rate is 0.5 L/min, after 30 minutes, the maximum temperature of the motor winding is 130.7°C. Therefore, refrigerant cooling requires an appropriate flow rate in consideration of the amount of heat loss of the motor.

Fig. 3.9 is a temperature distribution of the winding according to the position. The winding in the model is divided into 48 cells in the theta-direction and 4 cells in the z-direction. In the Fig. 3.9(a), when the theta = 0 and z = 1, the cell is near the fluid channel inlet. Fig. 3.9(a) shows the temperature distribution after 30 minutes when water cooling is applied. As shown in the figure, the minimum temperature is displayed when the theta is small. However, since heat conduction in the theta direction is considered in the model, the theta of the minimum temperature position isn't zero. The minimum temperature is observed when the $\theta = 45.0^{\circ}$ and z = 1 of 88.5°C. While, the position of the maximum temperature is $\theta = 307.5^{\circ}$ and z = 3. The maximum winding temperature is 91.1°C.

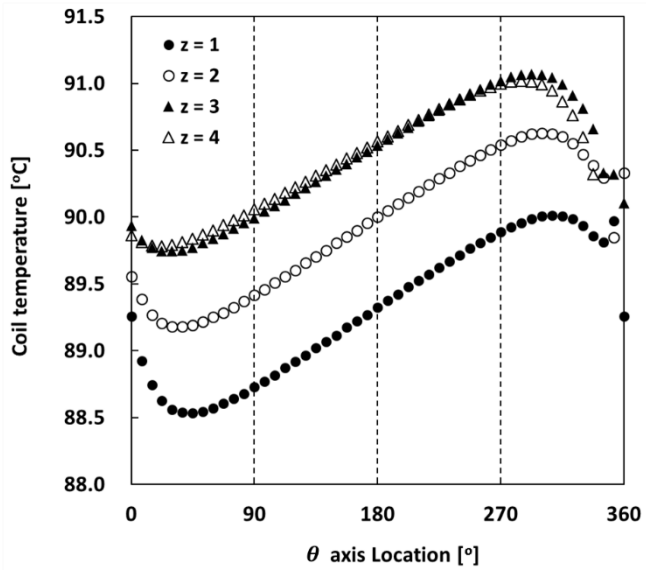

(a)

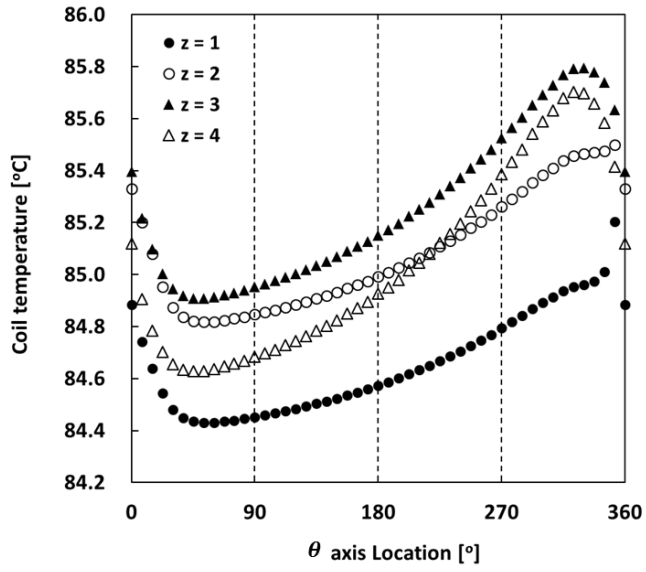

(b)

Fig. 3.9 Coil temperature distribution at 30 minute of (a) water cooling (1.0 L/min) and (b) R134a cooling (1.0 L/min)

When R134a cooling is applied, the temperature distribution has similar tendency as shown in Fig. 3.9(b). The maximum temperature is indicated when z = 3 and the θ = 330˚. The minimum temperature is indicated when z = 1 and the θ = 52.5˚. However, the temperature values are significantly different. In R134a cooling, the maximum temperature is 85.8ºC, and the minimum temperature is 84.4ºC. Also, the temperature difference between the windings is different. The maximum temperature difference between the windings is 2.5ºC for the water cooling. On the other hand, the maximum temperature difference is 1.4ºC with R134a cooling. Because the motor windings are electrically connected, the greater the temperature difference between the windings, the greater the risk of motor failure [86]. R134a cooling allows the temperature of the windings to be kept generally low and uniform, reducing the risk of motor failure.

Fig. 3.10 shows the results when the R134a flow rate is 0.5 L/min. As shown in Fig. 3.10(a), when one minute has elapsed after driving, the temperature of the motor winding is relatively low. At this time, the maximum winding temperature is 75.3ºC. However, after 10 minutes have passed, the winding temperature rises significantly from all locations (Fig. 3.10(b)). The maximum temperature increases to 101.7ºC. Also, the maximum temperature

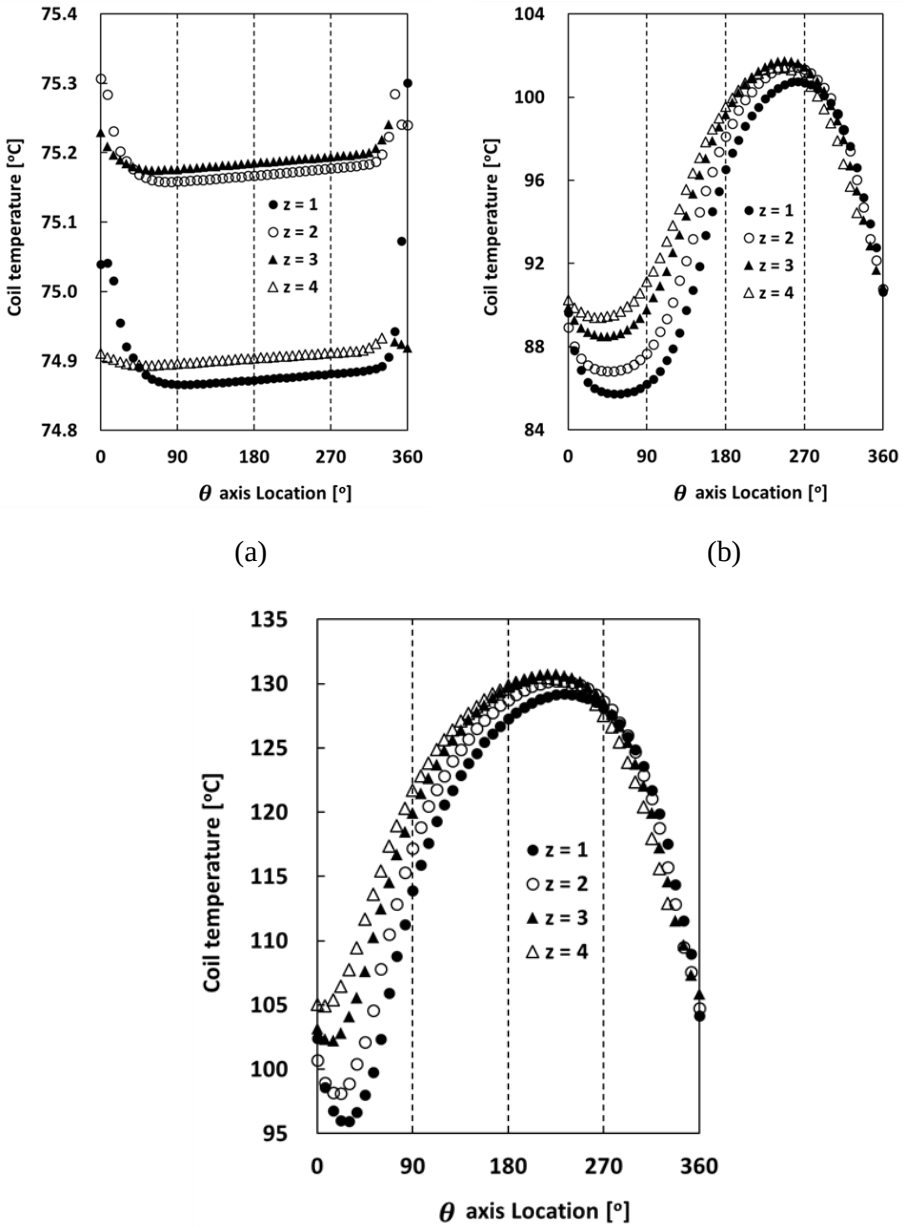

Fig. 3.10 Coil temperature distribution of R134a cooling (0.5 L/min) at (a) 1 minute (b) 10 minute and (c) 30 minute

difference between the windings is 16.0°C. Due to the low flow rate, the refrigerant is completely vaporized. The temperature of the outlet after 10 minutes is 16.4°C higher than saturation temperature. After 30 minutes, the maximum temperature of the winding reaches 130.7°C, and the maximum temperature difference reaches 34.8°C (Fig. 3.10(c)). The outlet at this time is in a gaseous state where the temperature is 37.6°C higher than saturation temperature. In order to maintain winding temperature lower, flow rate of the refrigerant should be controlled considering the heat loss of the motor.

3.3.3 Cooling performance comparison

Based on the results of 30 minutes passed, the cooling performances of the water and the R134a were compared. As shown in Fig. 3.11, the winding temperature after 30 minutes according to the inlet temperature and flow rate of the water and R134a are presented. The temperature of the winding with water cooling decreases as the flow rate increases. On the other hand, the temperature of the winding is almost constant regardless of the flow rate of the R134a except for when the flow rate is 0.5 L/min because the boiling temperature of the R134a

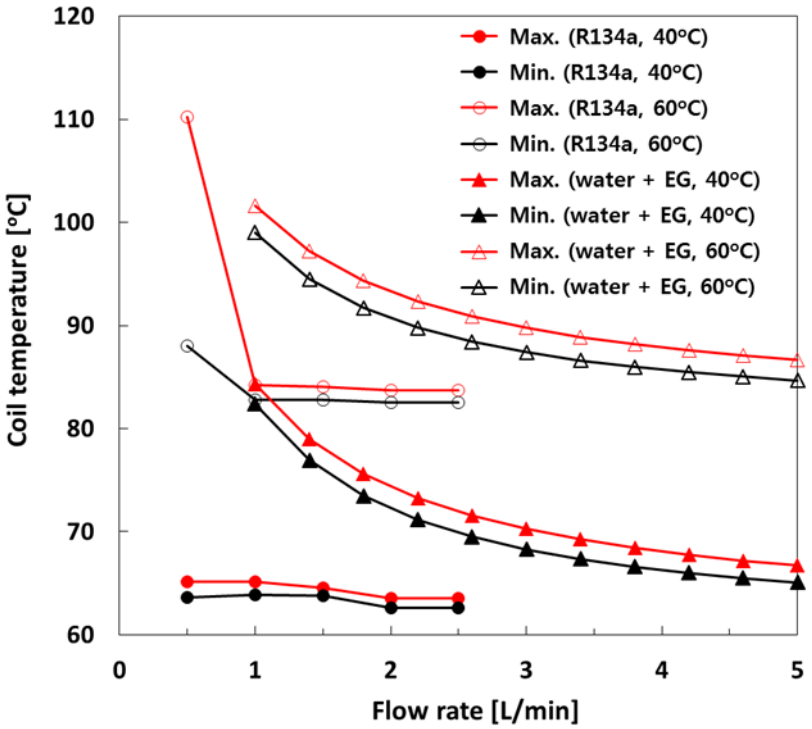

Fig. 3.11 Winding temperature results with respect to flow rate

is the same regardless of the flow rate. However, the flow rate is 0.5 L/min, the temperature of the winding is high. In the 0.5 L/min case, all of the refrigerant near the channel outlet is vaporized. However, when the inlet temperature of the refrigerant is 40°C, the R134a is not completely vaporized. There are two causes, one of which is that when the temperature of the motor is low, the motor heat loss is also reduced. Another reason is that the latent heat required for vaporization differs depending on the refrigerant saturation temperature. The latent heat of vaporization is 163.02 kJ/kg when the saturation temperature is 40°C. On the other hand, the latent heat of vaporization is 139.12 kJ/kg when the saturation temperature is 60°C. Therefore, although the same flow rate flows, the outlet refrigerant is not completely vaporized when the saturation temperature is 40°C.

As mentioned in Chapter 1 and 2, joule loss is highly dependent on the temperature of the winding. Therefore, when the flow rate and the inlet temperature change, the variation of the joule loss from the motor tends to be as shown in Fig. 3.12. The tendency of the temperature of the winding and the joule loss is similar. Also, based on the same flow rate, the joule loss of the R134a cooling has a difference of up to 90.1 W when compared with the joule loss of the water cooling. It can increase the efficiency of the motor and improve the mileage of the vehicle. However, in the

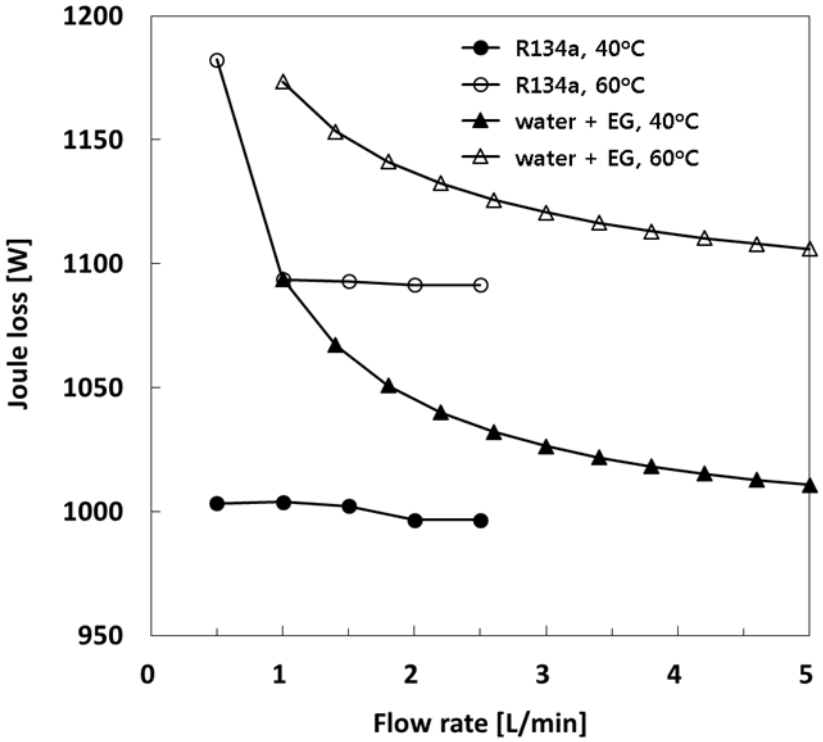

Fig. 3.12 Joule loss results with respect to flow rate

case of R134a cooling, when all the refrigerant are vaporized, not only the temperature of the motor rises but also the joule loss of the motor increases as shown in Fig. 3.12 of the refrigerant flow rate as 0.5 L/min. In some cases, joule loss increases significantly. This is the effect of the winding temperature rise. Thus, R134a cooling can be accomplished to cool the motor windings as well as thereby improve the motor efficiency by reducing joule losses.

Through efficient cooling, motor losses can be reduced and efficiency can be improved as well as increase motor power output. Since the temperature of the motor winding has a limitation, if the power output of the motor is excessively large, cooling may not be properly performed, causing a failure. Therefore, if the motor winding temperature can be lowered with the same pump power consumption, the temperature of the motor can be maintained under the limit temperature even if the power output of the motor is improved. Table 3.3 shows the relationship between the motor power output and the cooling method. Case 1 shows the conventional water cooling with maximum flow rate of 25.0 L/min, and shows the maximum temperature of the motor winding after 2 hours. Using R134a cooling with the same pump power, the maximum temperature of the motor winding can be lowered to 175.6^{o}C. Therefore, even if the motor power output increases and the heat generation of the motor increases, the motor can be cooled. As in case 3, when the motor

power output increases to 159.0 kW, the maximum winding temperature can be maintained as the same in case 1 through R134a cooling. Therefore, if R134a cooling is applied, motor cooling is sufficiently conducted even though the motor power output increases by 6.0%.

3.3.4 Dynamic cooling performance

The results presented in above section are obtained when the motor driving condition is constant. However, in an actual vehicle, operating conditions according to time change continuously. For evaluating an actual motor cooling performance, the result when the motor performs acceleration and deceleration continuously is important. Therefore, the cooling performance is evaluated for the driving schedule as shown in Fig. 3.13(a). The driving schedule of Fig. 3.13 (a) is a combined cycle of the UDDS (Urban Dynamometer Driving Schedule) and HWY (High-Way) driving modes. The UDDS mode is used to evaluate the performance of the vehicle as well as the vehicle's driving cycle in the actual city driving. The HWY mode is the driving cycle of the vehicle on the highway.

Fig. 3.13(b) is the maximum temperature of the motor winding calculated during driving schedule of Fig. 3.13(a). The inlet temperature of the water and the R134a is the same as 40^{o}C, and the ambient temperature is 35^{o}C. The

Table 3.3 Cooling performance comparison by cooling method and volume flow rate

Parameter	Case 1	Case 2	Case 3
Motor power output [kW]	150.0	150.0	159.0
Cooling method/ Volume flow rate [L/min]	Water + EG/ 25.0	R134a/ 8.7	R134a/ 8.7
Maximum coil temperature [^{o}C]	181.9	175.6	181.9
Ideal pump power consumption [W]	14.46	14.46	14.46

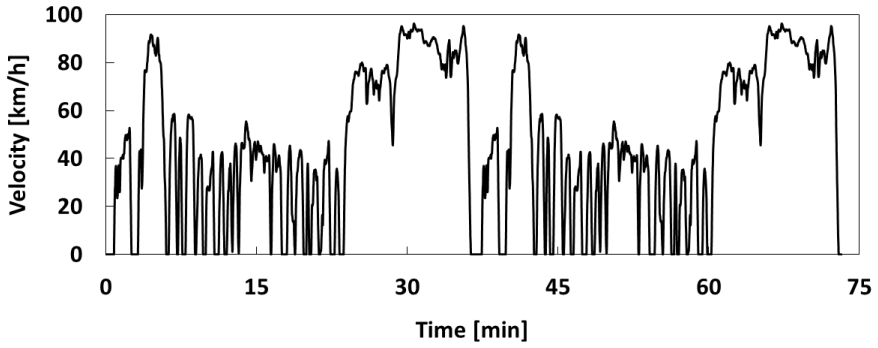

(a)

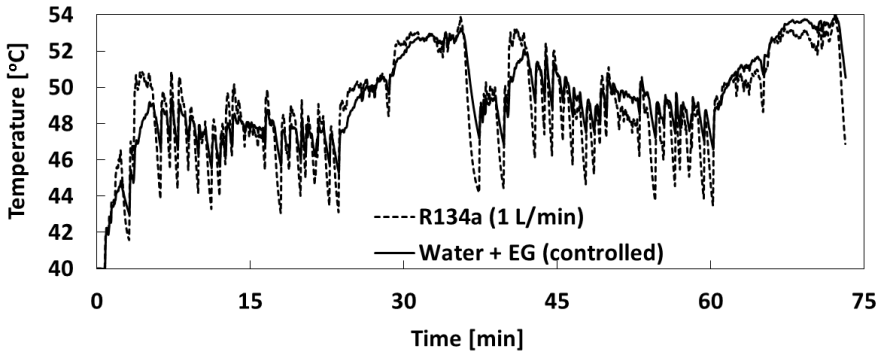

(b)

Fig. 3.13 Dynamic driving results

(a) Velocity profile of driving and (b) Winding temperature variation during the driving with different cooling method and flow rate

volume flow rate of R134a is fixed as 1.0 L/min because this value is enough to cool the motor. The volume flow rate of the water is controlled to minimize pump power consumption. As shown in the Fig. 3.13(b), with R134a cooling and water cooling, the maximum temperature of the motor winding is 54.0^{o}C. Further, in the case of R134a cooling, since the heat transfer coefficient is large, the winding temperature decreases fast when the heat generation of the motor decreases. As shown in the figure, similar cooling performance is obtained by using two cooling methods. However, as described above, when comparing the cooling performance, not only the motor winding temperature but also the power or energy consumption of the pump should be considered. The R134a cooling consumes 0.81 J for a pump. On the other hand, water cooling requires 4.08 J for driving a pump. Therefore, applying the R134a cooling can reduce the power consumption of the pump by 80.1% while achieving the same cooling performance.

3.6 Summary

Fully lumped parameter thermal model for the motor has been developed to accurately predict the temperature inside the motor and the heat loss of the motor. Using the motor model, cooling performances of the motor with both existing water cooling and the refrigerant cooling by R134a are compared.

Especially, the winding temperature is the main target of the motor thermal management.

When driving under the same conditions, refrigerant cooling can maintain the maximum winding temperature 4.6ºC lower than water cooling with the same pump power consumption. When the flow rate of the water increased to 12.2 L/min to maintain the maximum winding temperature as the same of R134a cooling, the pump power consumption should be increased as 12.5 times. Such tendency appears in dynamic driving condition. R134a cooling is able to reduce pump power consumption of 80.1% with the same cooling performance when driving UDDS and HWY driving schedule twice in a row.

However, for the refrigerant cooling, controlling the flow rate with considering the heat loss of the motor is significant. If the flow rate of the refrigerant is small for the given motor heat loss, the refrigerant is completely vaporized inside the cooling channel. If it is single phase as gas state, the heat transfer coefficient is so small that it loses the benefits of flow boiling cooling. With gas refrigerant, the cooling performance is worse than that of the water. Therefore, the flow rate should be controlled so that the refrigerant is not completely vaporized and the two-phase condition of the refrigerant can be maintained.

Chapter 4. Parametric study on the integrated system with liquid pump and vapor compressor for electric vehicle

4.1 Introduction

Electric vehicles, unlike conventional internal combustion engine vehicles, perform indoor cooling, heating and component thermal management using electric energy from the battery. Therefore, a new system needs to be designed in order for the refrigerant cooling proposed in Chapter 3 to be practically applied to the existing electric vehicle system. Moreover, for optimal operation of the new system, parametric study for the system is necessary.

In this chapter, comparison of two systems in order to apply the motor cooling with refrigerant to the electric vehicle system is conducted. The basic system is considered as an electric vehicle with heat pump system. Based on the basic system, the first system uses the motor cooling channel as an evaporator. The concept of the first system is adopted from the existing battery cooling. In the second system, liquid refrigerant is drawn from the condenser outlet by liquid pump and passes through the motor channel.

A performance comparison of the two systems is investigated for the

cooling performance of the motor and the energy efficiency of the vehicle. As mentioned in chapter 3, winding temperature is of primary interest, as it is most important for evaluating the cooling performance of the motor cooling method. Furthermore, the energy consumption of the entire vehicle system is considered to compare the two systems to improve the mileage of the electric vehicle. The comparison results are calculated for the summer season and the winter season respectively.

4.2 Integrated heat pump system proposal

4.2.1 Basic heat pump system for electric vehicle

The basic heat pump system for an electric vehicle is presented as in Fig. 4.1. The solid line indicates the refrigerant line, and the dashed line indicates the water line. The heat pump is operated for indoor (cabin) heating and cooling. In addition, the water cycle is designed to cool the main components such as battery and motor. As shown in Fig. 4.1(a), the heat pump in summer uses the indoor heat exchanger as an evaporator. The refrigerant is evaporated in the heat exchanger and the indoor air is cooled. The pressure of the refrigerant that passes through the evaporator becomes higher through the

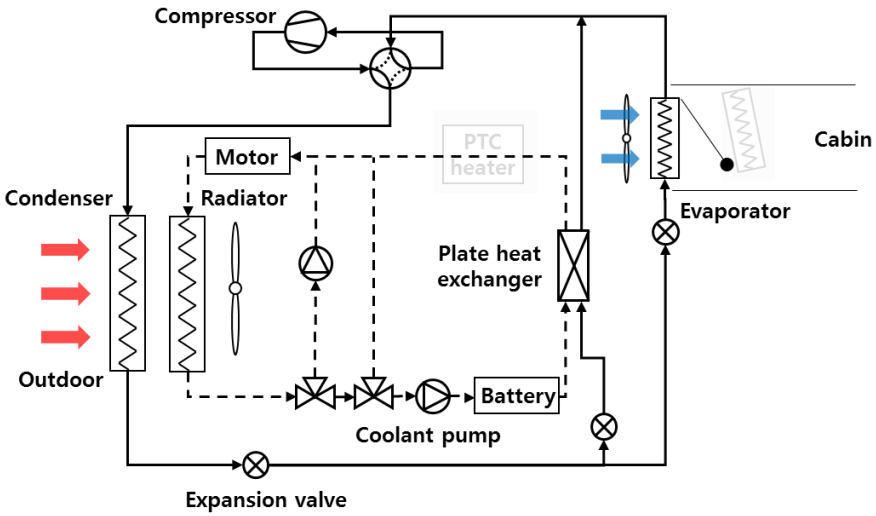

(a)

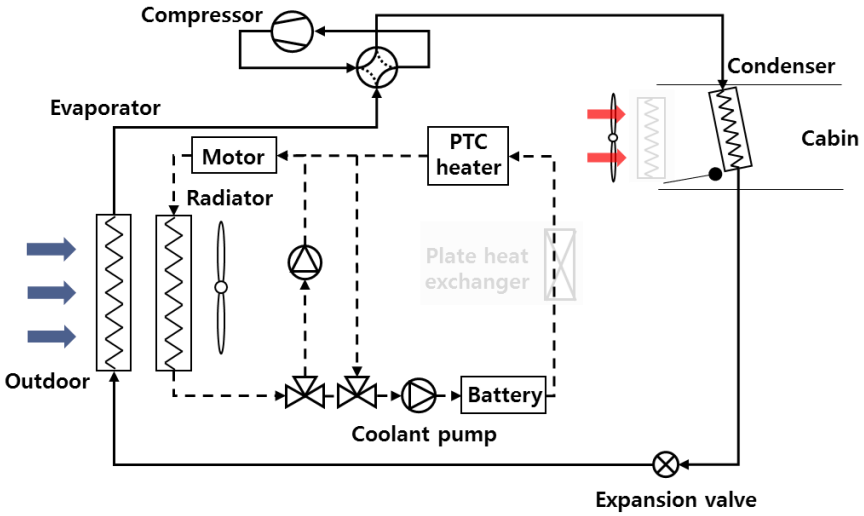

(b)

Fig. 4.1 Basic heat pump system and coolant system for electric vehicle in (a) summer and (b) winter

compressor, and releases the heat from the condenser to the outside air. The battery is cooled by the water. However, if the outdoor air temperature is high in summer, the ambient air temperature is higher than the proper battery operating temperature (20^{o}C ~ 35^{o}C). In this condition, battery cooling would be failed. In this case, the low-pressure side refrigerant and the water exchange heat inside the plate heat exchanger shown in the figure. The plate heat exchanger and the indoor heat exchanger are all used as evaporator, and the two are connected in parallel.

In winter season, the direction of heat transfer through the heat pump changes as presented in Fig. 4.1(b). An outdoor heat exchanger is used as an evaporator and an indoor heat exchanger is used as a condenser. In fact, two heat exchangers are installed indoor to dehumidify the room. In addition to the indoor heat exchanger used as an evaporator in the summer, another heat exchanger is installed. This heat exchanger is only used as a condenser in the winter. The reason for installing two heat exchangers in the cabin side is dehumidification for the cabin in winter. In order to operate dehumidification mode, both an evaporator and a condenser are needed. When the winter dehumidifying mode is operated, the air supplied into the cabin passes through the indoor evaporator and the temperature drops. The reduction of the air temperature condenses and removes the water vapor in the air. The

dehumidified air passes through the indoor condenser and the temperature rises again to heat up the cabin. The temperature of the battery in winter is heated by the coolant warmed using a PTC heater. The heater isn't operated if battery cooling is required. Because the PTC heater converts electric energy directly into heat, it consumes a large portion of the energy in the battery [7].

4.2.2 Parallel Cooling Vapor Compression (PCVC) system

In the basic system of Fig. 4.1, the motor is cooled by water regardless of the season. However, with the refrigerant cooling proposed in Chapter 3, the system is modified as shown in Fig. 4.2. Fig. 4.2 is schematics of a system applying parallel cooling for motor cooling. Battery cooling is beyond the scope of this study, so use the existing system as it is.

The system can be called as Parallel Cooling Vapor Compression (PCVC) system. PCVC system for the motor cooling in the summer can be achieved applying the concept used in conventional battery chiller or plate heat exchanger as shown in the Fig. 4.2(a). As the temperature on the low pressure side is low in the heat pump, part of the refrigerant leaving the expansion valve is sent to the motor cooling channel. Since the motor cooling is performed with a low temperature refrigerant, the temperature of the motor can be significantly

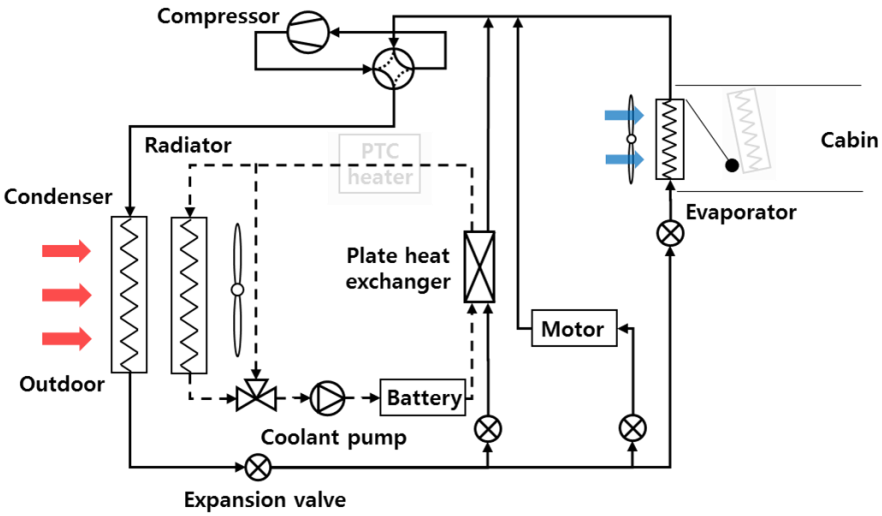

(a)

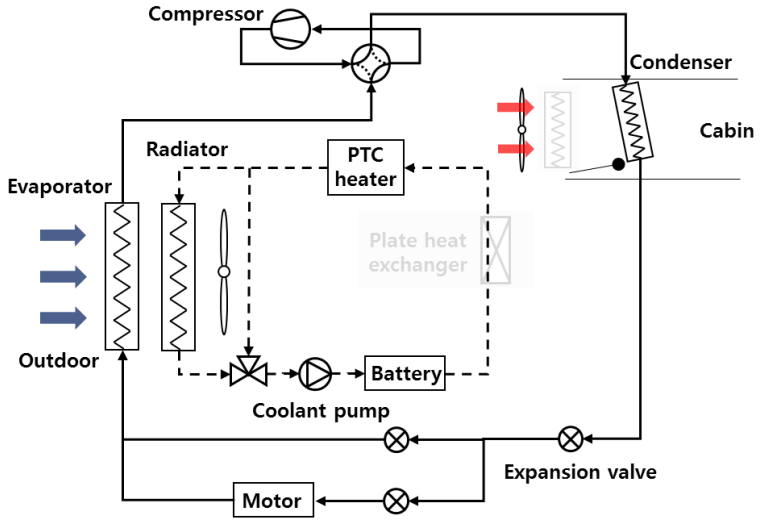

(b)

Fig. 4.2 Schematics of parallel cooling system in (a) summer and (b) winter

decreased. As a result, the heat loss of the motor can be greatly reduced. However, when the outdoor temperature in summer is high, the power consumption of the compressor can be increased because the compressor has to send the refrigerant not only to the indoor evaporator but also to the battery chiller and the motor cooling channel. Therefore, the energy efficiency of the vehicle system can be degraded.

In winter, PCVC system is designed as presented in Fig. 4.2(b). Because outdoor heat exchanger is used as an evaporator in winter, the motor cooling channel is connected in parallel with the outdoor unit. As in summer, the motor temperature can be maintained as low, but compressor power consumption may increase. On the other hand, in winter, heat generated by the motor can be used for cabin heating. Therefore, the coefficient of performance (COP) of the PCVC system in winter would be improved over existing heat pump system.

4.2.3 Integrated system with Liquid Pump and Vapor Compressor (LPVC)

Unlike the PCVC system, refrigerant for motor cooling can be adopted from the condenser. The condenser side refrigerant is in a high temperature and high pressure state. However, since the motor has a limit temperature of 150^{o}C, it can be sufficiently cooled with refrigerant of 50^{o}C which is the temperature

of the condenser refrigerant in summer. Since the refrigerant at the outlet of the condenser is usually in a liquid state, the liquid refrigerant can be sent to the motor cooling channel by adding a reservoir and a pump in the latter stage of the condenser. The two-phase or vapor state refrigerant from the motor channel is mixed with the compressor discharge refrigerant at the inlet of the condenser and sent to the condenser again. Therefore, the integrated system with both liquid pump and vapor compressor (LPVC) is proposed.

Fig. 4.3 is schematic diagrams of the LPVC system according to the season. As shown in Fig. 4.3(a), since the outdoor unit is a condenser in summer, a reservoir is attached to the outlet of the outdoor unit, and the reservoir outlet is connected to both the expansion valve side and the pump side, respectively. The pump sends the liquid refrigerant to the motor cooling channel. The expansion valve adjusts its opening, and sends the refrigerant through the indoor unit and the battery chiller. Compared to the PCVC system, the temperature of the motor could be higher. However, power consumption of the vehicle can be reduced because power consumption of the liquid pump is smaller than that of the vapor compressor.

As shown in Fig. 4.3(b), an indoor unit is used as a condenser in winter. Therefore, a reservoir and a pump are required at the outlet of the indoor condenser. As in summer, the temperature of the motor by LPVC system can

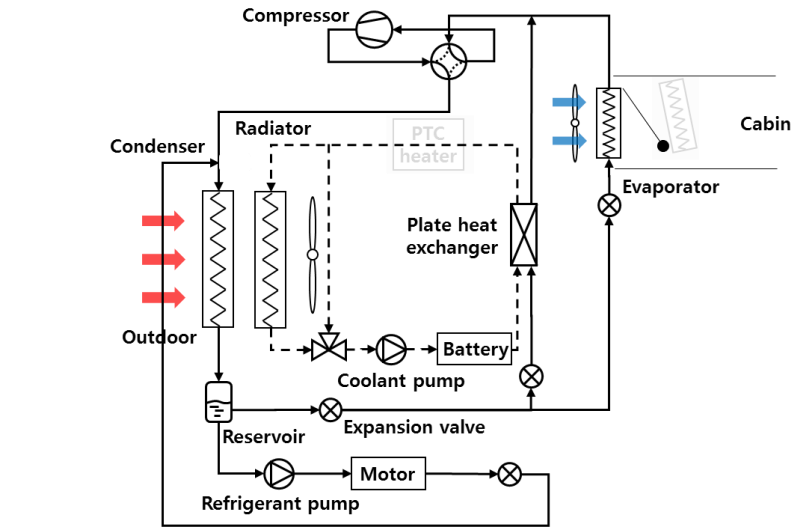

(a)

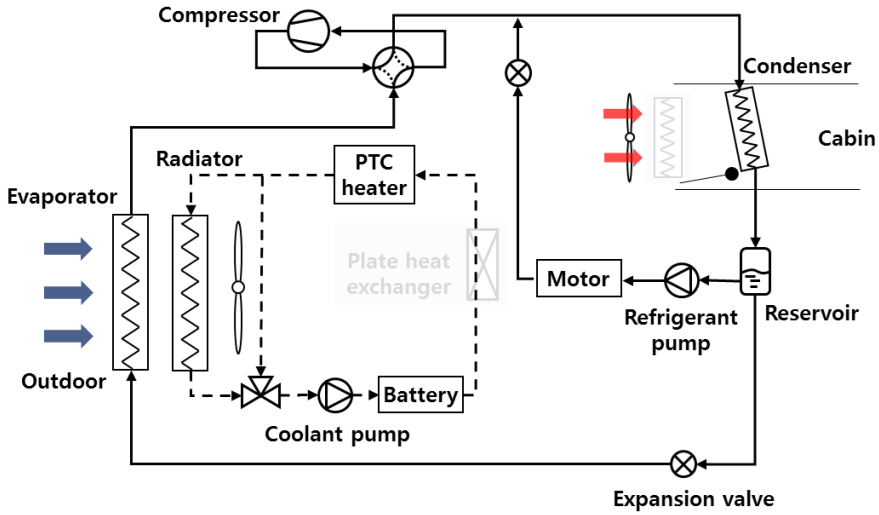

(b)

Fig. 4.3 Schematics of integrated system with both liquid pump and vapor compressor (LPVC) in (a) summer and (b) winter

be higher compared to PCVC system. However, there are advantages in terms of power consumption. Also, COP of the vehicle system with LPVC system will be improved over the basic heat pump system, as motor waste heat can be used for indoor heating in winter.

4.3 Modeling

4.3.1 Compressor and expansion valve

Each components is modeled for steady state performance analysis. First of all, scroll type compressor is adopted for compressor of the systems. Because scroll type compressor is classified as volume displacement compressors, it is modelled as typical method of volume displacement compressor. The pressure and temperature at the inlet and outlet of the compressor is assumed for calculation. From the assumption, compressor outlet temperature, mass flow rate of the refrigerant and compressor power consumption are obtained. Considering polytropic compression through the compressor, compressor outlet temperature is calculated from Eq. (4.1).

$$T_{comp,o} = T_{comp,i}(P_{comp,i}/P_{comp,o})^{\frac{1-n}{n}} \quad (4.1)$$

n is the polytropic coefficient obtained empirically. In actual volume displacement compressor, a little portion of refrigerant is remained inside compressor and re-expansion occurs. Thus, mass flow rate is reduced compared to theoretical compressor. The decrease of the mass flow rate is defined as volumetric efficiency as Eq. (4.2).

$$\eta_V = 1 - C\left(\frac{\rho_{comp,out}}{\rho_{comp,in}} - 1\right) \tag{4.2}$$

C is the clearance volume ratio calculated empirically. The mass flow rate of the compressor is obtained by Eq. (4.3).

$$\dot{m}_{comp} = \eta_V \rho_{comp,in} V_{disp} \omega_{comp} \tag{4.3}$$

ω_{comp} is rotational speed of the compressor and V_{disp} is the volume of compressor displacement. Compressor power consumption is calculated as Eq. (4.4).

$$W_{comp} = \dot{m}_{comp}(i_{comp,out} - i_{comp,in}) \tag{4.4}$$

For expansion valve, isenthalpic expansion is assumed. The enthalpy of inlet and outlet of the expansion valve is the same as Eq. (4.5).

$$i_{EEV,o} = i_{EEV,i} \tag{4.5}$$

4.3.2 Condenser and evaporator

In heat pump analysis, heat exchanger is important component. Louvered fin type heat exchanger is used in conventional heat pump system for electric vehicle. Based on the finite volume method, heat transfer rate is calculated for each discretized cell.

Based on the given refrigerant pressure and inlet temperature of each cell, heat transfer coefficient of refrigerant side in each cell is obtained. In condensation of the refrigerant, heat transfer coefficient is calculated by Eq. (4.6) [87].

$$Nu_{ref} = 0.018\left(\frac{\mu_v}{\mu_l}\right)^{0.078}\left(\frac{\rho_l}{\rho_v}\right)^{0.39} Re_l^{0.20}(Re_{lo} - Re_l)^{0.70} Pr_l^{0.65} \tag{4.6}$$

Heat transfer coefficient in evaporators is obtained by Eq. (4.7) ~ (4.9) [88].

$$h_{ref} = E h_l \tag{4.7}$$

$$\mathrm{E} = 1 + 3000Bo^{0.86} + 1.12\left(\frac{x}{1-x}\right)^{0.75}\left(\frac{\rho_l}{\rho_v}\right)^{0.41} \tag{4.8}$$

$$Bo = \frac{q''}{i_{lv}G} \tag{4.9}$$

Air side heat transfer coefficient is calculated by Eq. (4.10) ~ (4.11) [89].

$$j = \frac{h_{air}}{\rho_{air}V_{max}C_{p,air}}Pr_{air}^{2/3} \tag{4.10}$$

$$j = \mathrm{Re}_{air}^{-0.49}\left(\frac{\theta_l}{90}\right)^{0.27}\left(\frac{F_p}{L_p}\right)^{-0.14}\left(\frac{F_l}{L_p}\right)^{-0.29}\left(\frac{T_d}{L_p}\right)^{-0.23} \times \left(\frac{L_l}{L_p}\right)^{0.68}\left(\frac{T_p}{L_p}\right)^{-0.28}\left(\frac{\delta_f}{L_p}\right)^{-0.05} \tag{4.11}$$

In order to calculated fan power consumption, pressure drop of air through heat exchangers is defined as Eq. (4.12) ~ (4.13) [90].

$$f_{air} = 0.54486\mathrm{Re}_{air}^{-0.3068}\left(\frac{\theta_l}{90}\right)^{0.444}\left(\frac{F_p}{L_p}\right)^{-0.9925}\left(\frac{F_l}{L_p}\right)^{0.5458} \times \left(\frac{L_l}{L_p}\right)^{-0.2003}\left(\frac{L_d}{L_p}\right)^{0.0688} \tag{4.12}$$

$$\Delta P_{air} = \frac{1}{2}\rho_{air}V_{air}^2\left(f_{air}\frac{A_{tot}}{A_{frt}\sigma_A} + 0.6\right) \tag{4.13}$$

f_{air} is the friction factor. A_{frt} is frontal area of the heat exchanger and A_{tot} is the sum of finned area and tube area.

4.3.3 Plate heat exchanger

In order to consider battery cooling in summer, plate heat exchanger is adopted. Due to the high temperature of the air in summer, optimum battery temperature near 30°C can't be maintained by air cooled radiator. In this condition, water after cooling battery passes plate heat exchanger to be cooled by the refrigerant from the outlet of the expansion valve. This plate heat exchanger is called as battery chiller. Inside battery chiller, heat transfer coefficient of refrigerant side is obtained by Eq. (4.14) [91].

$$Nu_{ref} = 1.926 Pr_l^{1/3} Bo^{0.3} Re^{0.5} \left[(1-x) + x \left(\frac{\rho_l}{\rho_v} \right)^{0.5} \right] \quad (4.14)$$

Coolant side heat transfer coefficient is calculated by Eq. (4.15) [92].

$$Nu_{wt} = 0.46 Re_{wt}^{0.66} Pr_{wt}^{0.333} \quad (4.15)$$

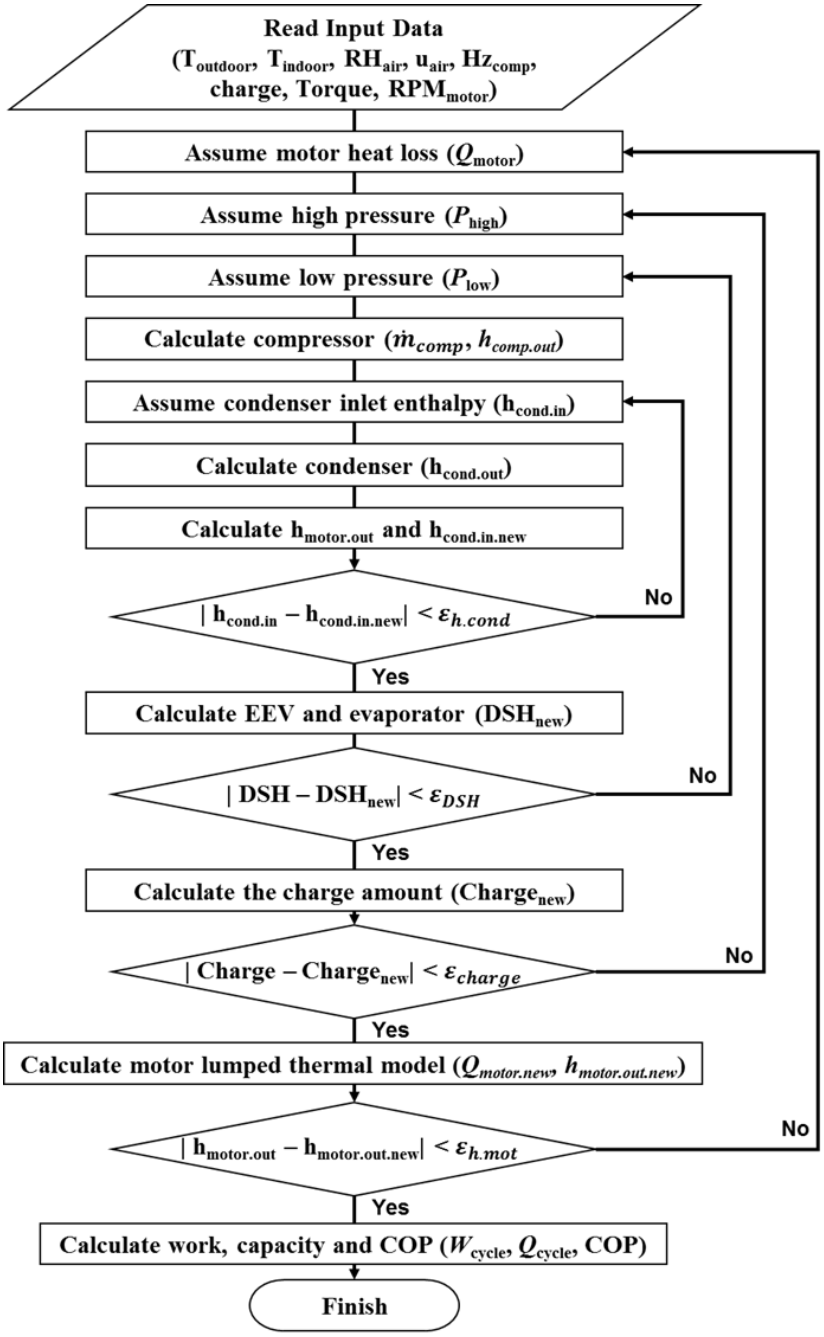

Fig. 4.4 Flow chart of the system analysis for LPVC system

4.3.4 Cycle modeling

Steady state cycle performance analysis is performed based on the component modeling described above sections. Fig. 4.4 is a flow chart for performance analysis of the LPVC system. The basic heat pump cycle and the PCVC system are basically the same in analysis. LPVC system analysis method also has common parts.

Outdoor temperature, cabin temperature and relative humidity are required for system analysis. Also, the torque and the rotational speed of the motor (ω_{mot}) are the input conditions. Control variables during system operation are compressor rotational speed (ω_{comp}), flow rate of the liquid refrigerant by pump ($\dot{m}_{pump}$), refrigerant charge in the system (m_{sys}), and the air velocity (u_{air}).

Motor heat loss ($\dot{Q}_{mot}$) is assumed based on the given motor driving conditions. High pressure (P_{high}) and low pressure (P_{low}) of the system is also assumed in order. By this, the compressor is calculated, and the mass flow rate ($\dot{m}_{comp}$) and the outlet enthalpy ($i_{comp,o}$) of the compressor are calculated. After that, the condenser inlet enthalpy ($i_{cond,i}$) is assumed. The condenser is calculated using the assumed enthalpy and the calculated mass flow rate to obtain the outlet enthalpy of the condenser ($i_{cond,o}$). The outlet enthalpy of the condenser is the same as the motor inlet enthalpy ($i_{mot,i}$) in the LPVC system

when the refrigerant from the condenser is subcooled state. Therefore, the motor outlet enthalpy is calculated by the motor inlet enthalpy and the assumed heat loss of the motor. Condenser inlet enthalpy is calculated as Eq. (4.4) via the calculated motor outlet enthalpy and compressor outlet enthalpy. Iterations are performed in comparison between the assumed condenser inlet enthalpy and calculated condenser inlet enthalpy.

Subsequently, the expansion valve and the evaporators are calculated. Depending on the operating conditions, the system needs many evaporators. For a basic heat pump cycle, one evaporator is needed. When the ambient temperature is high in summer, a battery chiller is used as an additional evaporator. In the same manner, the motor cooling channel is utilized as an evaporator in a parallel cooling system. Therefore, when multiple evaporators are used, the mass flow rate of each evaporator is determined by its load. From the calculation of the multiple evaporators, degree of superheat (DSH) of compressor inlet is obtained. The second iteration is conducted for low pressure of the system comparing between assumed DSH and calculated DSH. The third iteration is performed for obtaining high pressure of the system. The high pressure is calculated based on the charge amount of the system.

After the system pressure and temperature are calculated, fully lumped parameter thermal model of the motor developed in Chapter 3 is calculated.

Steady state motor temperature and heat loss of the motor is calculated by the model with motor inlet enthalpy, pressure, and mass flow rate of the refrigerant obtained from the system calculation. A fourth iteration is performed by comparing calculated enthalpy of motor channel outlet of the refrigerant from the model with the assumed enthalpy of the motor outlet.

After all the calculations are conducted, the temperature and pressure of the refrigerant and the temperature and loss of the motor can be calculated in the system. The power consumption of the system, the heating and cooling capacity, and the system COP are calculated. The power consumption of the entire system is calculated as Eq. (4.16).

$$\dot{W}_{sys} = \dot{W}_{comp} + \dot{W}_{fan} + \dot{W}_{pump} + \dot{Q}_{mot} \tag{4.16}$$

$\dot{W}_{sys}$ is the system power consumption and $\dot{W}_{comp}$ is the compressor power consumption. $\dot{W}_{fan}$ is the power consumption of the fan connected with indoor and outdoor unit. $\dot{W}_{pump}$ is the power consumption of the liquid pump to cool the motor. $\dot{W}_{fan}$ and $\dot{W}_{pump}$ is calculated as Eq. (4.17) and (4.18).

$$\dot{W}_{fan} = \Delta P_{air} \dot{V}_{air} \tag{4.17}$$

$$\dot{W}_{pump} = \Delta P_{pump} \dot{V}_{ref} \tag{4.18}$$

The motor heat loss is included in the total power consumption of the system because it is additionally consumed energy of the motor for driving. It allows consideration of the motor heat loss change through the flow boiling cooling.

The cooling capacity and the heating capacity are calculated as follows.

$$\dot{Q}_c = \dot{m}_{evap}\left(i_{evap,o} - i_{evap,i}\right) \tag{4.19}$$

$$\dot{Q}_h = \dot{m}_{cond}\left(i_{cond,i} - i_{cond,o}\right) \tag{4.20}$$

The system COP of cooling and heating is calculated as follows.

$$COP_c = \frac{\dot{Q}_c}{\dot{W}_{sys}} \tag{4.21}$$

$$COP_h = \frac{\dot{Q}_h}{\dot{W}_{sys}} \tag{4.22}$$

The detailed information and simulation conditions are presented in Table 4.1 and 4.2.

Table 4.1 Geometric parameters of target components

Component	Parameter	Value
Compressor	Volume displacement [mm^3]	33000
Outdoor unit	Type	Louvered fin type
	Width [mm]	345
	Height [mm]	572.6
	Depth [mm]	20
	Number of tube	81
Indoor evaporator	Type	Louvered fin type
	Width [mm]	215
	Height [mm]	256
	Depth [mm]	45
	Number of tube	29
Indoor condenser	Type	Louvered fin type
	Width [mm]	170
	Height [mm]	215
	Depth [mm]	20
	Number of tube	30

Table 4.1 Geometric parameters of target components (continued)

Component	Parameter	Value
Battery chiller	Type	Plate heat exchanger
	Width [mm]	60
	Height [mm]	31
	Length [mm]	63.6
	Number of path	26

Table 4.2 Simulation conditions

Season	Parameter	Value
Summer	Outdoor temperature [°C]	40
	Indoor temperature [°C]	25
	Compressor speed [Hz]	60
	Charge [kg]	0.2
	Battery heat loss [kW]	0.5
	Motor torque [N-m]	150
	Motor rotational speed [rpm]	4000
	Motor channel mass flow rate [g/s]	7 ~ 13
Winter	Outdoor temperature [°C]	-5
	Indoor temperature [°C]	18
	Compressor speed [Hz]	60
	Charge [kg]	0.03
	Battery heat loss [kW]	0
	Motor torque [N-m]	150
	Motor rotational speed [rpm]	4000
	Motor channel mass flow rate [g/s]	3 ~ 9

4.4 Results and discussion

4.4.1 Comparison of characteristics and performance in the summer season

The performance of the systems according to the mass flow rate of the motor cooling channel was calculated for comparison of the integrated systems. First, steady state calculation was carried out under the conditions that the ambient temperature in summer is 40°C, the temperature of cabin is 25°C, and the motor driving condition is the torque of 150 Nm and the rotational speed of 4000 rpm, respectively. The battery heat loss is 0.5 kW, and the battery chiller was used in consideration of the outside air temperature. The performance of the systems is compared for both the cooling performance of the motor and the system COP.

Fig. 4.5 shows the maximum and minimum temperatures of the motor winding according to the mass flow rate on the motor cooling channel. As shown in the figure, in the case of the PCVC system, as the motor-side mass flow rate increases, the temperature of the motor winding decreases significantly. Although the cooling performance is improved with increasing mass flow rate of motor cooling channel, the influence of the motor side inlet temperature is larger than the effect of the mass flow rate. Fig. 4.6 is a graph of

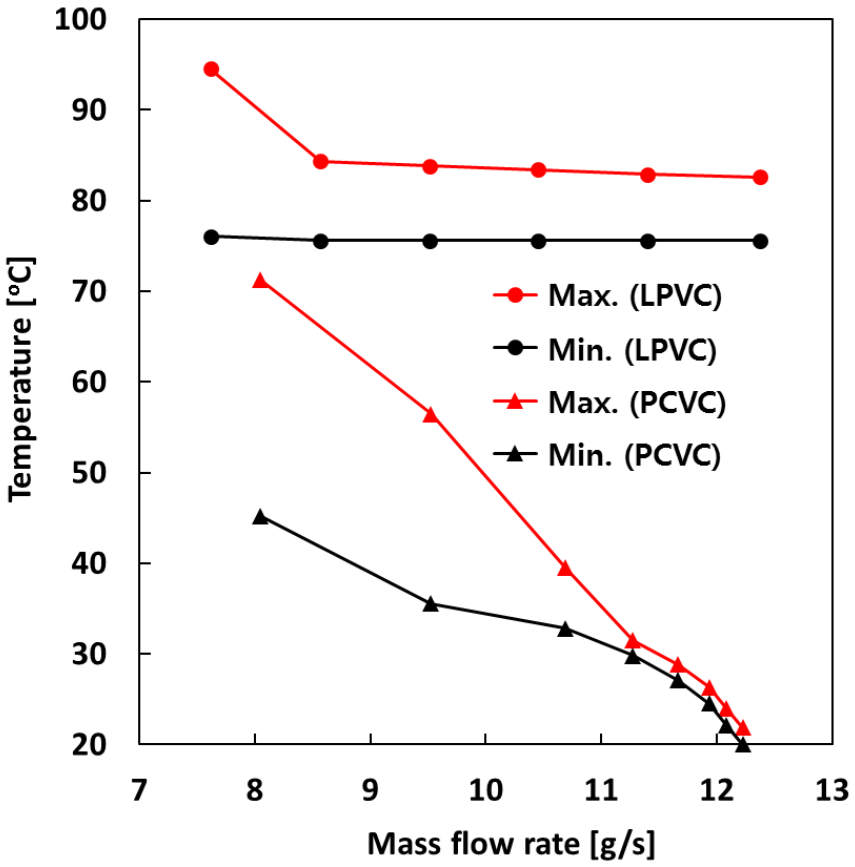

Fig. 4.5 Winding temperature with respect to mass flow rate into motor in summer

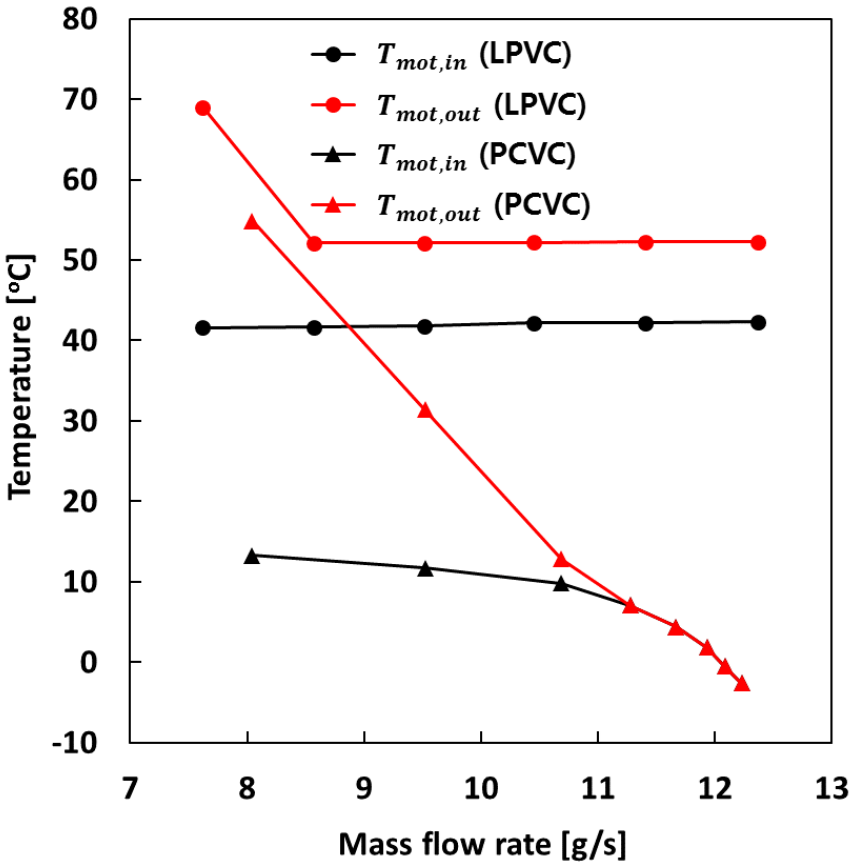

Fig. 4.6 Temperature of motor inlet and outlet with respect to mass flow rate into motor in summer

the motor cooling channel inlet and outlet temperature with respect to the mass flow rate of the motor cooling channel. As shown in the figure, as the mass flow rate increases, the motor channel inlet temperature for the parallel cooling system decreases. As the motor side mass flow rate increases, the mass flow rate of the refrigerant to the battery chiller and the indoor evaporator decreases. In particular, the decrease of the mass flow rate for the indoor evaporator increases DSH at the outlet of the indoor evaporator. Therefore, DSH of the refrigerant mixed from each evaporator is increased. The low pressure of the system has to go down in order to satisfy the given DSH, which reduces the evaporation temperature. Therefore, the temperature of the motor winding is decreased because the inlet temperature of the motor cooling channel is lowered.

On the other hand, in the case of the LPVC system, the motor winding temperature and the temperatures at the motor cooling channel inlet and outlet are hardly changed even if the mass flow rate of the motor cooling channel is increased. Because the change of the mass flow rate for motor cooling channel has little influence on the high pressure of the system. When the motor-side mass flow rate is small as 8 g/s or less, the refrigerant is completely vaporized at the outlet of the motor cooling channel. Therefore, the outlet temperature of the motor cooling channel and the maximum temperature of the motor winding are calculated higher than in the other cases. Since the motor temperature must

be under the limit temperature (180°C), the cooling performance of the motor of both systems is satisfied. However, as the winding temperature of the motor is lower, the heat loss of the motor is reduced. Thus, the motor cooling performance of the PCVC system is evaluated superior to that of the LPVC system.

In order to compare the system COP, the power consumption and cooling capacity of the system were calculated as shown in Fig. 4.7. As shown in the figure, the LPVC system maintains the power consumption of the system and cooling capacity independent to the mass flow rate of the motor cooling channel. As the motor-side mass flow rate increases, the power consumption of the pump increases. However, pump power consumption is very small compared to the power consumption of the compressor and the heat loss of the motor. Thus, the power consumption of the system is hardly affected by the mass flow rate. Whereas, in the case of the PCVC system, the power consumption and cooling capacity of the system decrease as the motor-side mass flow rate increases. Since the PCVC system uses three evaporators, when the motor-side mass flow rate increases, the mass flow rate of the indoor evaporator decreases and the indoor cooling capacity also decreases. Moreover, as described in Fig. 4.7, as the compressor inlet temperature decreases, the power consumption of the compressor decreases. The reduced winding temperature reduces the motor

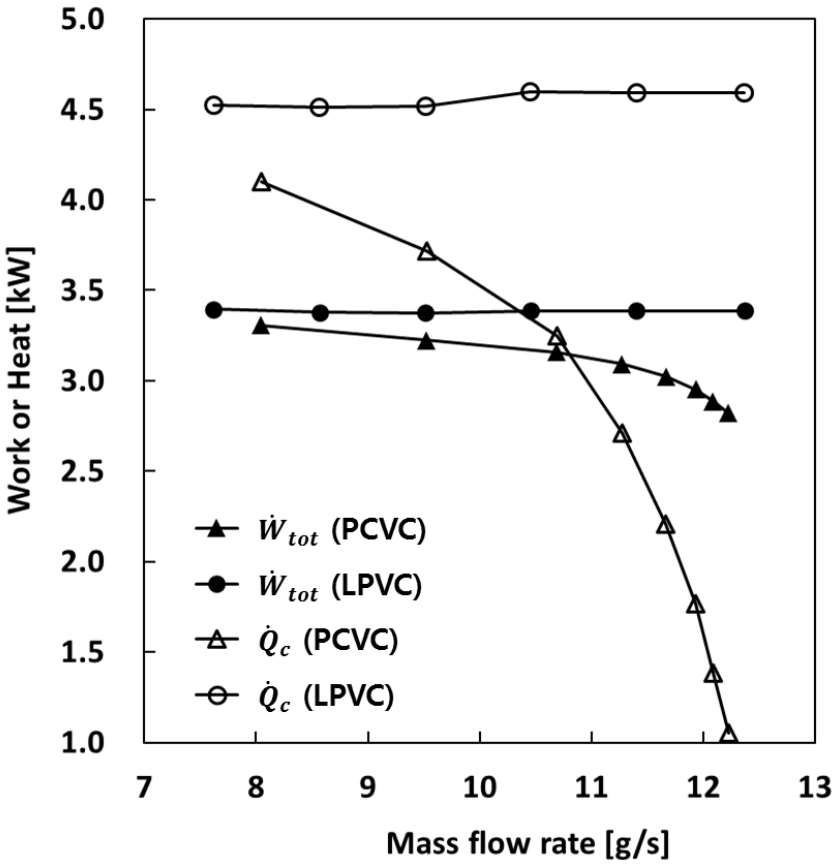

Fig. 4.7 Total system power and cooling capacity with respect to mass flow rate into motor in summer

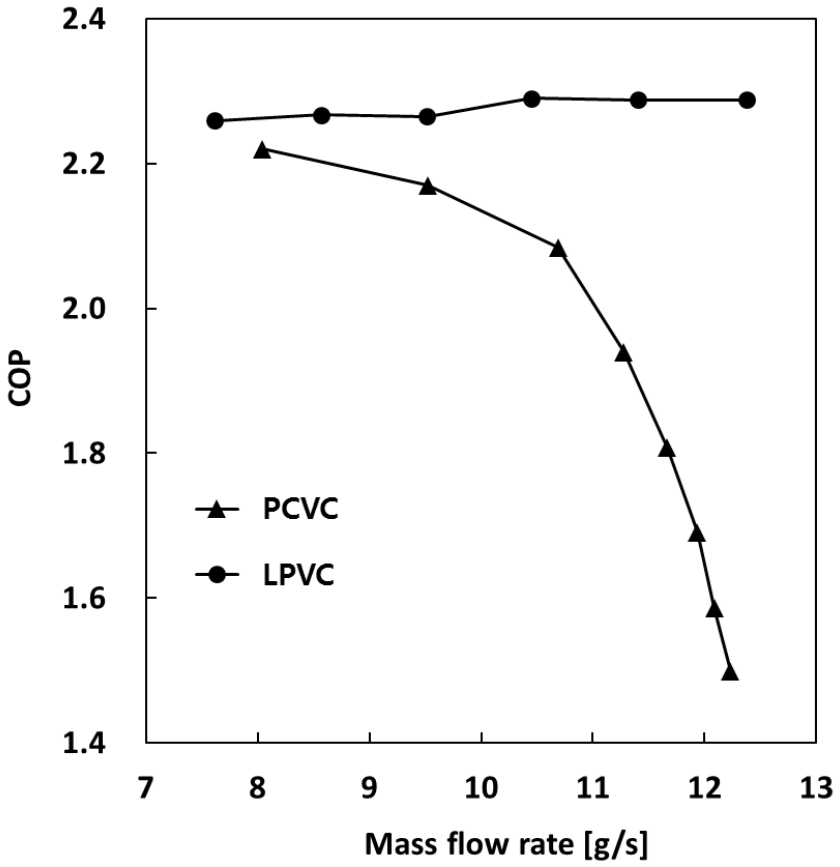

Fig. 4.8 System COP according to mass flow rate into motor in summer

heat loss. As a result, the system power consumption is reduced.

The system COP is calculated as shown in Fig. 4.8. The LPVC system has almost no change in COP, but the COP of the PCVC system decreases rapidly. The COP of the PCVC system is 2.17 when the motor-side mass flow rate is 9.52 g/s. However, since the motor outlet refrigerant is vaporized, it is not suitable for motor cooling. While, in the LPVC system, COP is 2.26 when the motor side mass flow rate is 9.51 g/s. Therefore, system COP of the LPVC system is better.

4.4.2 Comparison of characteristics and performance in the winter season

In winter, evaporation and condensation occur in reverse for heat pump. Winter operating conditions are: outdoor temperature -5ºC, cabin temperature 18ºC, compressor speed 60 Hz, motor torque 150 Nm, and motor rotational speed 4000 rpm. Based on the given conditions, the system performance was calculated according to the motor side mass flow rate.

Fig. 4.9 shows the result of the motor winding temperature, and Fig. 4.10 shows the result of the motor side refrigerant inlet and outlet temperature after 1 hour has passed.

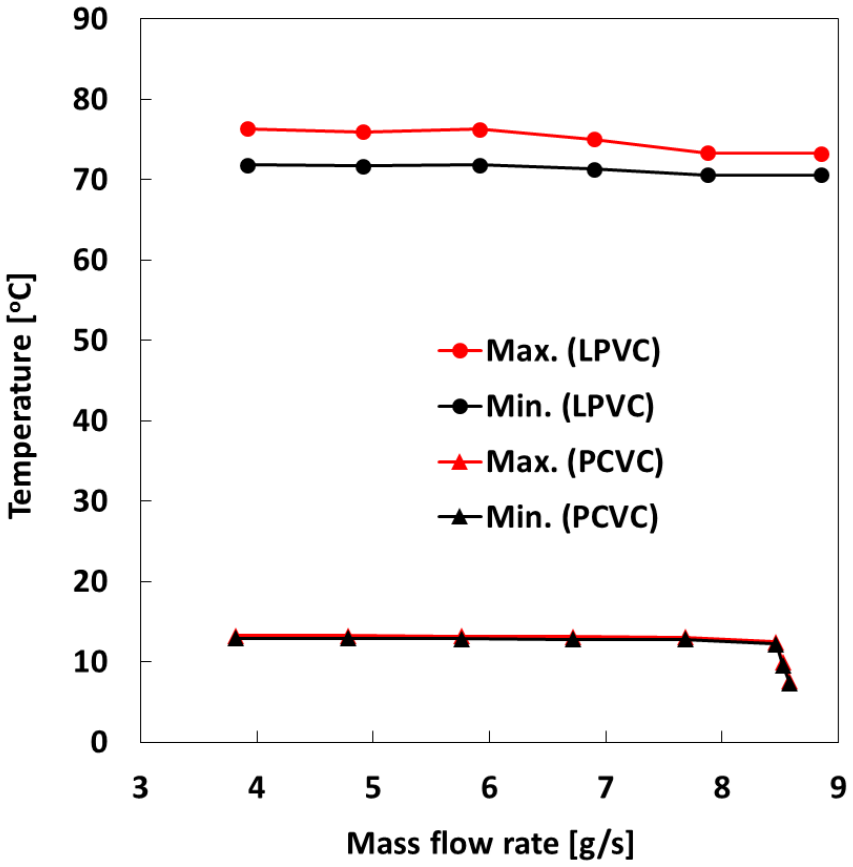

Fig. 4.9 Winding temperature with respect to mass flow rate into motor in winter after 1 hour has passed

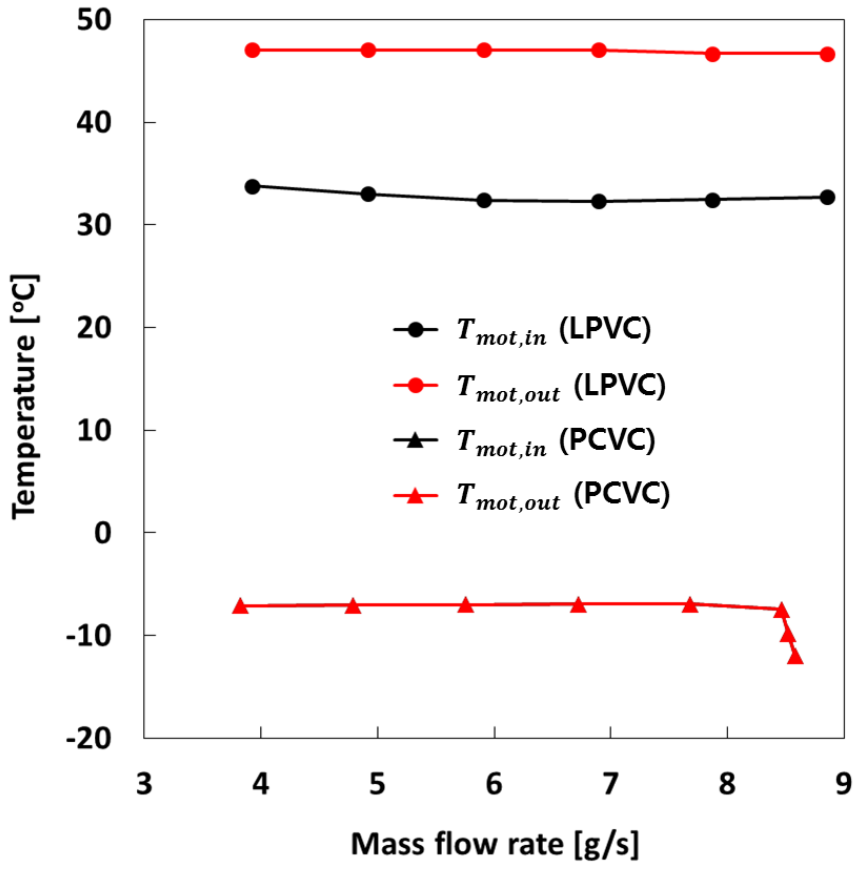

Fig. 4.10 Temperature of motor inlet and outlet with respect to mass flow rate into motor in winter after 1 hour has passed

Unlike in summer, the change in the inlet temperature of the motor channel according to the mass flow rate is not significant. Since the size of the outdoor unit is larger than that of the indoor unit, the change in capacity according to the variation of the mass flow rate is relatively small. While similar to summer, the PCVC system indicates the low motor channel inlet temperature because low pressure refrigerant is used to cool the motor. When the refrigerant is not completely vaporized, the motor winding temperature of the PCVC system is lower than that of the LPVC system. In order to ensure the cooling performance of the motor, the mass flow rate on the motor side should be properly selected.

In winter, motor cooling performance is not a critical issue. Because the outdoor temperature is very low, the motor can be cooled also by the water cooling. However, the advantage in performing motor cooling with the refrigerant system is waste heat recovery. The motor waste heat can be used to solve the problem of insufficient heating capacity of the electric vehicle in winter. The heat loss generated from the motor is transferred to the cabin by the refrigerant. As a result, the heating capacity of the cabin can be increased, and the system COP can also be improved.

Fig. 4.11 shows the power consumption and the heating capacity of the system, respectively. As shown in the figure, results of the LPVC system isn’t changed significantly as the motor-side mass flow rate increases. On the other

hand, the power consumption and the heating capacity of the PCVC system decrease sharply while the mass flow rate exceeds 8.46 g/s. Because the mass flow rate of the outdoor evaporator decreases, the capacity of the outdoor unit decreases as in the summer. The maximum heating capacity of the LPVC system is 0.58 kW higher than that of the PCVC system.

Fig. 4.12 shows the result of calculating the system COP. As shown in the figure, the COP of the PCVC system increases as the motor-side mass flow rate increases. However, when the mass flow rate exceeds 8.46 g/s, it shows a sharp decrease in COP. While, the LPVC system shows a gradual increasing trend as the motor side mass flow rate increases. The COP of the PCVC system is 1.44 when the mass flow rate for motor cooling channel is 8.46 g/s. The LPVC system exhibits COP of 1.51 when the mass flow rate is 8.85 g/s. Based on the calculated heating capacity and system COP, the LPVC system can further reduce the energy consumption of the electric vehicle.

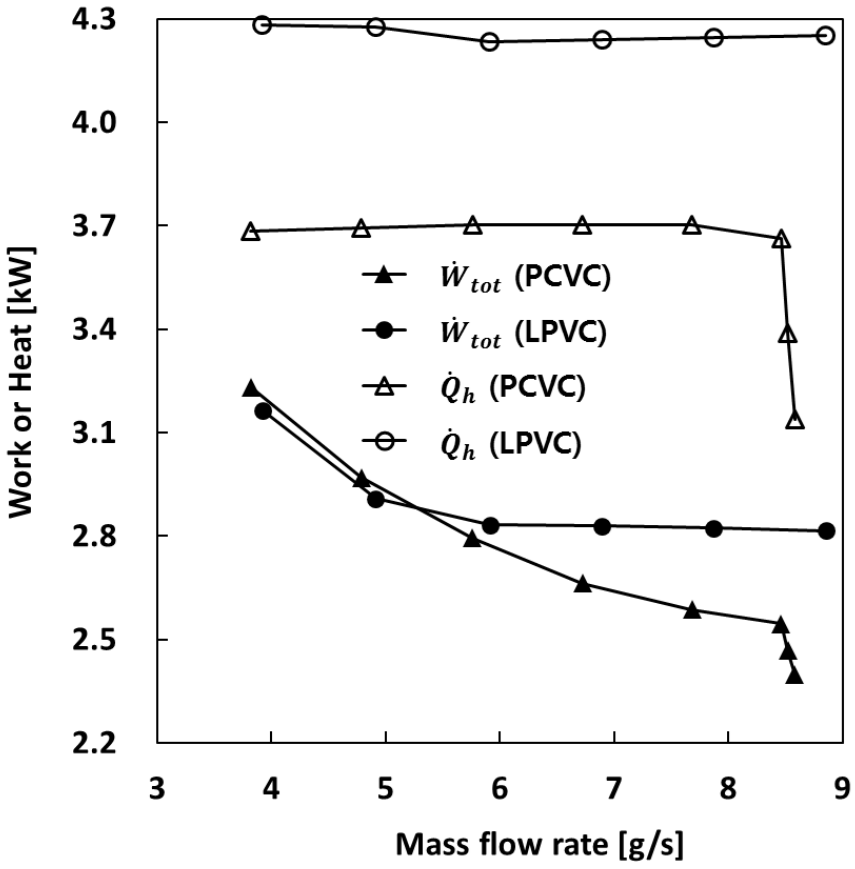

Fig. 4.11 Total system power and cooling capacity with respect to mass flow rate into motor in winter

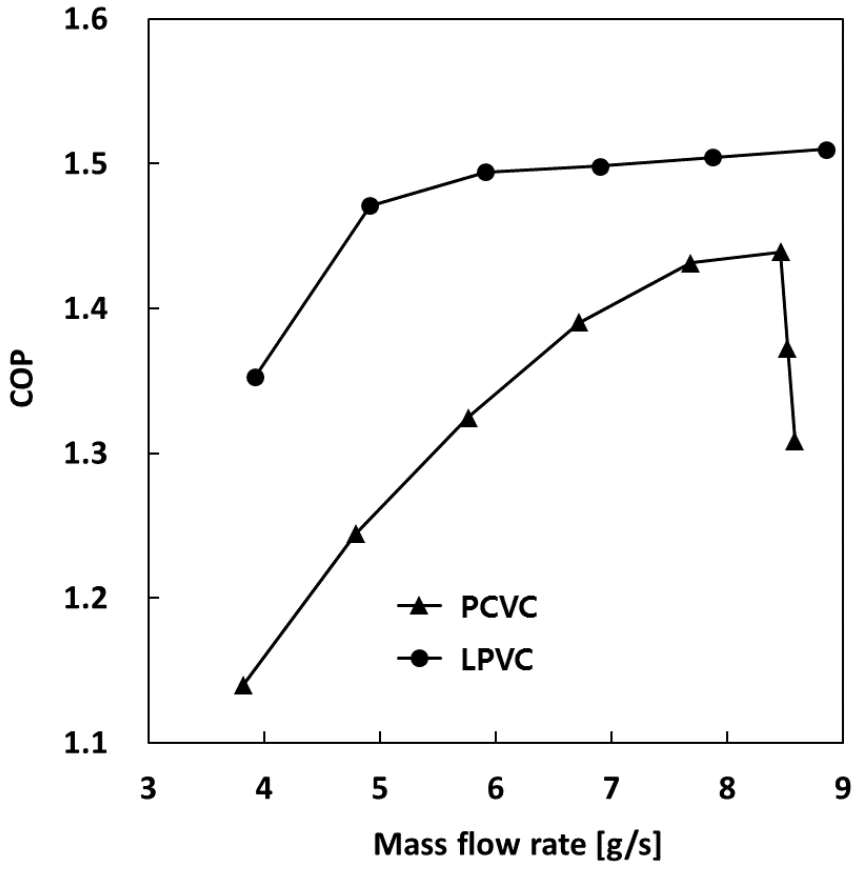

Fig. 4.12 System COP according to mass flow rate into motor in winter

4.5 Summary

In this chapter, two systems integrating heat pump system and motor cooling system with flow boiling are proposed for electric vehicle. The proposed systems were analyzed through steady state modeling and compared through both motor cooling performance and system COP.

Regardless of the season, the motor cooling performance of the PCVC system is superior to that of LPVC system. Because the low pressure refrigerant of the heat pump is used to cool the motor, the temperature of the refrigerant entering the motor cooling channel is low. While, since the LPVC system uses high pressure liquid refrigerant, the motor temperature is maintained higher than the PCVC system. However, with proper control for the motor side mass flow rate, the motor with both systems can be operated at a temperature lower than the limit temperature of the motor. Therefore, the motor cooling performance of both systems is satisfied.

The system COP of the LPVC system is always superior to that of the PCVC system. Because the LPVC system uses liquid pump for motor cooling, it consumes less power than PCVC system which uses part of the compressor mass flow rate to cool the motor. In the PCVC system, when the mass flow rate for the motor cooling increases, the mass flow rate of the indoor heat exchanger decreases, so the heating and cooling capacity decreases sharply. Therefore, the

system COP is decreased. Even though the heat loss of the motor with PCVC system is smaller than that of the LPVC system, the system COP of the LPVC system is higher than that of the PCVC system. The speed of the compressor can be increased to increase the heating or cooling capacity of the PCVC system, but it is difficult to improve the system COP due to the increasing power consumption.

Therefore, the energy efficiency of the electric vehicle can be improved by applying the LPVC system capable of cooling the motor using the liquid refrigerant at the outlet of the condenser regardless of the season.

Chapter 5. Concluding remarks

With the increasing demand for eco-friendly vehicles, as the thermal management performance for the motor becomes important, there has been a need for a method to replace the conventional water cooling system. Flow boiling is the method that can improve the motor cooling performance. In order to apply this method to an actual motor, in this study, firstly the heat transfer characteristics that occur in a curved rectangular channel is dealt with experiments. The numerical study for verifying motor cooling performance using lumped parameter thermal model is also conducted. Lastly, new systems integrating existing heat pump system and proposed flow boiling cooling system for motor are proposed and analyzed.

In the chapter 2, heat transfer characteristics in the curved rectangular channel were experimentally confirmed using R245fa and R134a. The heat transfer coefficient at the curved channel is varied depending on the location in the channel and the inlet mass flux, which also makes the channel temperature very different. The local heat transfer coefficient with location is largely reduced at location 3 and improved substantially around location 5. Because of this, the channel temperature is not uniform. Such a phenomenon is hardly affected by the heat flux and is greatly affected by the mass flux of the refrigerant. When the mass flux is low, a sudden drop of the heat transfer

coefficient appears. In order to explain the reason of that, high speed camera was used to investigate the boiling situation in the channel. As a result, it was confirmed that bubbles moved in the opposite direction to the main flow near the location 3 and moved on the heated surface. Therefore, there is a need for a suitable mass flux that can push the bubbles to apply boiling cooling efficiently on the curved channel.

In the chapter 3, fully lumped parameter thermal model for motor was developed to verify the performance of the proposed flow boiling cooling method. This model is a transient model in which all the thermal resistance in the cylindrical coordinate system, the heat loss of the motor and the heat transfer characteristics of the fluid are included. In this way, it is possible to calculate the internal temperature change and heat loss of the motor according to the cooling method and operating conditions. The cooling performance of the flow boiling cooling and water cooling was compared by the model. Flow boiling cooling can reduce the maximum winding temperature up to 4.6^{o}C compared to water cooling with the same pump power consumption. Due to the temperature reduction, motor power output can be increased as 6.0% using the same pump power.

In the last chapter, two new systems were proposed to apply the previously proposed flow boiling cooling to an actual vehicle, and the performance of each

system was analyzed by steady state analysis. The PCVC (Parallel Cooling Vapor Compression) system using a low pressure refrigerant by splitting a refrigerant from the outlet of an expansion valve of a vehicle heat pump system and the LPVC (Liquid Pump and Vapor Compressor) system using refrigerant from an outlet of a condenser by a liquid pump have been proposed. When each system is operated under the same operating conditions, the motor cooling performance of the PCVC system is better, but the LPVC system also showed excellent performance. When considering the system COP, the LPVC system showed higher COP than the PCVC system regardless of the season.

The flow boiling cooling proposed in this research could replace the existing water cooling method as it was confirmed in the chapter 3 and improve the motor cooling performance significantly. Also, it can be applied to the actual eco-friendly vehicle with the proposed LPVC system. Thus, the COP of the vehicle system can be improved over the existing vehicle thermal management system. Moreover, unlike the existing heat transfer studies, the heat transfer characteristics in the curved channel are studied experimentally, and it is thought that it can contribute to the heat transfer studies for similar shape in the future.

References

[1] International Council on Clean Transportation (ICCT) 2011b.

[2] Bloomberg new energy finance. Electric vehicle outlook 2017.

[3] Yano Research Institute. Traction motors for Xev in 2010. 2011.

[4] Venkataraman B., Godsey B., Shulman E., Thakur M., Midence R. Fundamentals of a motor thermal model and its applications in motor protection. IEEE 2005:127-144.

[5] Ruoho S., Kolehmainen J., Ikaheimo J., Arkkio A. Interdependence of demagnetization, loading, and temperature rise in a permanent-magnet synchronous motor. IEEE Transaction on magnetics 2010;46(3):949-953.

[6] Sato Y., Ishikawa S., Okubo T., Abe M., Tamai K. Development of high response motor and inverter system for the Nissan LEAF electric vehicle. SAE International 2011.

[7] Lajunen A. Thermal system simulations of an electric vehicle in different climate conditions. SAE Thermal Management System Symposium 2016. October 18-20.

[8] Dittus F.W., Boelter L.M.K. Heat transfer in automobile radiators of the tubular type. The University of California Publications on Engineering. 1930;2:443-461, Reprinted 1985. Int. Commun. Heat Mass. 12, 3-22.

[9] Shah M.M. Chart correlation for saturated boiling heat transfer: equations

and further study. ASHRAE Transaction 1982;88(1):185-196.

[10] Kandlikar S.G. A general correlation for saturated two-phase flow boiling heat transfer inside horizontal and vertical tubes. ASME Journal of Heat Transfer 1990;112:219-228.

[11] Wang C., Chen I.Y., Yang Y., Hu R. Influence of horizontal return bend on the two-phase flow pattern in small diameter tubes. Exp Therm Fluid Sci 2004;28:145-152.

[12] Chu J., Teng J., Greif R. Experimental and numerical study on the flow characteristics in curved rectangular microchannels. Appl Therm Eng 2010;30:1558-1566.

[13] Padilla M., Revellin R., Bonjour J. Two-phase flow visualization and pressure drop measurements of HFO-1234yf and R-134a refrigerants in horizontal return bends. Exp Therm Fluid Sci 2012;39:98-111.

[14] Owhadi A., Bell K.J., Crain B. Jr. Forced convection boiling inside helically-coiled tubes. Int. J. Heat Mass Transfer 1968;11:1779-1793.

[15] Nariai H., Kobayashi M., Matsuoka T. Friction pressure drop and heat transfer coefficient of two-phase flow in helically coiled tube once-through steam generator for integrated type marine water reactor. Journal of Nuclear Science and Technology 1982;19(11):936-947.

[16] Yi J., Liu Z., Wang J. Heat transfer characteristics of the evaporator section

using small helical coiled pipes in a looped heat pipe. Appl Therm Eng 2003;23:89-99.

[17] Zhao L., Guo L., Bai B., Hou Y., Zhang X. Convective boiling heat transfer and two-phase flow characteristics inside a small horizontal helically coiled tubing once-through steam generator. Int. J. Heat Mass Transfer 2003;46:4779-4788.

[18] Hwang K.W., Kim D.E., Yang K.H., Kim J.M., Kim M.H., Park. H.S. Experimental study of flow boiling heat transfer and dryout characteristics at low mass flux in helically-coiled tubes. Nucl Eng Des 2014;273:529-541.

[19] Chung Y., Bae K., Kim K.K., Lee W. Boiling heat transfer and dryout in helically coiled tubes under different pressure conditions. Ann. Nucl. Energy 2014;71:298-303.

[20] Chen C., Han J., Jen T., Shao L. Thermo-chemical characteristics of R134a flow boiling in helically coiled tubes at low mass flux and low pressure. Thermochim Acta 2011;512:163-169.

[21] Elsayed A.M., AL-Dadah R.K., Mahmoud S., Rezk A. Investigation of flow boiling heat transfer inside small diameter helically coiled tubes. Int. J. Refrig 2012;35:2179-2187.

[22] Cui W., Li L., Xin M., Jen T., Chen Q., Liao Q. A heat transfer correlation

of flow boiling in micro-finned helically coiled tube. Int. J. Heat Mass Transfer 2006;49:2851-2858.

[23] Aria H., Akhavan-Behabadi M.A., Shemirani F.M. Experimental Investigation on Flow Boiling Heat Transfer and Pressure Drop of HFC-134a inside a Vertical Helically Coiled Tube. Heat Transfer Eng 2012;33(2):79-87.

[24] Wongwises S., Polsongkram M. Evaporation heat transfer and pressure drop of HFC-134a in a helically coiled concentric tube-in-tube heat exchanger. Int. J. Heat Mass Transfer 2006;49:658-670.

[25] Kang H.J., Lin C.X., Ebadian M.A. Condensation of R134a flowing inside helicoidal pipe. Int. J. Heat Mass Transfer 2000;43:2553-2564.

[26] Han J.T., Lin C.X., Ebadian M.A. Condensation heat transfer and pressure drop characteristics of R-134a in an annular helical pipe. Int. J. Heat Mass Transfer 2005;32:1307-1316.

[27] Shao L., Han J. Condensation heat transfer of R-134a in horizontal straight and helically coiled tube-in-tube heat exchangers. J Hydrodyn 2007;19(6):677-682.

[28] Li H. Cooling of a permanent magnet electric motor with a centrifugal impeller. Int. J. Heat Mass Transfer 2010;53:797-810.

[29] Jang J., Chiu H., Yan W., Tsai M.C., Wang P. Numerical study on

electromagnetics and thermal cooling of a switched reluctance motor. Case studies in thermal engineering 2015;6:16-27.

[30] Grabowski M., Urbaniec K., Wernik J., Wołosz K.J. Numerical simulation and experimental verification of heat transfer from a finned housing of an electric motor. Energy Convers. Manag. 2016;125:91-96.

[31] Rhebergen C., Bilgin B., Emadi A., Rowan E., Lo J. Enhancement of electric motor thermal management through axial cooling methods: a materials approach. IEEE 2015:5682-5688.

[32] Xu Y., Jia Y., Ai M., Wang Y. Heat transfer characteristics of external ventilated path in compact high-voltage motor. Int. J. Heat Mass Transfer 2018;124:1136-1146.

[33] Chiu H., Jang J., Yan W., Shiao R. Thermal performance analysis of a 30 kW switched reluctance motor. Int. J. Heat Mass Transfer 2017;114:145-154.

[34] Pechánek R., Bouzek L. Analyzing of two types water cooling electric motors using computational fluid dynamics. 15th International Power Electronics and Motion Control Conference. 2012.

[35] Tuysuz A., Meyer F., Steichen M., Zwyssig C., Kolar J.W. Advanced cooling methods for high-speed electrical machines. IEEE Transactions on industry applications 2017;53.

[36] Chen W., Ju Y., Yan D., Guo L., Geng Q., Shi T. Design and optimization of dual-cycled cooling structure for fully-enclosed permanent magnet motor. Appl Therm Eng 2019;153:338-349.

[37] Putra N., Ariantara B. Electric motor thermal management system using L-shaped flat heat pipes. Appl Therm Eng 2017;126:1156-1163.

[38] Sun Y., Zhang S., Yuan W., Tang Y., Li J., Tang K. Applicability study of the potting material based thermal management strategy for permanent magnet synchronous motors. Appl Therm Eng 2019;149:1370-1378.

[39] Wang J., Li Y., Wang S., Zhang H., Ning X., Guo W. Experimental investigation of the thermal control effects of phase change material based packaging strategy for on-board permanent magnet synchronous motors. Energy Convers. Manag. 2016;123:232-242.

[40] Wang S., Li Y., Li Y., Wang J., Xiao X., Guo W. Conception and experimental investigation of a hybrid temperature control method using phase change material for permanent magnet synchronous motors. Exp Therm Fluid Sci 2017;81:9-20.

[41] Wang S., Li Y., Li Y., Wang J., Xiao X., Guo W. Transient cooling effect analyses for a permanent-magnet synchronous motor with phase-change-material packaging. Appl Therm Eng 2016;109:251-260.

[42] Lim D.H., Kim S.C. Thermal performance of oil spray cooling system for

in-wheel motor in electric vehicles. Appl Therm Eng 2014;63:577-587.

[43] Davin T., Pellé J., Harmand S., Yu R. Experimental study of oil cooling systems for electric motors. Appl Therm Eng 2015;75:1-13.

[44] Lee K., Cha H., Kim Y. Development of an interior permanent magnet motor through rotor cooling for electric vehicles. Appl Therm Eng 2016;95:348-356.

[45] Alexandrova Y., Semken R.S., Pyrh ö nen J. Permanent magnet synchronous generator design solution for large direct-drive wind turbines: Thermal behavior of the LC DD-PMSG. Appl Therm Eng 2014;65:554-563.

[46] Lim D.H., Lee M., Lee H., Kim S.C. Performance evaluation of an in-wheel motor cooling system in an electric vehicle/hybrid electric vehicle. Energies 2014;7:961-971.

[47] Campbell J.B., Tolbert L.M., Ayers C.W., Ozpineci B., Lowe K.T. Two-phase cooling method using the R134a refrigerant to cool power electronic devices. IEEE Transactions on industry applications 2007;43.

[48] Wang P., McCluskey P., Bar-Cohen A. Two-phase liquid cooling for thermal management of IGBT power electronic module. J ELECTRON PACKAGING 2013;135.

[49] Choi E.J., Park J.Y., Kim M.S. A comparison of temperature distribution

in PEMFC with single-phase water cooling and two-phase HFE-7100 cooling methods by numerical study. Int. J. Hydrog. Energy 2018;43:13406-13419.

[50] Choi E.J., Park J.Y., Kim M.S. Two-phase cooling using HFE-7100 for polymer electrolyte membrane fuel cell application. Appl Therm Eng 2019;148:868-877.

[51] Leighton D. Combined fluid loop thermal management for electic drive vehicle range improvement. SAE Int. J. Passeng. Cars - Mech. Syst. 2015;8(2),doi:10.4271/2015-01-1709.

[52] Kwon C., Kim M.S., Choi Y., Kim M.S. Performance evaluation of a vapor injection heat pump system for electric vehicles. Int J Refrig 2017;74:138-150.

[53] Choi Y.U., Kim M.S., Kim G.T., Kim M., Kim M.S. Performance analysis of vapor injection heat pump system for electric vehicle in cold startup condition. Int J Refrig 2017;80:24-36.

[54] Ahn J.H., Kang H., Lee H.S., Jung H.W., Baek C., Kim Y. Heating performance characteristics of a dual source heat pump using air and waste heat in electric vehicles. Appl Energ 2014;119:1-9.

[55] Ahn J.H., Lee J.S., Baek C., Kim Y. Performance improvement of a dehumidifying heat pump using an additional waste heat source in electric

vehicles with low occupancy. Energy 2016;115:67-75.

[56] Park S., Jung D. Design of vehicle cooling system architecture for a heavy duty series-hybrid electric vehicle using numerical system simulations. J ENG GAS TURB POWER 2010;132.

[57] Hosoz M., Direk M. Performance evaluation of an integrated automotive air conditioning and heat pump system. Energy Convers. Manag. 2006;47:545-559.

[58] Qin F., Xue Q., Velez G.M.A., Zhang G., Zou H., Tian C. Experimental investigation on heating performance of heat pump for electric vehicles at -20^{o}C ambient temperature. Energy Convers. Manag. 2015;102:39-49.

[59] Rugh J.P. Integrated vehicle thermal management – combining fluid loops in electric drive vehicles. Vehicle Technologies Program Annual Merit Review, 2013.

[60] Lee S., Kang H., Kim Y. Performance optimization of a hybrid cooler combining vapor compression and natural circulation cycles. Int. J. Refrig 2009;32:800-808.

[61] Zhang P., Wang B., Wu W., Shi W., Li X. Heat recovery from Internet data centers for space heating based on an integrated air conditioner with thermosyphon. Renew Energ 2015;80:396-406.

[62] Dong J., Lin Y., Deng S., Shen C., Zhang Z. Experimental investigation of

an integrated cooling system driven byboth liquid refrigerant pump and vapor compressor. Energ Buildings 2017;154:560-568.

[63] Zhang H., Shao S., Jin T., Tian C. Numerical investigation of a CO2 loop thermosyphon in an integrated air conditioning system for free cooling of data centers. Appl Therm Eng 2017;126:1134-1140.

[64] Rouhani S.Z., Axelsson E. Calculation of void volume fraction in the subcooled and quality boiling regions. Int. J. Heat Mass Transfer 1970;13:383-393.

[65] Padilla M., Revellin R., Wallet J., Bonjour J. Flow regime visualization and pressure drops of HFO-1234yf, R-134a and R-410A during downward two-phase flow in vertical return bends. Int J Heat Fluid Fl 2013;40:116-134.

[66] Lemmon, E.W., Bell, I.H., Huber, M.L., McLinden, M.O. NIST Standard Reference Database 23: Reference Fluid Thermodynamic and Transport Properties-REFPROP, Version 10.0, National Institute of Standards and Technology, Standard Reference Data Program, Gaithersburg, 2018.

[67] Lee J., Mudawar I. Critical heat flux for subcooled flow boiling in micro-channel heat sinks. Int. J. Heat Mass Transfer 2009;52:3341-3352.

[68] Agostini B., Bontemps A. Vertical flow boiling of refrigerant R134a in small channels. Int J Heat Fluid Fl 2005;26:296-306.

[69] Delnoij E., Kuipers J.A.M., van Swaaij W.P.M. Dynamic simulation of gas-liquid twophase flow: effect of column aspect ratio on the flow structure. Chem. Eng. Sci. 1997;52:3759-3772.

[70] Saffman P.G. The lift on a small sphere in a slow shear flow. J. Fluid Mech. 1965;22(2):385-400.

[71] Mei R., Klausner J.F. Shear lift force on spherical bubbles. Int J Heat Fluid Fl 1994;15:62-65.

[72] Klausner J.F., Mei R., Bernhard D.M., Zeng L.Z. Vapor bubble departure in forced convection boiling. Int. J. Heat Mass Transfer 1993;36(3):651-662.

[73] Roberts D. The application of an induction motor thermal model to motor protection and other functions. University of Liverpool, 1986.

[74] Perez I.J., Kassakian J.G. A stationary thermal model for smooth air-gap rotating electric machines. Elec Mach Power Syst 2007;3:285-303.

[75] Fan J., Zhang C., Wang Z., Dong Y., Nino C.E., Tariq A.R., Strangas E.G. Thermal analysis of permanent magnet motor for the electric vehicle application considering driving duty cycle. IEEE Transactions on magnetics 2010;46(6):2493-2496.

[76] Kim D., Choi J., Chun Y., Koo D., Han P. The study of the stray load loss and mechanical loss of three phase induction motor considering

experimental results. J Electr Eng Technol 2013;8:742-747.

[77] Fluxmotor 2018. Altair.

[78] Rogers G.F.C., Mayhew Y.R. Heat transfer and pressure loss in helically coiled tubes with turbulent flow. Int. J. Heat Mass Transfer 1964;7:1207-1216.

[79] Taylor G.I. Stability of a viscous liquid contained between two rotating cylinders. Philos. Trans. Roy. Soc. London A, Math. Phys. Sci. 1923;223:289-343.

[80] Howey D.A., Childs P.R.N., Holmes A.S. Air-gap convection in rotating electrical machines. IEEE Transactions on industrial electronics 2012;59(3):1367-1375.

[81] Bjorklund I., Kays W. Heat transfer between concentric rotating cylinders. Trans. ASME, J. Heat Transf. 1959;81:175-186.

[82] Becker K., Kaye J. Measurements of diabatic flow in an annulus with an inner rotating cylinder. Trans. ASME, J. Heat Transf. 1962;84:97-105.

[83] Becker K., Kaye J. The influence of a radial temperature gradient on the instability of fluid flow in an annulus with an inner cylinder rotating. Trans. ASME, J. Heat Transf. 1962;84:106-110.

[84] Kim J.S., Moon J.W., Kwak T.H., Kang T.G. Numerical investigation on an oil cooling system in the motor for a hybrid vehicle. J. Comput. Fluids

Eng. 2017;22(3):86-94.

[85] Deeb R. Thermal calculations of permanent magnet motors in high current technology. BRNO UNIVERSITY OF TECHNOLOGY. Doctoral thesis. 2013.

[86] Lee Y., Kim K., Hur J. Dynamic analysis algorithm of irreversible demagnetization of IPM-type brushless DC motor by stator turn fault. The Transactions of the Korean Institute of Electrical Engineers 2013;62(12):1661-1667.

[87] Chen S.L., Gerner F.M., Tien C.L. General film condensation correlations. Exp Heat Transfer 1987;1:93-107.

[88] Gungor K., Winterton R., Simplified gernaral correlation for saturated flow boiling and comparisons with data. Chemical Engineering Research and Design. Chem Eng Res Des. 1987;65:148-156.

[89] Chang Y., Wang C. A generalized heat transfer correlation for louver fin geometry. Int. J. Heat Mass Transfer 1997;40(3):533-544.

[90] Dong J., Chen J., Chen Z., Zhang W., Zhou Y. Heat transfer and pressure drop correlations for the multi-louvered fin compact heat exchangers. Energy Convers. Manag. 2007;48:1506-1515.

[91] Yan Y.-Y., Lin T.-F. Evaporation heat transfer and pressure drop of refrigerant R134a in a plate heat exchanger. Transactions of the ASME

1999;121:118-127.

[92] Longo G.A., Gasparella A., Sartori R. Experimental heat transfer coefficients during refrigerant vaporisation and condensation inside herringbone-type plate heat exchangers with enhanced surfaces. Int. J. Heat Mass Transfer 2004;47:4125-4136.

국 문 초 록

본 연구에서는 모터의 냉각 성능을 향상시키기 위해 유동 비등 냉각 방법을 제안하고 이에 대한 실험과 시뮬레이션을 실시했다. 모터 열관리는 성능 향상과 고장 방지를 위해 매우 중요하다. 영구자석형 모터의 수요와 출력이 증가함에 따라 모터 열관리는 점점 더 중요해지고 있다. 출력이 향상되고 크기가 작아지기 때문에 모터의 열 손실이 증가하여 기존의 수냉 방식을 대체하는 새로운 냉각 방식이 필요하다. 따라서 본 연구에서는 기존의 냉각 유로에 냉매를 이용하는 유동 비등 냉각 방법을 제안한다.

유동 비등 냉각을 모터 냉각에 적용하기 위해서는 곡선 유로에서의 유동 비등 특성에 관한 연구가 필요하다. 따라서 R245fa와 R134a를 이용한 열전달 실험을 모터 냉각 채널과 모터 열손실을 모사함으로써 수행하였다. 이를 통해 유로 내의 위치에 따른 국소 열전달 계수를 도출하였다. 열전달 계수의 변화가 채널 내 위치에 따라 관찰되는데, 이를 설명하기 위해 기포의 동적 거동을 예측하였다. 또한 실제 기포의 움직임을 초고속 카메라로 촬영하였다. 그 결과, 기포가 가열면에 붙은 채로 주 유동과 반대 방향으로 이동하면 열전달 계수가 감소하는 것이 확인되었다. 따라서 열전달 계수의 감소를 방지하기 위해 질량 유량을 적절하게 제어하여 기포를 밀어낼 수 있도록 운전할 필요가 있다.

유동 비등 냉각 성능을 검증하기 위해 모터의 집중형 열모델을 개발하였다. 이 모델을 이용하여 모터의 위치에 따라 온도와 열손실

을 계산하여 과도 열해석을 수행하였다. 모터의 권선 온도와 열손실을 기존의 수냉 방식과 비교해 유동 비등 냉각 성능을 확인했다. 동일한 펌프 소모 동력을 필요로 할 때, 유동 비등 냉각 모터의 권선 온도는 수냉 방식보다 최대 4.6℃ 낮게 유지될 수 있다. 동일한 냉각 성능을 유지할 경우, 펌프 소모 동력을 92.0% 저감할 수 있다. 또한 동일한 펌프 소모 동력으로 기존보다 출력이 6.0% 향상된 모터를 안정적으로 냉각할 수 있다.

제안된 방법을 실제 차량에 적용하기 위해 기존의 히트 펌프 시스템의 냉매를 이용한 통합 시스템이 제안되었다. 차량 실내의 열관리 및 모터 냉각 성능을 PCVC (Parallel Cooling Vapor Compression) 시스템과 LPVC (Liquid Pump and Vapor Compressor) 시스템 각각에 대해 계산하였다. 그 결과, 응축기 출구에서 냉매를 끌어와 모터 냉각에 사용하는 LPVC 시스템이 계절에 관계없이 높은 성능을 나타내었다.

본 연구에서 제안된 유동 비등 냉각 방법은 기존의 차량 시스템에 쉽게 통합될 수 있다. 또한 기존 수냉 방식에 비해 모터의 냉각 성능이 크게 향상된다. 따라서 유동 비등을 이용한 모터 냉각 방법은 친환경 자동차의 성능과 안전성을 향상시킬 수 있다.

주요어: 모터 냉각, 유동 비등, 곡선 유로, 집중형 열모델, 통합 히트 펌프 시스템

학 번: 2014-21567